

University of Alberta Library




0 1620 2667199 8

88F-176

Ex libris
UNIVERSITATIS
ALBERTAENSIS





Digitized by the Internet Archive
in 2025 with funding from
University of Alberta Library

<https://archive.org/details/0162026671998>

UNIVERSITY OF ALBERTA

RELEASE FORM

AUTHOR: Brent J. McDonell

TITLE: Burning Rates of Propane-Air Mixtures in
Homogeneous Decaying Turbulence

DEGREE: Masters of Science

GRANTED: Fall, 1988

Permission is hereby granted to THE UNIVERSITY OF ALBERTA LIBRARY to reproduce single copies of this thesis and to lend or sell such copies for private, scholarly or scientific research purposes only.

The author reserves other publication rights, and neither the thesis nor extensive extracts from it may be printed or otherwise reproduced without the author's written permission.

THE UNIVERSITY OF ALBERTA

BURNING RATES OF PROPANE-AIR
MIXTURES IN HOMOGENEOUS
DECAYING TURBULENCE



BY

BRENT J. McDONELL

A THESIS

SUBMITTED TO THE FACULTY OF GRADUATE STUDIES AND RE-
SEARCH IN PARTIAL FULFILMENT OF THE REQUIREMENTS FOR THE
DEGREE OF MASTERS OF SCIENCE IN MECHANICAL ENGINEERING

EDMONTON, ALBERTA
(FALL, 1988)

THE UNIVERSITY OF ALBERTA
FACULTY OF GRADUATE STUDIES AND RESEARCH

The undersigned certify that they have read, and recommend to the Faculty of Graduate Studies and Research for acceptance, a thesis entitled BURNING RATES OF PROPANE-AIR MIXTURES IN HOMOGENEOUS DECAYING TURBULENCE submitted by Brent J. McDonell in partial fulfilment of the degree of Masters of Science.

ABSTRACT

This thesis presents an experimental study of the effects of turbulence on constant volume combustion of propane-air mixtures. The apparatus consisted of a centrally ignited cubical combustion chamber across which was drawn a perforated plate at controlled speeds to generate known levels of turbulence prior to ignition. The turbulence was characterized in terms of root-mean-square intensity and integral length scale based on hot wire anemometry. Hot wire measurements were performed both in the combustion cell and behind perforated plates in a wind tunnel. Based on measured turbulence decay rates, the turbulence intensity and scale at ignition were independently varied by controlling the plate speed, plate perforation size, and the delay after plate movement to ignition.

Combustion diagnostics based on direct high speed photography, measured pressure rise, and flame arrival detection were compared. It was shown that burning speed could be reasonably deduced from the pressure signal for both laminar and turbulent explosions. A photomultiplier based technique for monitoring burning rate as a function of light emitted from the flame was also demonstrated, but slight mixture variability led to high repeatability uncertainty in this measurement.

Combustion duration was reduced with increasing turbulence intensity at ignition through increased burning

speeds. The effect of integral scale on combustion duration showed an apparent trade-off between the benefit of large scale turbulence (which is longer lived in the combustion process), and small scale turbulence which was observed to better enhance instantaneous burning velocity. Burning velocity was measured at a fixed flame size and the turbulence at that point was estimated based on the known turbulence decay functions. A correlation of turbulent to laminar burning speed ratio against intensity and integral scale showed that turbulent burning speed was linearly proportional to intensity, and inversely proportional to the square root of integral scale. This correlation appeared approximately independent of mixture strength.

TABLE OF CONTENTS

CHAPTER	PAGE
1. INTRODUCTION	1
2. BACKGROUND FOR THIS STUDY	4
2.1 Laminar Burning Speed	4
2.2 Turbulent Flame Growth	5
2.3 Turbulence Generation	6
2.4 Objectives of This Study	10
3. TURBULENT COMBUSTION APPARATUS AND INSTRUMENTATION	12
3.1 Construction of the Combustion Cell	12
3.1.1 Turbulence Generation Plates	15
3.1.2 Plate Movement Mechanism	15
3.1.3 Triggering Plate Motion	19
3.1.4 Ignition System	22
3.1.5 Ignition Triggering System	24
3.2 Sensors for the Turbulent Combustion Cell . .	28
3.2.1 Plate Speed Sensor	28
3.2.2 Timing Pulse Signal	30
3.2.3 Pressure Measurement	32
3.2.4 Temperature Probe	32
3.2.5 Flame Arrival Detector	33
3.2.6 Flame Photography	35
3.2.7 Photomultiplier Based Measurements .	36
3.2.8 Recording and Storage of Data	38
3.3 Turbulence Measurements	42
3.3.1 Anemometry in the Combustion Cell . .	44

CHAPTER	CONTENTS (continued)	PAGE
	3.3.2 Anemometry in the Wind Tunnel	47
4.	RESULTS OF TURBULENCE MEASUREMENTS	50
4.1	General Discussion	50
4.2	Turbulence Behind Perforated Plates in the Wind Tunnel	53
4.2.1	Decay of Mean Velocity	55
4.2.2	Decay of RMS Fluctuation Velocity	58
4.2.3	Power Spectra, Correlation, and Scales	63
4.3	Turbulence in the Combustion Cell	72
4.4	Conclusions of Chapter 4	78
5.	MEASUREMENTS OF FLAME GROWTH	80
5.1	Repeatability in the Combustion Cell	80
5.2	Measuring Laminar Flame Growth	83
5.2.1	Laminar Flame Speed	89
5.3	Turbulent Flame Speed	94
5.4	Photomultiplier Based Diagnostics	96
6.	RESULTS OF TURBULENT COMBUSTION EXPERIMENTS	104
6.1	Effects of Turbulents on Overall Combustion	105
6.2	Burning Speeds and Turbulence	110
6.2.1	Burning Speed Results	113
6.2.2	Comparison To Previous Work	116
7.	CONCLUSIONS	125
7.1	Turbulence	126
7.2	Flame Measurements	126

CONTENTS (continued)		PAGE
CHAPTER		
7.3	Turbulence and Flame Growth	127
7.4	Recommendations for Future Research	128
REFERENCES	131

LIST OF FIGURES

FIGURE		PAGE
3.1	Layout of the Turbulent Combustion Cell	13
3.2	Perforated Plates Used in the Turbulent Combustion Cell	16
3.3	Mechanism for Perforated Plate Movement	17
3.4	Speed of the Perforated Plate Across the Combustion Chamber	20
3.5	Electronics for Controlling Perforated Plate Motion	21
3.6	Ignition Circuit and Electrode Detail	23
3.7	Ignition Triggering Electronics	25
3.8	Apparatus for Air-Fuel Mixture Preparation	27
3.9	Perforated Plate Speed Sensor with Sample Output Signal	29
3.10	Timing Pulse Circuit with Sample Output Signal	31
3.11	Flame Ionization Detection Circuit and Sensor Detail	34
3.12	Photomultiplier Optical System Layout	37
3.13	Signal Recording and Digitization Summary	39
3.14	Typical Explosion Record of Stoichiometric Propane-Air (Non-Turbulent)	43
3.15	Sample Calibration Curve for Hot Wire Anemometer Signal	45
3.16	Apparatus and Signal Recording Summary for Turbulence Measurement in the Combustion Cell	46
3.17	Apparatus and Signal Recording Summary for Turbulence Measurement in the Wind Tunnel	48
4.1	Horizontal Velocity Profiles Downstream of 20 mm D. Perforated Plate	54

FIGURES (continued)

FIGURE		PAGE
4.2	Decay of Mean Velocity on the Centreline Downstream of the Perforated Plates	56
4.3	Decay of RMS Fluctuation Velocity on the Centreline Downstream of the Perforated Plates	56
4.4	Power Law Fits to the Decay of RMS Fluctuation Velocity Downstream of the Perforated Plates	59
4.5	Comparison Between RMS Decay Behind a Perforated Plate and That Behind Lattice Type Screens	61
4.6	The Normalized Power Spectrum at 10 D. Downstream of the 10 mm D. Perforated Plate	64
4.7	Power Spectra at Various Positions Down- Stream of the 10 mm D. Perforated Plate	64
4.8	The Autocorrelation Function at 10 D. Downstream of the 10 mm D. Perforated Plate	66
4.9	The Growth of Turbulence Scales Downstream of the 10 mm D. Perforated Plate	66
4.10	Power Law Fits to the Growth of Integral Scales Downstream of the Perforated Plates	70
4.11	Anemometer Signal in the Combustion Cell Following the Passage of the 20 mm D. Perforated Plate	73
4.12	The Ensemble Mean Velocity at the Centre of the Combustion Cell for 12 Identical Passes of the 20 mm D. Perforated Plate	73
4.13	Comparing the Spatial Decay of Wind Tunnel Turbulence and the Temporal Decay of the Ensemble Mean Velocity in the Combustion Cell for the 20 mm D. Perforated Plate	76
5.1	Variability of Observed Peak Pressure at Different Mixture Settings	82
5.2	Pressure Record for Stoichiometric Quiescent Explosion Showing the Flame Size Datum From the Ionization Sensor	82

FIGURES (continued)

FIGURE		PAGE
5.3	Comparing the Available Flame Size Measures	87
5.4	Microdensitometer Trace of a Photographed Laminar Flame Sphere (15 ms After Ignition)	87
5.5	Smoothing the Early Pressure Signal	92
5.6	Comparing the Derivative of the Raw Pressure Signal With That of the Smoothing Function	92
5.7	Comparing Flame Speed Derived From Smoothed Pressure Record With That Predicted With the Correlation of Reference [9]	93
5.8	Comparing Photographed Flame Size With Pressure Prediction for a Moderately Turbulent Flame	97
5.9	Microdensitometer Trace of a Photographed Turbulent Flame (11.6 ms After Ignition)	97
5.10	Calibration of the Photomultiplier Output to Laminar Flame Area	101
5.11	Calibration of Photomultiplier Output to Mass Burning Rate	101
6.1	Dependence of Maximum Pressure Rise on Ignition Time Intensity (Integral Scales Fixed at Ignition)	106
6.2	Dependence of Time to Reach Maximum Pressure on Ignition Time Intensity (Integral Scales Fixed at Ignition)	108
6.3	Time for Flame to Reach a 4 cm Flame Radius for Varied Ignition Time Intensity and Fixed Integral Scales	109
6.4	Times to Peak Pressure and 4 cm Flame Radius for Varied Ignition Time Integral Scale, Fixed Intensity (Stoichiometric Only)	111
6.5	Turbulent Burning Velocity Dependence on Instantaneous Intensity and Integral Scale	114
6.6	Fitting the Intensity Dependence of Burning Speed to Integral Scale	114
6.7	Correlation of Burning Speed Ratio to Instantaneous Intensity and Scale	117

FIGURE	FIGURES (continued)	PAGE
6.8	Comparing the Correlation to Lean Mixture Data	118
6.9	Comparing Data From the Present Study to Other Sources	122

LIST OF TABLES

TABLE		PAGE
4.1	Decay Constants for Turbulence Beyond 10 Dia.	60
4.2	Constants for Growth of Integral Scale	71
4.3	Constants for Growth of Taylor Microscale	71
4.4	Constants for Growth of Kolmagorov Microscale	71
6.1	Dependence of Burning Speed on Intensity as it Varies With Scale	115

NOMENCLATURE

a	equivalent radius of the combustion chamber if it was spherical.
A/D	analogue to digital converter
b	bar width of a lattice type screen
CFR	acronym for Cooperative Fuel Research
D	diameter
E(n)	streamwise power spectrum of turbulence
f.p.s	frames per second (framing rate of the high speed camera)
i.p.s	inches per second (tape speed of the FM recorder)
k_u	specific heat ratio of the unburned mixture
l	large eddy scale of turbulence
M	mesh width of lattice type screens
n	frequency
n_i	initial number of moles of mixture
P	instantaneous pressure
P_e	maximum pressure reached
P_i	initial pressure
r_b	radius of the spherical burned gas volume
r_i	nominal radius of unburned gas which after burning has a radius r_b
Re_Λ	$= u' \Lambda / \nu$, Reynolds number of turbulence based on integral scale
Re_λ	$= u' \lambda / \nu$, Reynolds number of turbulence based on Taylor microscale.
$R_E(t)$	streamwise autocorrelation function of turbulent velocity fluctuation
S_t	turbulent burning velocity
S_u	laminar burning velocity

NOMENCLATURE (continued)

T_i	initial temperature
T_u	instantaneous temperature of the unburned mixture
u	simplified symbol for intensity (RMS fluctuation velocity)
u_x', u_y'	fluctuation components of the instantaneous velocity in the x and y directions
u_{xy}	$= (u_x'^2 + u_y'^2)^{1/2}$, modulus of the fluctuation velocities in the x-y plane
u_x	$= (\overline{u_x'^2})^{1/2}$, root-mean-square of the fluctuation velocity in x (streamwise) direction, also called intensity
$\overline{u}_x, \overline{u}_y$	mean components of the instantaneous velocity in the x and y directions
V	mean velocity of the perforated plate in the combustion chamber; or the bulk wind tunnel = flowrate / cross sectional area
V_b	burned gas volume at any time during combustion
V_i	nominal volume of unburned gas which, upon burning becomes the burned volume V_b
V_t	total volume of the combustion chamber (1883 cm ³)
X	instantaneous mass fraction burned
ϵ	turbulent dissipation rate
η	Kolmagorov dissipation scale of turbulence; this symbol was also used as dummy parameter in Ch. 6
ν	kinematic viscosity
λ_f	Taylor streamwise length microscale of turbulence
τ_E	Taylor streamwise time microscale of turbulence
Λ	Simplified symbol for integral length scale of turbulence
Λ_f	Streamwise integral length scale of turbulence
\mathfrak{s}_E	Streamwise integral time scale of turbulence

1. INTRODUCTION

It has long been apparent that in-cylinder turbulence could improve internal combustion engine performance through increased burning rates, improved charge homogeneity, and decreased cycle to cycle variability [1,2]. It was recognized that optimizing combustion chamber aerodynamics is a significant engine design criterion. Since the effect of turbulence on burning parameters has not been clearly understood, this aspect of engine design has relied heavily on empirical data and experimental engine trials. As the conventional "cut and try" approach to engine design gives way to more sophisticated theoretical approaches, combustion models coupled to in-cylinder turbulence estimates begin to receive considerable attention for combustion chamber optimization.

Measured laminar burning velocity is used as an input to most physical combustion models, along with a correction or correlation for the effect of turbulence on flame propagation rate. While measured values for laminar burning velocity are becoming uniform in current research, the relationship between turbulent flame propagation rate and the turbulence which promotes it is still not well defined. The situation is particularly difficult in closed combustion systems such as engine cylinders where turbulence levels vary rapidly during combustion due to turbulence decay and rapid compression.

The chief objective of this study was to examine flame growth in a closed system where there is rapidly decaying turbulence, and to gather data on turbulent flame propagation rates suitable for input into engine combustion models. Ideally such data should be measured under engine like conditions. However, because of the many interacting effects of turbulence, compression, and ignition in an engine cylinder, the direct effects of turbulence on burning speeds are difficult to isolate in such a system. Furthermore, actual turbulence levels in an engine are difficult to measure.

In order to systematically measure the effects of turbulence on confined combustion, the turbulence parameters must be predictable and well defined. They should in addition be independently controllable as far as possible. In the present study, turbulence was induced by the motion of a perforated plate through a premixed gaseous charge inside a centrally ignited closed bomb. The intensity and scale of the resulting homogeneous turbulence is easily characterized. Relatively high intensity turbulence could be induced without adding the complicating effects of mean flow. Both the intensity and scale of turbulence at ignition could be independently controlled by varying plate speed, plate perforation size, and ignition timing after plate motion. Burning was monitored using pressure-based diagnostics, and photometric measurements of the growing flame were afforded through optical glass windows. This work

is a continuation of work initiated by Checkel and Thomas [3,4] who used a similar apparatus.

The next chapter reviews the literature which provided the background for this thesis, while Chapter 3 details the design and construction of the turbulent combustion cell and the data collection apparatus. The results of a detailed investigation into the turbulence generated in the cell are then presented in Chapter 4. Chapter 5 discusses the methods used for measuring flame growth and flame speed in the combustion cell. Chapter 6 reports the experimental results of the effects of turbulence on peak pressure, burning duration, and instantaneous burning velocity. An experimental correlation for burning speed against turbulence intensity and integral scale is presented. This work is summarized and the conclusions are submitted in Chapter 7.

2. BACKGROUND FOR THIS STUDY

2.1 LAMINAR BURNING SPEED

Laminar burning velocity has been investigated extensively for the past fifty years and measurements encompass a wide range of combustible mixtures. Early experiments were performed chiefly with open burners and tubes and many of those results were summarized by Gibbs and Calcote [5], as well as Andrews and Bradley [6]. An overview of much of the early flame speed measurements is offered in Lewis and von Elbe [7], who also describe a simple method for deducing flame speed in a closed, spherical vessel from the pressure rise rate. This assumes a thin shelled flame and is based on the estimate of mass fraction burned from pressure rise derived in 1917 by Flamm and Mache [8].

Metghalchi and Keck [9] used the closed bomb approach to measure laminar flame speed of propane-air mixtures over a range of temperatures and pressures. This work was extended by these authors to other hydrocarbon fuels [10], where corrections were introduced to account for heat lost to the walls and radiant energy transfer away from the flame. Several other sources of similar bomb type measurements are also noted in [10].

In general these studies agree that laminar flame speed in hydrocarbon-air flames is highest in slightly richer than stoichiometric mixtures and decreases with air dilution until a limit is reached where the flame is not

self-sustaining. This lean limit varies little with hydrocarbon fuel type. Dilution of the combustible mixture with non reacting components also reduces burning velocity. Laminar flame speed increases strongly with temperature and may increase or decrease weakly with increasing pressure. The temperature-pressure dependence varies little with mixture strength and hydrocarbon fuel complexity. The temperature-pressure dependence also remains relatively unchanged between atmospheric room temperature conditions and those in an engine cylinder [9,10].

2.2 TURBULENT FLAME GROWTH

The laminar flame has a smooth surface and a thin reaction zone, and the propagation rate is determined by the chemical and thermodynamic properties of the mixture. With the presence of turbulent fluid motion, the flame is no longer smooth, the reaction zone is apparently thicker than that of the laminar flame, and the propagation rate is greatly increased.

An appraisal of various theoretical models of the turbulent flame compared to empirical evidence was offered by Andrews and Bradley [11], where correlation of flame speed to turbulence Reynolds number based on microscale, Re_λ , is suggested. There are two general regimes used in modelling turbulent flame structure in premixed gases:

- 1) the reaction sheet regime, where turbulence simply stretches and wrinkles the laminar flame, thereby

increasing flame area and thus growth rate.

- 2) the distributed reaction zone regime, where the reaction zone is extended by turbulent transport of heat and reacting species.

It was concluded [11] that for a turbulent Reynolds number greater than about 100, the wrinkled flame structure is unlikely. A theory of turbulent flame propagation accounting for both wrinkling and diffusion was developed by Abdel-Gayed and Bradley [12]. A review of the various theoretical models is also offered by Abraham et al [13] who examined criteria for the two regimes and concluded that under engine-like conditions there is no clear evidence to suggest a separation of the two regimes, and either or both may be equally valid for different operating conditions.

There are three basic categories of empirical turbulent flame growth data: steady flow experiments with burners, ducts and edge flows; measurements in engines under controlled operating conditions and variable geometry; and constant volume bomb methods, where either steady state or decaying turbulence may be induced. Hot wire anemometry remains the most common means of quantifying turbulence parameters in all three approaches, although recently developed laser based methods are now more often applied. Hot wire anemometry has the advantage over laser based methods in its greater efficiency of data acquisition (turbulence parameters are easily extracted from the continuous analogue signal), but both hot wire and

laser-doppler anemometry share the important drawback of greater uncertainty in situations of little or no mean flow, as is the case in most closed bomb and engine studies. This aspect of anemometry will be discussed in Chapter 4.

Steady flow experiments in burners and ducts have the distinct advantage of easily measured and controlled turbulence. Since the turbulence is superimposed on a mean flow, hotwire anemometry may be reliably applied. Variation of flowrate and obstruction geometry enables direct control of turbulence intensity and scale. The disadvantage is that there is an upper limit to the gas velocity and thus the intensities generated, since an anchored flame must be maintained. Also, ignition and evolution of the flame is difficult to study in such systems. The large body of burner type experiments are typified by those of Fox and Weinberg [14] and Ballal and Lefebvre [15] where flame speed was measured for varying intensity. The latter also made a detailed study of the effect of turbulence scales.

Flame speed measurements by Lwakabamba [16] and by Abdel-Gayed et al [17,18] were performed using a cylindrical bomb continuously stirred by four wall mounted fans. Fuller [19] employed a bomb stirred by a central rotor to study global reaction rates. One drawback of the continuous turbulence bomb approach is that it may not be appropriate to apply the results to engine combustion modelling. Engine cylinder turbulence production has essentially ceased prior to ignition, and the turbulence is decaying. In the fan

stirred combustion chamber, the flame-turbulence interaction is masked and possibly reduced by the continuous production of fixed scale and intensity turbulence. Also, phenomena associated with rapid compression may occur on a significantly different scale, owing to the large volume occupied by the fans and ancilliary apparatus.

Ohigashi et al [20] used a flat disk shaped bomb with geometry similar to that of an engine cylinder, where one-shot turbulence generation was provided by a perforated plate drawn rapidly across the combustion chamber prior to ignition. Flame propagation rates in the subsequent decaying turbulence were measured with high speed photography, and different plate perforation sizes afforded control of turbulence scale, but only for qualitative comparison. Measurements of combustion duration and flame area growth rate by Checkel and Thomas [3,4] were made in a cubical bomb across which perforated plates were drawn to generate a decaying turbulence field. The significance of this apparatus was that the turbulence field was independently variable and free flame travel could be observed over distances typical of an engine cylinder.

Turbulent flame speeds have been deduced from pressure traces in a CFR (Cooperative Fuel Research) engine by Lancaster et al [21] assuming a spherical thin shelled flame. Turbulence conditions were measured for motoring (no combustion) conditions using hot-wire anemometry by Lancaster [22]. A similar approach was used by Groff and

Matekunas [23] in more conventional engine geometries. Compression enhancement of the turbulence was addressed with corrections applied to the intensity. These corrections were based in part on the theoretical study of Hoult and Wong [24] on the effect of rapid compression on turbulence in a cylindrical volume. This was essentially an application of Townsend's [25] rapid distortion theory. There is a comprehensive review of engine turbulence and burning rate studies offered in [23].

All of the bomb, burner and engine studies agree that there is a very strong and close to linear increase in burning speed with turbulence intensity, but the strength of the correlation varies considerably among the sources. The effect of scale when reported is weak, and both positive and negative correlations to integral scale have been documented. It is generally held that the turbulent to laminar burning speed ratio appears independent of mixture strength. Turbulence intensity is deemed more important than the laminar burning velocity of the mixture in determining turbulent flame speed.

2.3 TURBULENCE GENERATION BY PERFORATED PLATES

The present study uses a closed bomb apparatus where one shot turbulence is generated by the movement of a perforated across the interior of the cubical combustion chamber. This apparatus is based on the design of Checkel [26] and has an advantage over other bomb and engine studies since the

difficulties of measuring turbulence where there is no mean flow is circumvented. The turbulence in the wake of the perforated plates may be measured in an analogous wind tunnel geometry where hot wire anemometry is more reliably applied.

Grid induced turbulence is well documented in the literature, and much of the subject matter is covered by Hinze [27]. Theoretical work on the decay of isotropic turbulence was pioneered by Taylor [28] and von Karman and Howarth [29] in the 1930s, later extended by Frenkiel [30] among others. Considerable experimental work was performed by Baines and Peterson [31] and Uberoi and Wallace [32] with a wide variety of screens, grids, and perforated plates to test theoretically predicted isotropy and decay rates. Turbulence decay rate in the wake of a perforated plate in a closed vessel was observed by Tsuge et al [33] to be similar to that in the wind tunnel.

Checkel [26] reported hot wire measurements in the wake of perforated plates both in the cubical combustion cell and in the wind tunnel. Using a statistical model for hotwire response in vanishing mean flow to extract turbulence parameters, good agreement was shown between turbulence decay in the wind tunnel and in the cubical cell.

2.4 OBJECTIVES OF THIS STUDY

The intent of the present experimental study was to observe turbulent combustion phenomena using the closed bomb

approach where homogeneous and decaying turbulence can be generated in a controlled manner, and turbulence parameters easily quantified. The experimental apparatus has the same design as that of Checkel and Thomas [3,26], where a perforated plate is pulled across a centrally ignited cubical combustion chamber prior to ignition. The apparatus is described in detail in the next chapter.

Checkel's original work concentrated on turbulent flame area growth rates and combustion durations, and the results were directed toward considerations in lean burning engine design. The present study extends this work in an attempt to gather more general data on turbulent burning speeds as a function of turbulence intensity and scale. The use of pressure derived flame speed measurement was evaluated by comparison to high speed photography and flame arrival detection. Checkel's concept for photomultiplier based flame growth monitoring was also tested. Detailed measurements were performed behind the perforated plates in a wind tunnel as well in the combustion cell to confirm Checkel's [26] data.

3. TURBULENT COMBUSTION APPARATUS AND INSTRUMENTATION

The design of this experiment evolved directly from the original work by Checkel [3,4] with improvements made in combustion cell construction, timing electronics, and sensor apparatus. A different charge preparation scheme was employed to reduce mixture uncertainty and variability.

In the first section of this chapter, the construction of the combustion cell and the associated turbulence generation equipment is outlined. Also described here are preparation and admission of the combustible charge. In the next section the various sensors used to monitor combustion phenomena are discussed, followed by an explanation of the recording, processing and storage of transducer signals. The final section relates the apparatus and procedure for measuring turbulence produced in the combustion chamber.

3.1 CONSTRUCTION OF THE COMBUSTION CELL

The combustion cell, shown in Figure 3.1, was machined from a solid block of 6066-T6 aluminum alloy to form a 125 mm cube chamber enclosed by walls 25 mm thick. A 25 mm thick removable plate fitted with an O-ring seal is rigidly bolted over the open end.

Two windows of PK-7 optical glass, 110 mm in diameter and 30 mm thick, are mounted flush with the inner walls on opposite sides of the chamber to allow either schlieren photography of the growing flame, or simultaneous direct

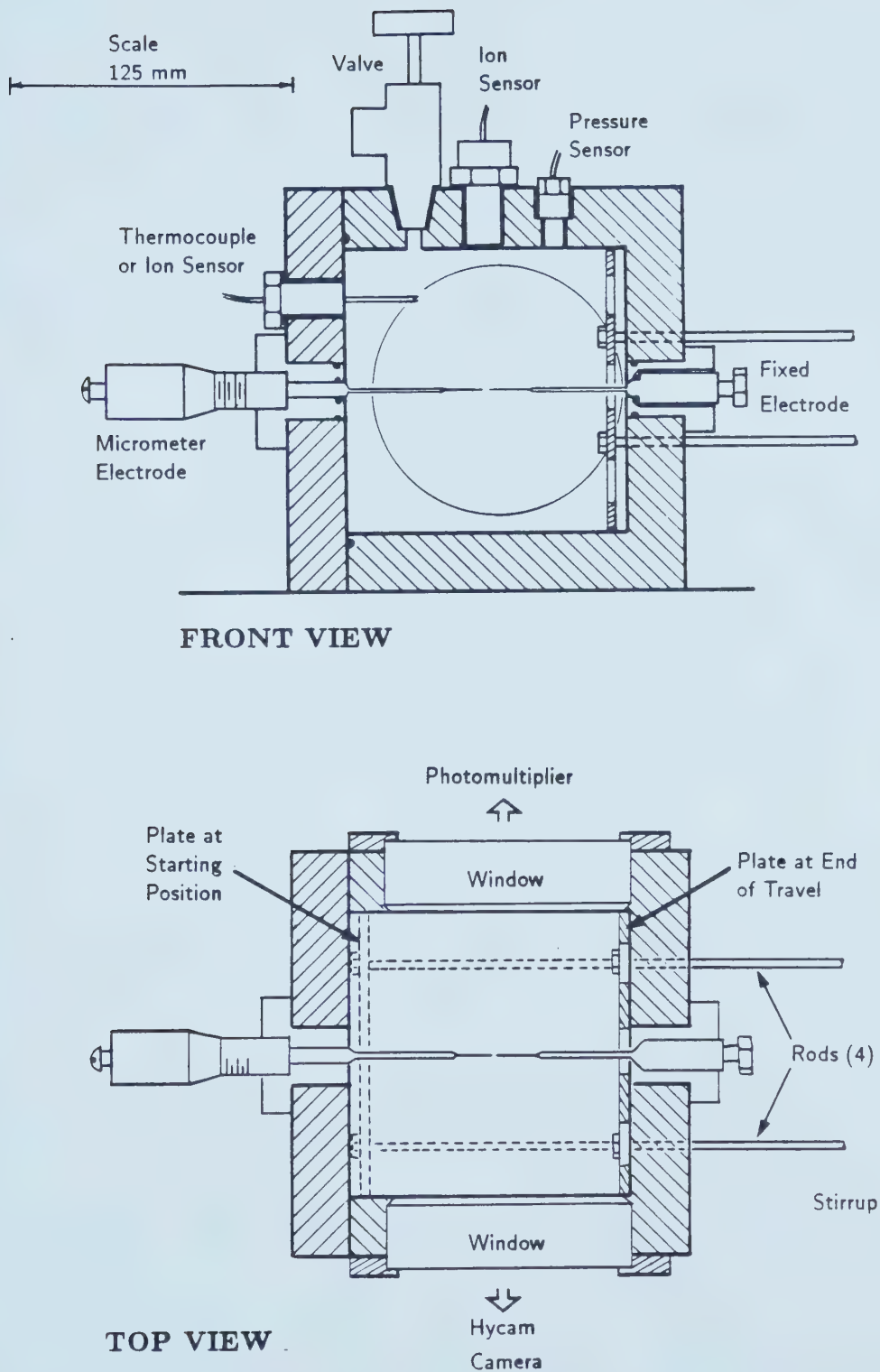


FIGURE 3.1

Layout of the Turbulent Combustion Cell

photography and light intensity measurement. In the present study only the latter strategy was used.

On the top of the cell are mounted a needle valve for filling and evacuation, an ionization detector to sense flame arrival at the wall, and a piezoelectric pressure transducer. A chromel-alumel thermocouple is mounted through the removable end plate to read the initial mixture temperature.

There are four 6 mm dia. rods passing through teflon glides sealed with lubricated O-rings in the rear of the cell. These rods are fixed to the perforated plate which is drawn across the chamber to induce pre-ignition turbulence.

The ignition spark gap is formed at the center of the chamber between electrodes extending from opposite ends of the cell and passing through a central hole in the turbulence generating plate.

The combustion cell, plate motion apparatus, and optical equipment are all mounted on a rigid steel frame which is anchored to the concrete floor. This measure is necessary to maintain alignment of the optics during the shock of plate motion.

Accounting for the perforated plate, electrodes, and machining fillets in the cell's interior, the total gas volume of the cell is 1882 cm^3 . Static pressure testing of the cell with all equipment mounted proved the integrity of seals from vacuum to 20 atm with no discernible leakage.

3.1.1 TURBULENCE GENERATION PLATES

The 125 mm square perforated plates (Figure 3.2) used to generate turbulence were fabricated from an aluminum alloy 5 mm thick, providing the ruggedness to withstand the high stresses encountered during the rapid traction of the plate across the cell.

Four plates were manufactured with hole diameters of 2.5, 5, 10, and 20 mm, each with the same grid pattern resulting in a 60% blockage ratio. Each plate has a central hole through which the spark electrode passes when the plate is moved. It will be shown that these plates provide a range of turbulence scales similar to those generated in a conventional spark ignition engine prior to ignition.

3.1.2 PLATE MOVEMENT APPARATUS

The mechanism for pulling the perforated plate at controlled, uniform speeds across the combustion chamber is illustrated in Figure 3.3. The impetus for plate motion is provided by the momentum of a 30 kg flywheel driven by a variable speed DC motor. The 30 cm diameter flywheel was constructed from two 2.5 cm thick disks with a 6 mm thick steel bar clamped between. One end of the bar extends 2.5 cm beyond the flywheel rim to form a tooth which will give slightly upon impact due to clutch-like slippage between the disks.

During flywheel rotation before the system is triggered, the tooth passes freely through a slot in a stirrup which

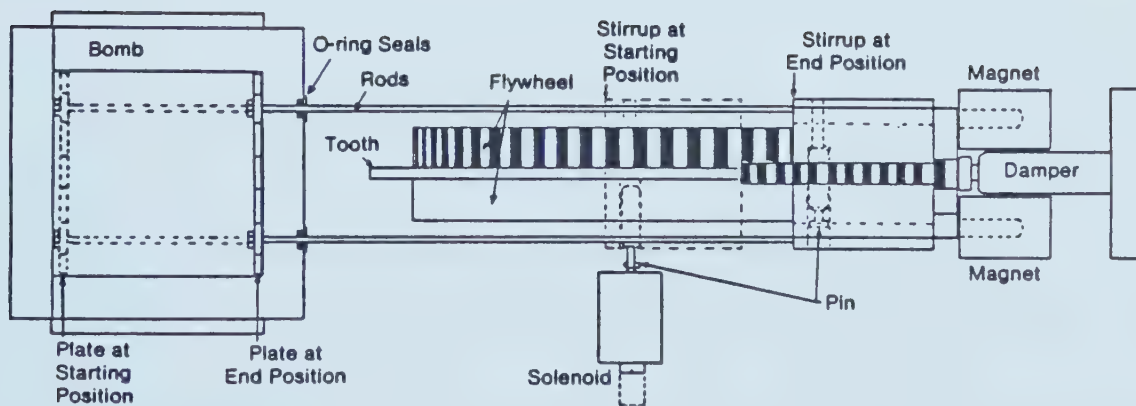
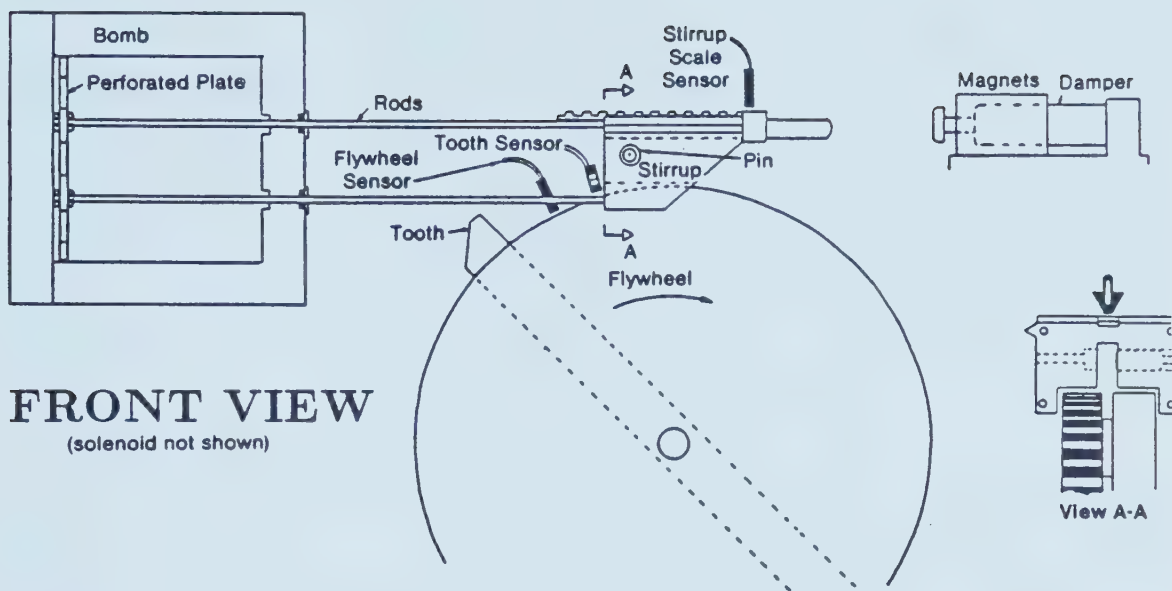


FIGURE 3.3

Mechanism for Perforated Plate Movement

slides along a horizontal track. This stirrup is directly connected to the the turbulence generating plate in the combustion chamber by the four rods which pass through the rear of the cell. When plate motion is electronically triggered, a solenoid propels a steel pin across the stirrup slot to engage the flywheel tooth. Velocity measurements of the stirrup show that the resulting acceleration of the stirrup-plate assembly may be as high as 200 g.

During the 80% of plate travel when the flywheel tooth remains engaged, a uniform velocity is maintained by the momentum of the flywheel. The stirrup is drawn through the remaining 2.5 cm of travel by its own momentum and by the traction of two electromagnets energized synchronously with the tooth pin solenoid. These magnets also serve to prevent rebound of the plate by freezing the stirrup in the end position.

A hydraulic shock absorber reduces excessive, potentially damaging impacts during deceleration of the stirrup-plate assembly. The shock absorber position is adjustable to allow a longer damping stroke for higher plate speeds.

Also depicted in Figure 3.3 are the locations of photo-transistor sensors used to monitor the motions of the plate movement apparatus. The sensor which detects the flywheel tooth just before it passes through the stirrup slot is important in the electronics triggering plate motion, and the photo-transistor signalling the mid point of

plate travel provides the reference for spark timing electronics. Flywheel speed is continuously monitored with a tachometer on the output of the photo-transistor activated by sixty stripes painted on the flywheel rim, while the actual plate position and speed is deduced from the recorded output of the sensor focused on stripes at 10 mm intervals on the stirrup.

The consistency of plate speed across the combustion chamber for various flywheel speed settings is seen in Figure 3.4. Note that "plate position" is the distance of the leading edge of the plate from the chamber wall where the plate initially rested. The plate begins its traverse at 10 mm owing to the combined thickness of the grid plate and the nuts which fix it to the stirrup-rods.

Plate velocity calculated at each 10 mm interval was averaged over the range of points (20 to 110 mm) to get the average plate speed used in later turbulence calculations. The average plate speed as a function of flywheel speed was repeatable within about 5%, so a desired plate speed could be obtained with reasonable reliability using the appropriate flywheel speed setting.

3.1.3 TRIGGERING PLATE MOTION

The electronics for triggering plate motion, shown schematically in Figure 3.5, rely on the flywheel tooth sensor to sequence plate motion events. The low-going pulse from the tooth sensor is inverted and sharpened with a

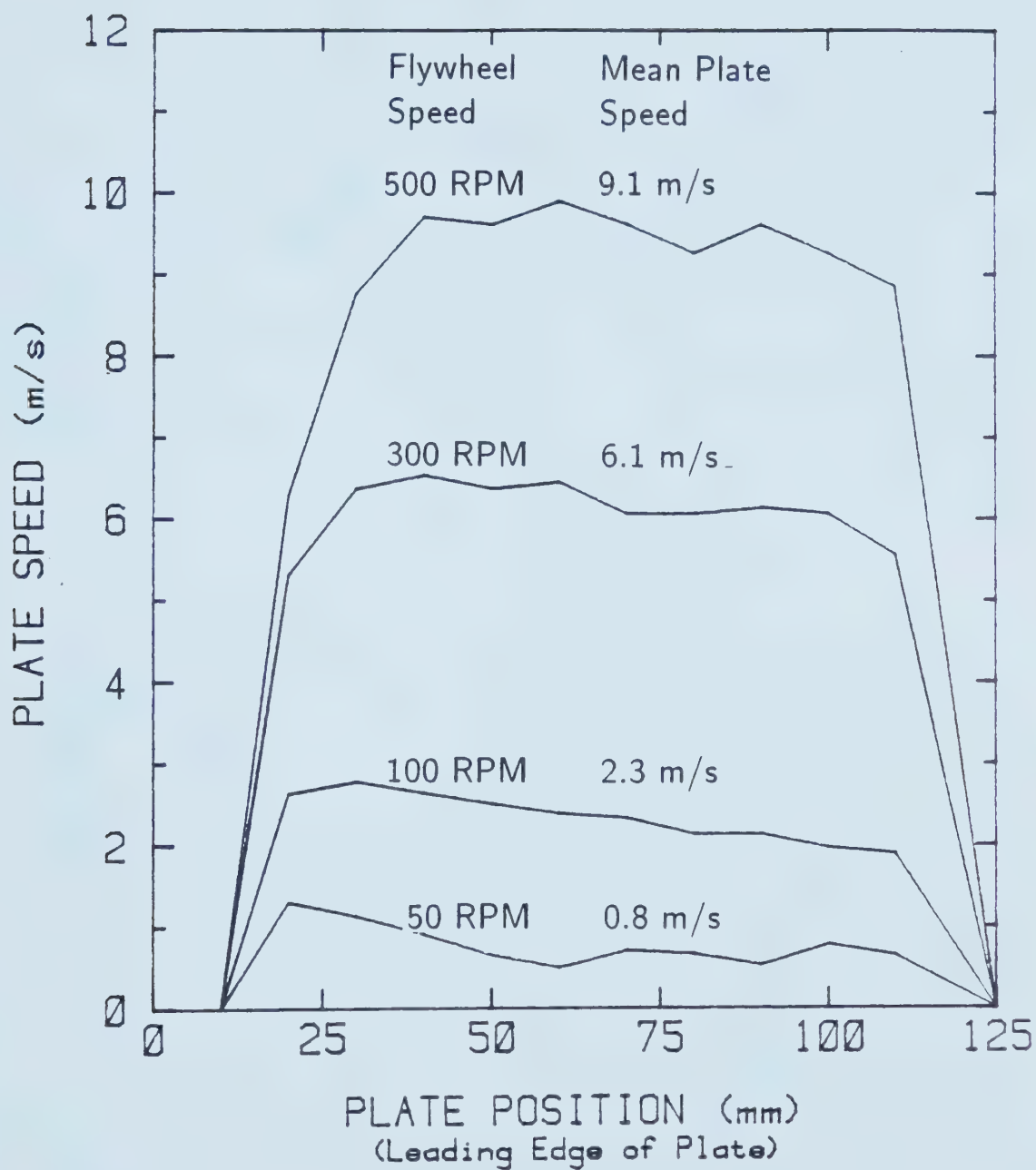


FIGURE 3.4

Speed of the Perforated Plate Across the Combustion Chamber

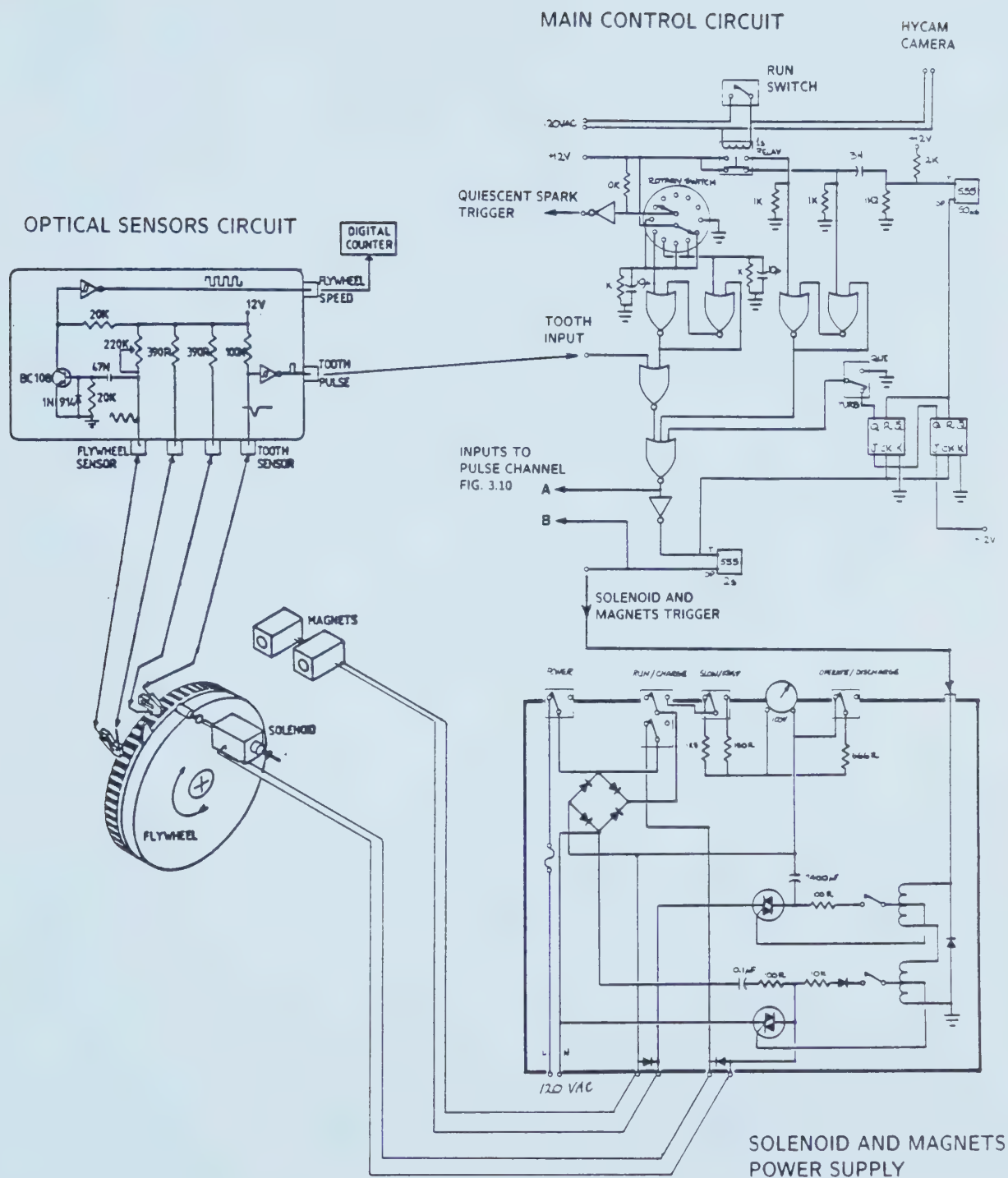


FIGURE 3.5

Electronics for Controlling Perforated Plate Motion

Schmitt trigger before being fed into the main control box where plate motion is triggered.

When the "run" switch on the main control box is made, the high speed framing camera (when used) is activated, and a timed relay allows a one second camera speed-up interval before "run" mode logic is initiated. When the tooth is next detected, a $50\ \mu\text{s}$ delay (allowing the tooth to clear the stirrup) precedes a 2 s pulse to the magnets and solenoid power supply. This causes a capacitor to discharge through the solenoid, firing the pin across the stirrup slot to engage the flywheel tooth on its next pass. The electromagnets are energized for the duration of the 2 s pulse to ensure the stirrup remains in its end position.

3.1.4 IGNITION SYSTEM

The high energy, capacitive discharge, coil spark generating circuit shown in Figure 3.6(a) was used in conjunction with the adjustable platinum tipped electrode pair shown in Figure 3.6(b).

The electronic trigger pulse activates the SCR, allowing the capacitor bank, charged to 400 V, to discharge through the primary windings of a standard automotive coil to produce the spark across the electrodes. An additional $1.5\ \mu\text{F}$ capacitance may be added to the base of $1\ \mu\text{F}$ for a stored energy range of 80 to 200 mJ.

Although capacitance, charging voltage, and spark gap are all adjustable, they were fixed for the present study at

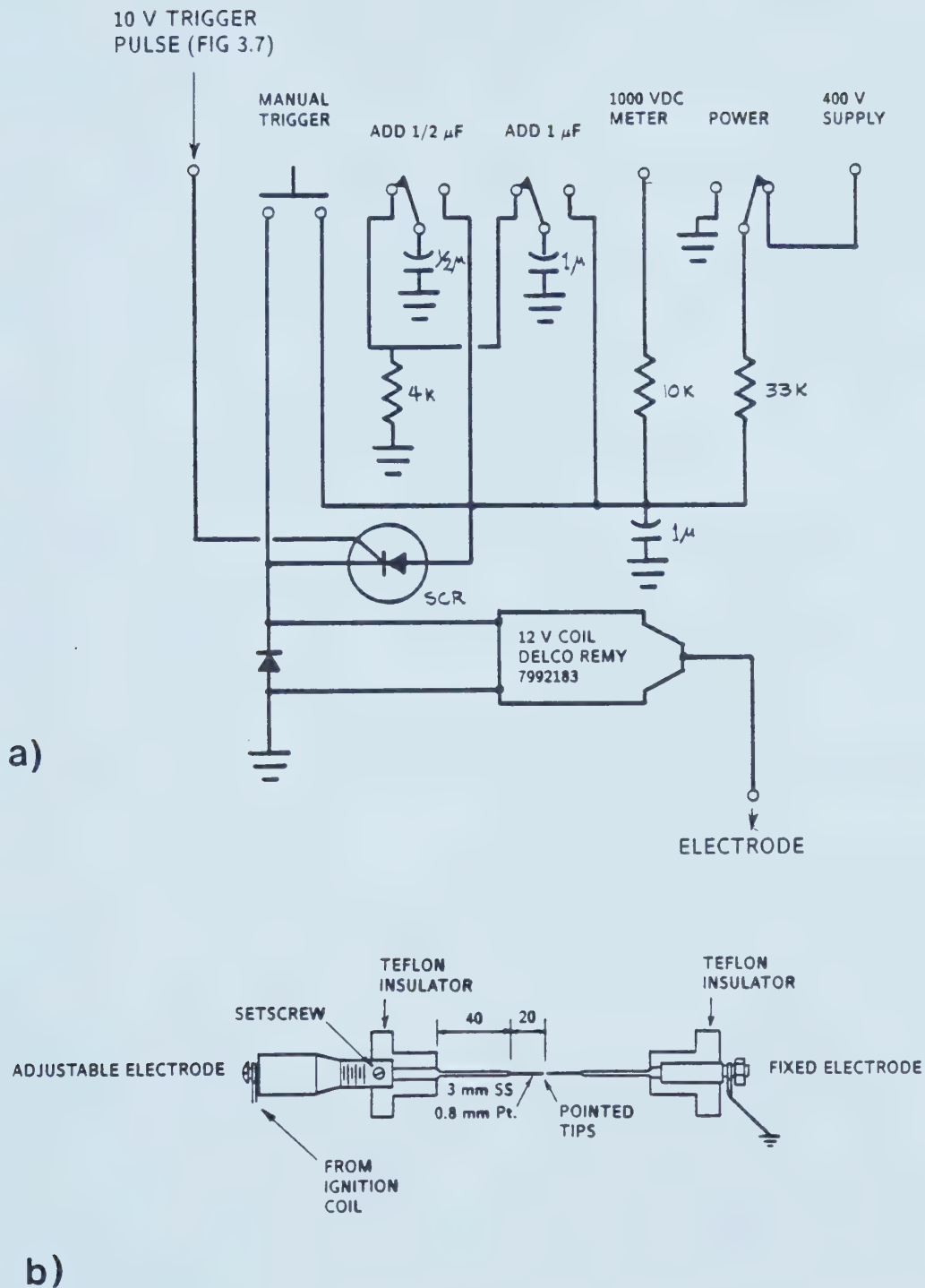


FIGURE 3.6 Ignition Circuit and Electrode Detail

2 μF , 400 V, and 1 mm respectively (stored energy of 160 mJ).

3.1.5 IGNITION TRIGGERING SYSTEM

The system for ignition triggering in either turbulent or quiescent modes is shown in Figure 3.7.

For turbulent mode spark triggering, the output from the photoswitch, activated when the leading edge of the plate is at the centre of the combustion chamber, is sharpened and inverted before input to the variable delay pulse unit. This device has a resolution of 1 μs , and a range of 10 s. The delay was preselected in conjunction with predicted plate speed and known turbulence decay functions to trigger ignition at the desired turbulence level. The outgoing pulse of the delay unit is 10 V, with 1 ms duration.

For non-turbulent runs, a manual rotary switch and inverter provide the high-going trigger pulse which is also fed into the delayed pulse unit, but with a zero delay selected. In this case, the delay unit serves as a simple thyristor-driver for the ignition circuit. The rotary switch also serves to simulate tooth-sense logic (Figure 3.5) monitored on the pulse channel of the data recorder. This provided similar timing records for turbulent and quiescent runs and simplified later computer analysis of records.

3.1.6 MIXTURE PREPARATION

The homogeneous premixed charge for the combustion cell

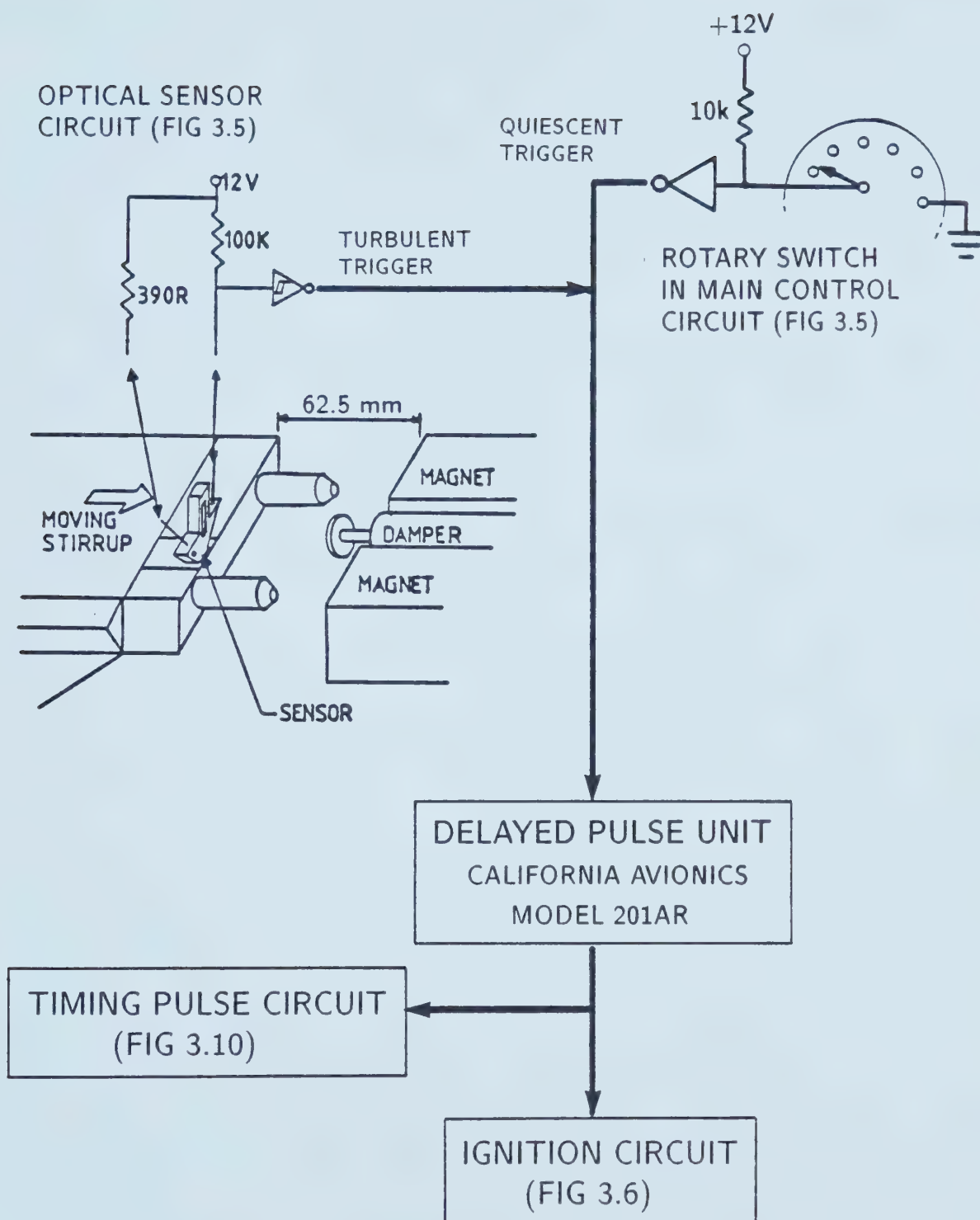


FIGURE 3.7

Ignition Triggering Electronics

was prepared with the system shown in Figure 3.8 which mixes independently controlled flows of fuel gas and air. The gases are supplied by pressurized cylinders containing extra dry air, 98% "technical" purity methane, and 96% "natural" purity propane. Propane/air mixtures were used exclusively in this study.

The flow rate of each gas is controlled with the two stage regulator which adjusts the pressure upstream of a small choked flow orifice. For the choked flow condition always maintained, flow rate is independent of downstream pressure and is directly proportional to upstream pressure. Each gas flowrate was calibrated to upstream pressure (read from a Bourdon gauge with 1 kPa resolution) using rotameters and a soap bubble burette apparatus. The fuel and air flows are mixed thoroughly in a baffle before delivery to the cell, or to the Meker burner used to discard the mixture until a steady state flow of the desired mixture is reached. This apparatus delivers about five litres per minute of mixture with equivalence ratio certain to within 2%, based on the repeatabilities of gas flowrate calibrations.

The combustion cell was prepared for admission of the charge by first evacuating it and flushing it with room air to remove previous combustion products, then re-evacuating it thoroughly. The vacuum pump is capable of drawing the system within about 2 mm Hg of absolute vacuum. The remaining air was later accounted for in stoichiometry calculations.

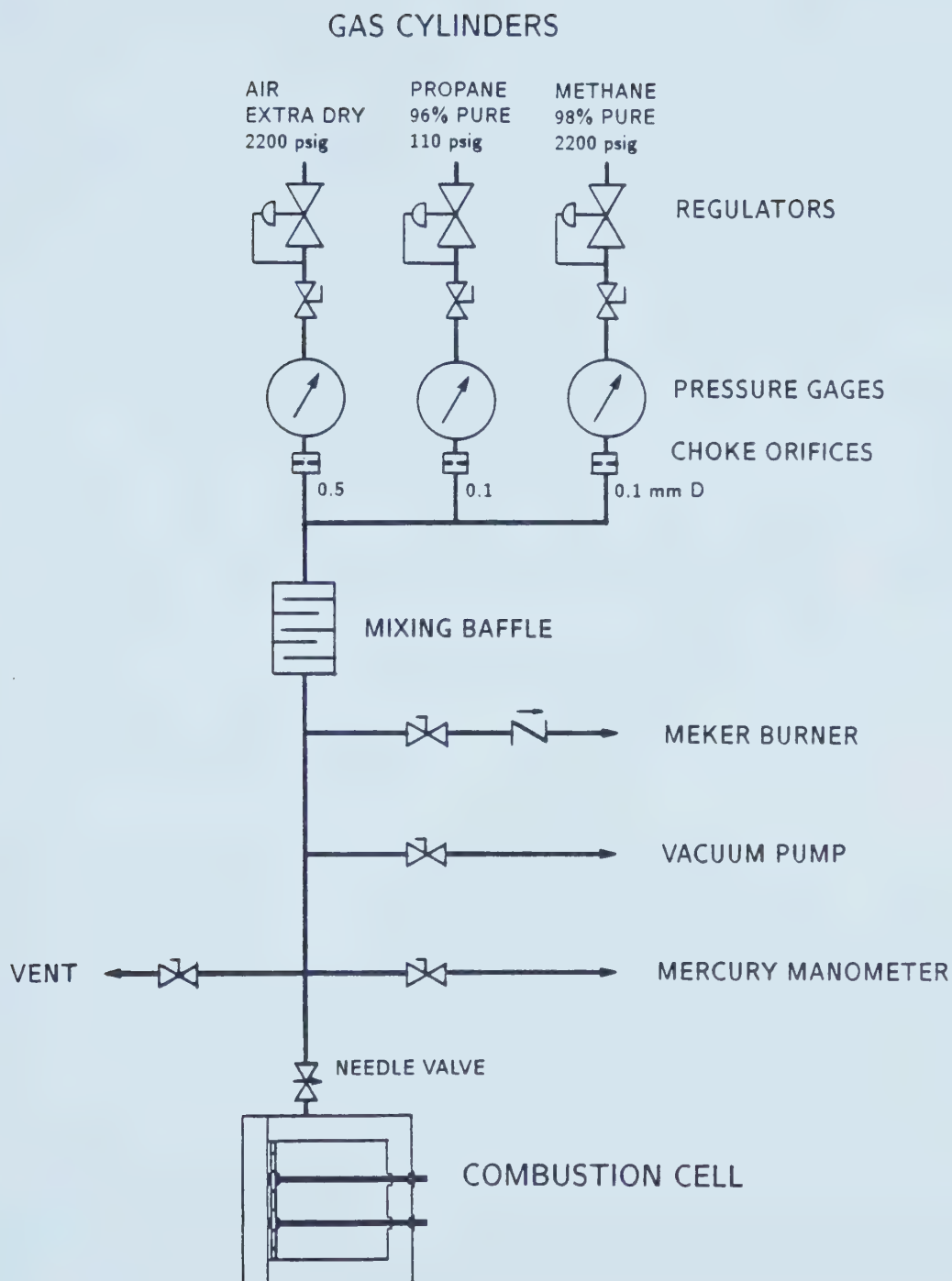


FIGURE 3.8

Apparatus for Air-Fuel Mixture Preparation

When the cell had reached maximum vacuum, the vacuum pump line was closed, and a line opened allowing the prepared mixture to gradually fill the cell to the desired initial pressure. During the evacuation and filling process, cell pressure was measured with a mercury manometer against the ambient barometric pressure checked before each run.

For the present study, initial conditions were fixed at 101.3 kPa, and ambient room temperature (23 ± 1 °C). Once cell pressure was set, and the mixture had reached thermal equilibrium with the surroundings, the combustion chamber was sealed with the needle valve atop the cell. A five minute settling period was allowed prior to ignition to remove background turbulence.

3.2 SENSORS FOR THE TURBULENT COMBUSTION CELL

Sensor signals were recorded on a four channel FM tape recorder. The recording and reduction of data are detailed later in Section 3.2.8 of this chapter.

3.2.1 PLATE SPEED SENSOR

Motion of the turbulence generating grid plate is sensed by the phototransistor (Figure 3.9(a)) focused on the alternating black and white markers at 10 mm intervals on the stirrup directly connected to the grid plate. The amplified output signal shown in Figure 3.9(b) was recorded on FM recorder channel 2.

Following the later digitization of the data channels,

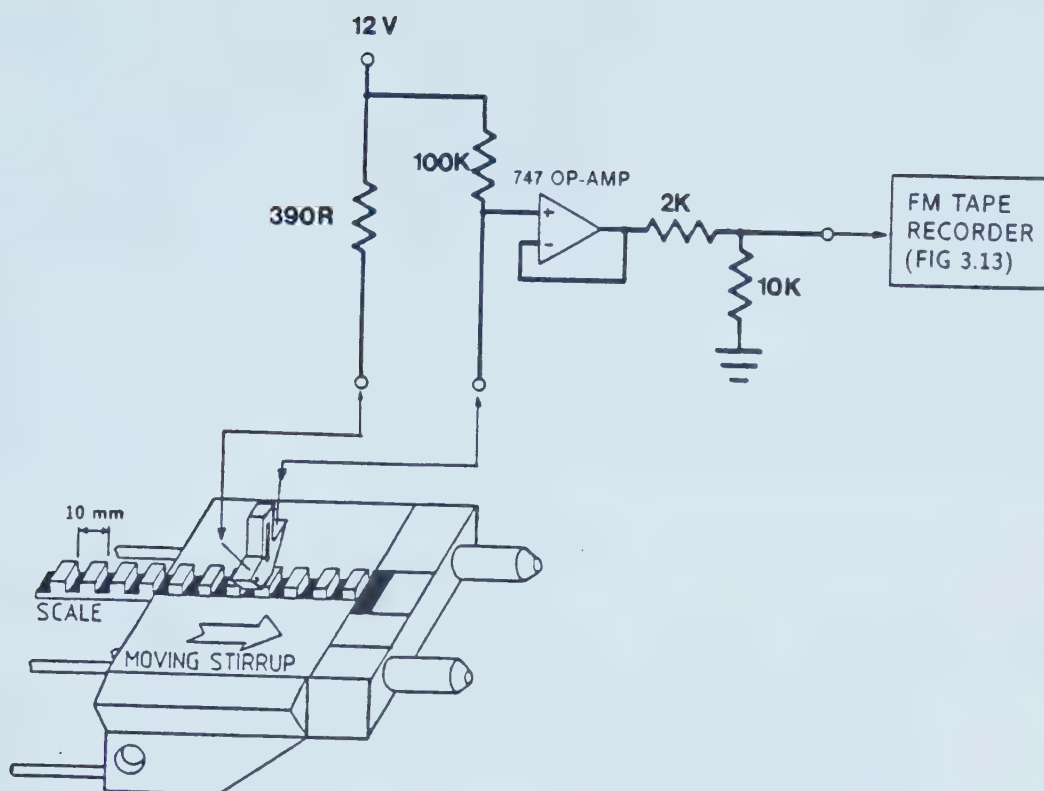


FIGURE 3.9(a) Perforated Plate Speed Sensor

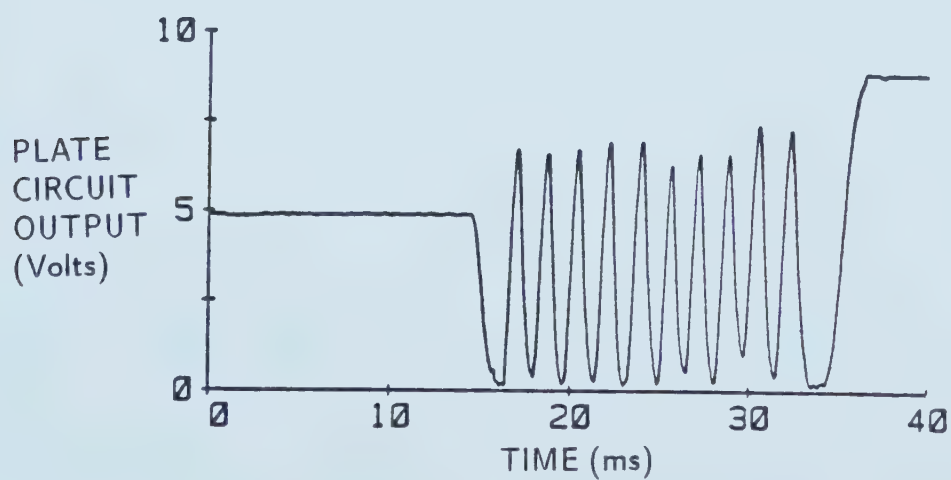


FIGURE 3.9(b) Sample Output From Plate Speed Sensor

the plate speed at each of the black markers (high peaks) was deduced by measuring the time between flanking low peaks which represents 10 mm of plate motion. This yields an array of ten velocities corresponding to plate positions of 20, 30,... 110 mm (where "plate position" is distance of the plate's leading edge from the starting wall). The average plate speed was taken as the average of these ten values.

3.2.2 TIMING PULSE SIGNAL

A timing reference signal, created with the circuit shown in Figure 3.10 and recorded on the FM recorder, marks flywheel tooth detection, the spark trigger pulse, and flame arrival detection.

When plate motion logic is in "run" mode, the first passage of the flywheel tooth starts a 2 s timer circuit and activates the tooth pin solenoid and electromagnets as previously detailed in Section 3.1.3. The timer puts the output of the pulse circuit high (8 V). The second pass of the tooth causes a low (0 V) pulse in the pulse circuit output. Another low pulse is created when the delayed pulse unit sends the spark trigger to the ignition circuit. The detection of flame arrival by the ionization sensor creates the final low pulse or series of pulses on the timing signal. To prevent registering additional tooth pulses on succeeding flywheel revolutions, a counter inhibits tooth detection pulses after the first two passes are marked.

For quiescent runs, a similar record is produced since

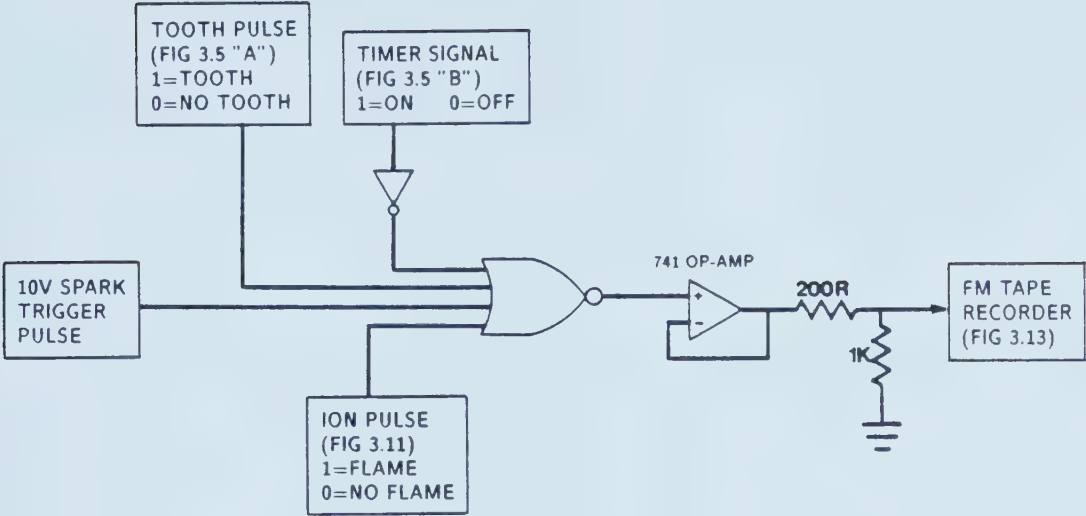


FIGURE 3.10(a) Timing Pulse Circuit

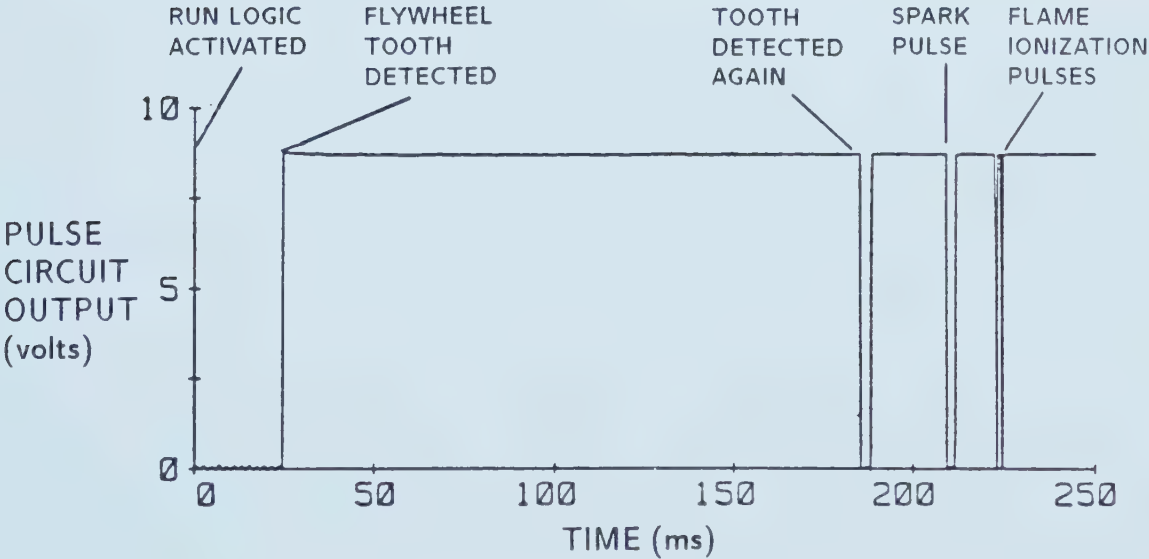


FIGURE 3.10(b) Sample Timing Pulse Signal

the timing pulse circuit was activated by the rotary triggering switch which simulates the two tooth pulses and produces the spark trigger pulse.

3.2.3 PRESSURE MEASUREMENT

Dynamic combustion pressures were measured using an AVL piezoelectric transducer (model 12QP 300CVK) specially designed for IC engine application, with a Kistler dual mode charge amplifier (model 507). The transducer has a dynamic range of 0 to 12 MPa, demonstrates linearity within 1%, and is temperature and vibration compensated. It was insulated from dynamic temperature effects with a 0.5 mm coating of silicone grease on the diaphragm.

The output of the amplifier was offset 0.5 V and scaled to give 4.0 V for 1 MPa. The difficulty of drifting offset inherent in such charge transducer systems posed no problem in the present study. The initial pressure was always known within 0.2 kPa from the mercury manometer, the calibrated linearity constant was repeatable within 1%, and finally, thermal gradients which cause most drift in engine applications were non-existent here.

The pressure signal was recorded on one channel of the FM tape recorder.

3.2.4 TEMPERATURE PROBE

A type K (chromel-alumel) thermocouple extending 1 cm

into the combustion chamber was used with a digital voltmeter and tabulated calibration data to monitor steady state mixture temperatures in the cell.

As well as providing the initial, pre-ignition temperature datum, the thermocouple was also important during admission of the charge. The gases expanding into the evacuated cell experienced a drop in temperature (Joule-Thomson effect), and the mixture had to reach thermal equilibrium with the combustion chamber walls before the cell was sealed. Otherwise subsequent warming of a sealed charge would have lead to an erroneous initial pressure reading.

No efforts were made in this study to monitor dynamic gas temperatures during combustion.

3.2.5 FLAME ARRIVAL DETECTOR

Shown in Figure 3.11 is the ionization sensor used in all combustion experiments to signal flame arrival at the wall of the combustion chamber. This datum was used to mark the period of the flame growth after which burning becomes significantly influenced by wall interaction.

The detector is composed a platinum electrode pair, 1 mm apart, across which an 40 V potential was maintained. Flame arrival at the gap provides the ionization to close the circuit, allowing a slight current flow. This current was amplified to activate a transistor, producing a low going pulse which was inverted and routed to the timing pulse

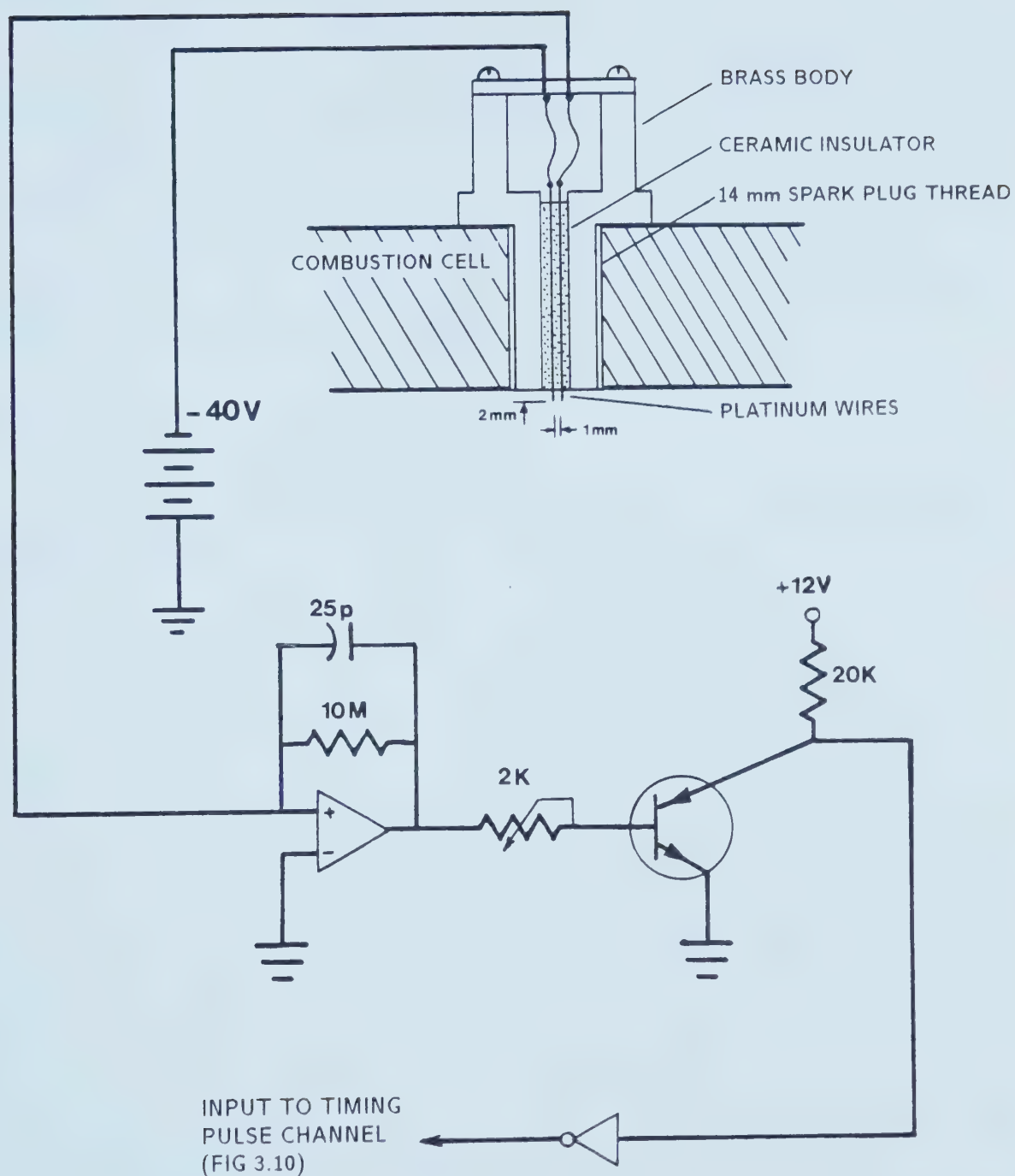


FIGURE 3.11

Flame Ionization Detection Circuit and
Sensor Detail

channel on the data recorder (Figure 3.10).

A similar detector used only in non-turbulent runs extended into the combustion chamber to sense flame arrival at a radius of 4.10 cm. This datum was used to quantify and evaluate alternate flame size measures. Because of possible damage from the vibration of plate motion, the extended sensor was not used in turbulent runs.

3.2.6 FLAME PHOTOGRAPHY

For some experiments, flame growth was photographed directly through one window of the cell using a Hycam high speed 16 mm framing camera. For optimum exposure speeds, a 50 mm f1.4 lens and 400 ASA positive color film were used.

Although the Hycam is capable of up to 11000 frames per second, filming speeds were limited in this application to less than 1000 f.p.s. so that the exposed image, registered by the luminosity of the flame itself, remained discernable. The inertia of the camera's drive necessitates a pre-event speed up interval of at least 0.5 s before the desired framing rate is reached. Exact framing speed was determined from timing markers on the film border produced by a miniature strobe lamp driven at 100 Hz.

Flame size was measured from the film with a Joyce Loebel Mark II dual beam microdensitometer, knowing the actual photographic scale established from photographs of a graduated ruler placed inside the combustion chamber.

For the present study, flame photography was used

principally in quiescent combustion experiments where various flame growth measures were compared. Only a few turbulent runs were filmed for qualitative analysis.

3.2.7 PHOTOMULTIPLIER BASED MEASUREMENTS

The intensity of light emitted by the CH radical, a species present only in the flame reaction zone, was measured with a photomultiplier through the window opposite the high speed camera. The application of this apparatus as a flame growth measure and its calibration are discussed in detail in Chapter 5.

The photomultiplier optical system is shown schematically in Figure 3.12. Light from the flame region is randomized by a frosted glass screen and by the collection optics which concentrate light from the screen onto the photomultiplier cathode without forming a focused image. This randomization is necessary since photomultiplier sensitivity is not uniform for all regions of the photocathode. Therefore every effort must be made to spread light from all regions of the flame to all regions of the photocathode to prevent excessive sensitivity to flame in certain regions of the cell. The collected light is filtered with a narrow band optical filter which removes all wavelengths except the blue light emission (431 nm) of the CH radical. Through simultaneous adjustment of the iris aperture and the photomultiplier cathode potential, the sensitivity of this system may be optimized to provide a linear response to

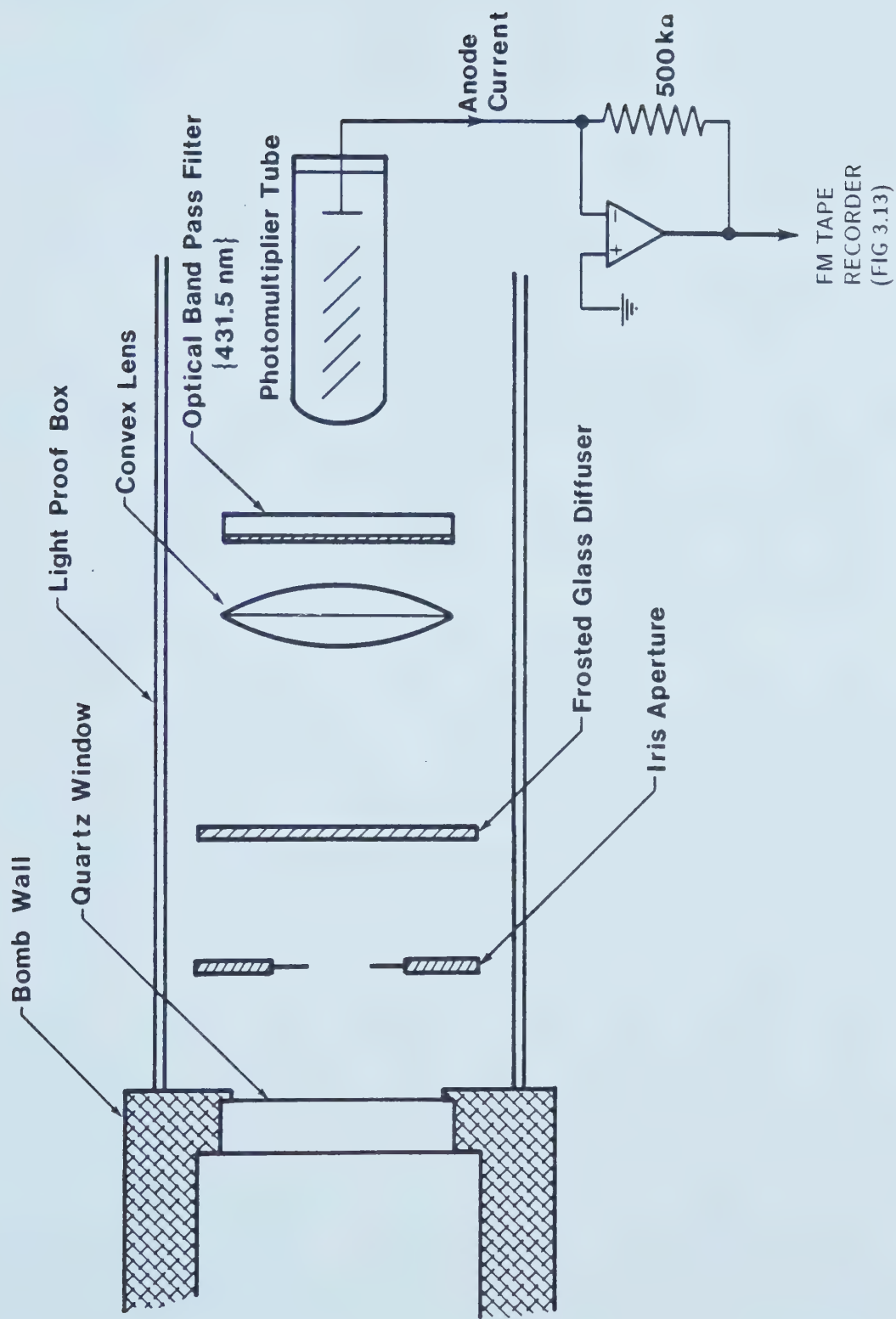


FIGURE 3.12 Photomultiplier Optical System Layout

combustion activity.

The photomultiplier current was converted to an amplified voltage output signal as shown in Figure 3.12, and recorded on the FM recorder.

3.2.8 RECORDING AND STORAGE OF DATA

All combustion experiments were recorded on a RACAL Store 4DS FM tape recorder which features variable record and replay speeds, as well as variable input and output ranges. The four recorded data signals are summarized in Figure 3.13(a). All runs were recorded at a tape speed of 60 inches per second, and using the RACAL wide-band option allowed a frequency bandwidth of 0-40 kHz.

The four channels were then replayed at 3.75 i.p.s. to the eight port analog to digital converter controlled by a Digital LSI-11/23 minicomputer (Figure 3.13(b)). The ports of the A/D are differential (non-grounded) connectors. Port 0 of the A/D was continuously sampled until the second tooth pulse of the timing pulse channel is detected - this is where useful data begins. Then the eight ports were sequentially sampled at an overall rate of 25 kHz, digitizing the data into 12 bit integers which are synchronously written to the hard disk of the minicomputer. This scheme results in an effective sampling rate of 100 kHz per recorded channel for a time resolution of 10 μ s. A total of 32000 values per channel were digitized and stored.

The combined aquisition apparatus was calibrated as a

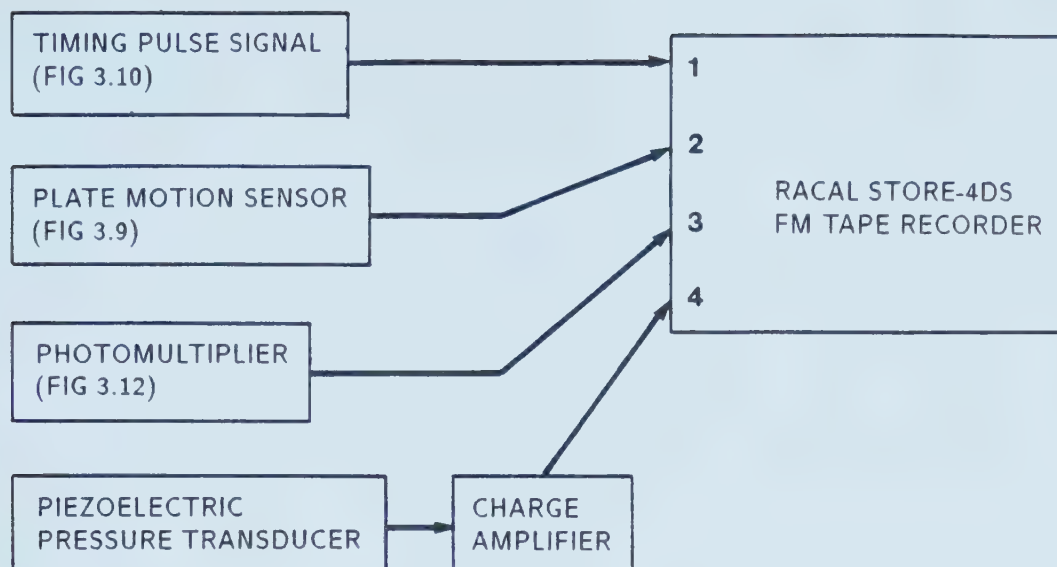


FIGURE 3.13(a) Signal Recording Summary

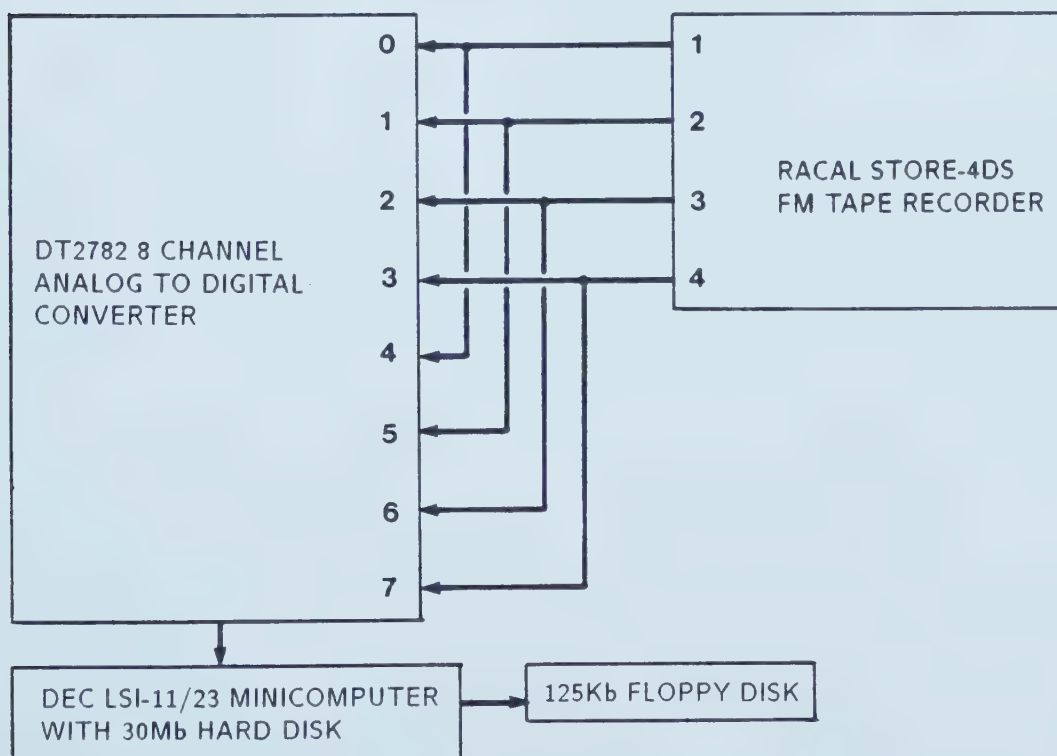


FIGURE 3.13(b) Digitizing the Recorded Signals

unit by recording known DC voltages on the tape recorder and replaying them to the A/D. A computer program calculated an A/D-recorder calibration function (A/D counts per input volt) for each of the A/D ports. This calibration was later applied in the sorting and conversion of the digitized data.

The computer was next directed to sort the serial eight port data on the hard disk into arrays representing the four recorded channels. The timing pulse channel was searched to locate and save the flame arrival time. The spark timing was not taken from this channel as originally intended, but rather from the photomultiplier output channel which shows a more highly resolved history of the actual illumination of the spark. The initial rise of the spark light was taken as the time origin for combustion records.

For turbulent runs, the plate motion data was then analysed to extract and save the array of ten plate speed values. Also retained was the time relative to the subsequent spark that the leading edge of the plate was exactly at the centre of the cell. This timing was later used with average plate speed and known turbulence decay functions to estimate turbulence levels at the spark.

Photomultiplier output data, beginning at the spark and ending where the signal has saturated the recorder input, is compressed into 512 values by central averaging. During the initial fine tuning of the photomultiplier system, this saturation point was induced to occur close to the point of flame arrival at the wall. This afforded optimum sensitivity

in the early flame growth period where the entire flame was visible through the cell windows. Photomultiplier data was converted to mV with the A/D-recorder calibration and saved in this integer form for later translation to the appropriate burning parameters presented in Chapter 5.

The pressure record was searched to locate the maximum pressure and the point where the pressure has dropped to 90% of this peak value. The maximum pressure and the time when it occurs were saved, and the pressure record from the spark to the 90% point was compressed into 512 values and saved. The pressure transducer calibration, A/D-recorder calibration, and the known initial pressure were used to convert data to $10 \times (\text{kPa abs})$. The multiplying factor was necessary to preserve resolution (0.1 kPa) with the data stored in integer form.

The 512 photomultiplier points and the 512 pressure points for each run were accompanied by a special "blueprint" array of 256 elements, set aside to contain all pertinent information about the run. This includes run number, mixture, initial conditions, data compression factors, and so on.

The 1280 value record was then transferred and stored in binary form on a specially prepared floppy disk equipped with a directory to contain condensed information on each run stored. This facility allowed rapid access and search capability where data could be extracted and condensed from several runs simultaneously using simple computer routines.

A typical record of a stoichiometric, non-turbulent propane/air explosion is plotted in Figure 3.14. The illumination of the spark is clearly evident in the photomultiplier trace.

3.3 TURBULENCE MEASUREMENTS

Hot wire anemometry was used to measure turbulence produced behind the perforated plates used in the combustion cell. The limitation of such measurements is that they become questionable when the turbulence fluctuations are not superimposed on a mean flow. For this reason, extensive anemometry was done behind geometrically similar perforated plates in a wind tunnel to establish spatially resolved turbulence decay functions in steady flow. Limited in-cell measurements were then taken to prove the similarity between temporal decay at a fixed point after passage of the moving plate, and the spatial decay in flow downstream of a fixed plate. The results of both cell and wind tunnel anemometry will be presented in Chapter 4.

All anemometry was performed using a TSI-1051 constant temperature hotwire system with a 1.5 mm long, 5 μm dia. platinum coated tungsten wire sensor. Frequency response of the system was determined to be about 15 kHz by internally generating a 1 kHz square wave according to the technique discribed by Fremuth [34]. The unlinearized output of the hotwire bridge was calibrated directly to velocity using a nozzle calibrator standard. A fourth order least squares

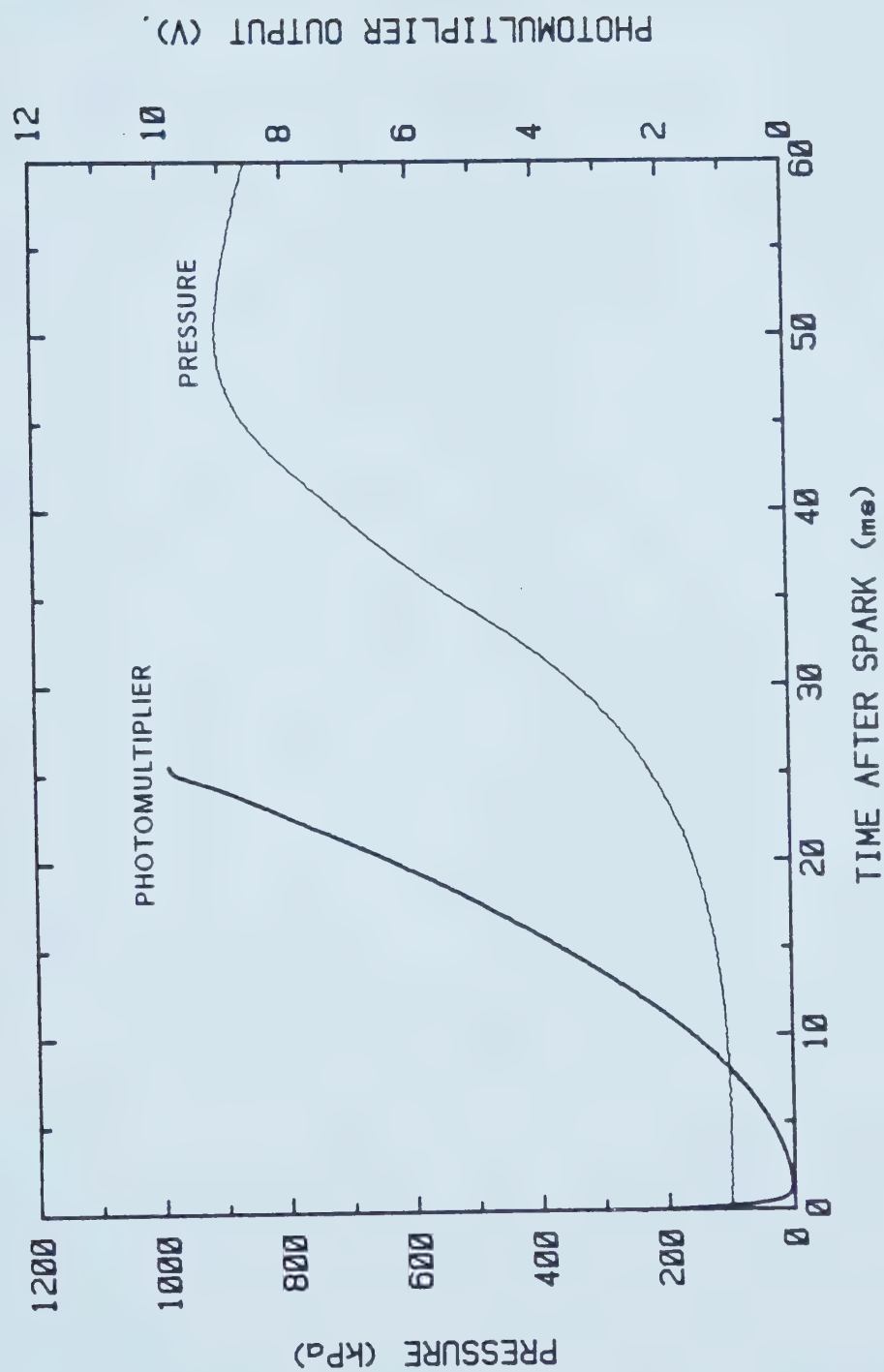


FIGURE 3.14 Typical Explosion Record of Stoichiometric Propane-Air (Non-Turbulent)

polynomial is fitted to the calibration data. A sample hotwire calibration is included in Figure 3.15

3.3.1 ANEMOMETRY IN THE COMBUSTION CELL

The equipment used for in-cell anemometry is shown schematically in Figure 3.16. The hotwire probe holder was fixed in the access normally occupied by the micrometer spark electrode and the wire was positioned horizontally at the exact centre of the combustion chamber. The probe fits through the centre hole of the passing perforated plate.

The output of the hotwire bridge is recorded on one channel of the FM tape recorder while other channels recorded the same signals as in regular combustion experiments. A higher gain of 30 kPa/volt on the pressure transducer was set in hope of sensing drag on the plate as it swept past the pressure sensor, but no such pressure variation was detected.

The signals were taped at 30 i.p.s and replayed at 3.75 i.p.s. to the A/D sampling at 20kHz, giving an effective overall sampling rate of 40 kHz per recorded channel. As in combustion runs, digitization started at the second tooth pulse. A total of 0.768 s of data were saved for each run.

Raw data were converted to integer velocities in mm/s and corrected for any differences in ambient temperature and pressure from calibration conditions. A specially prepared binary data disk was used to store velocity data and

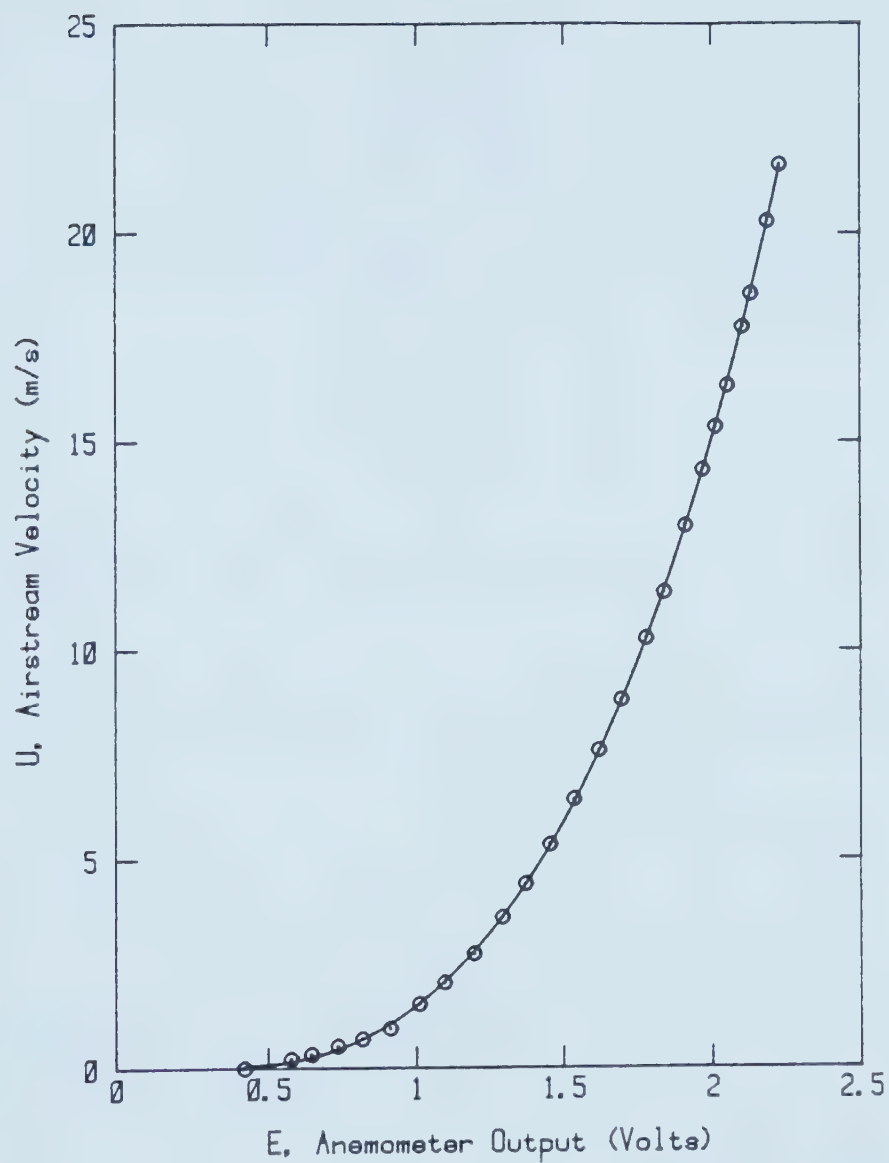


FIGURE 3.15

Sample Calibration Curve for Hot Wire
Anemometer System

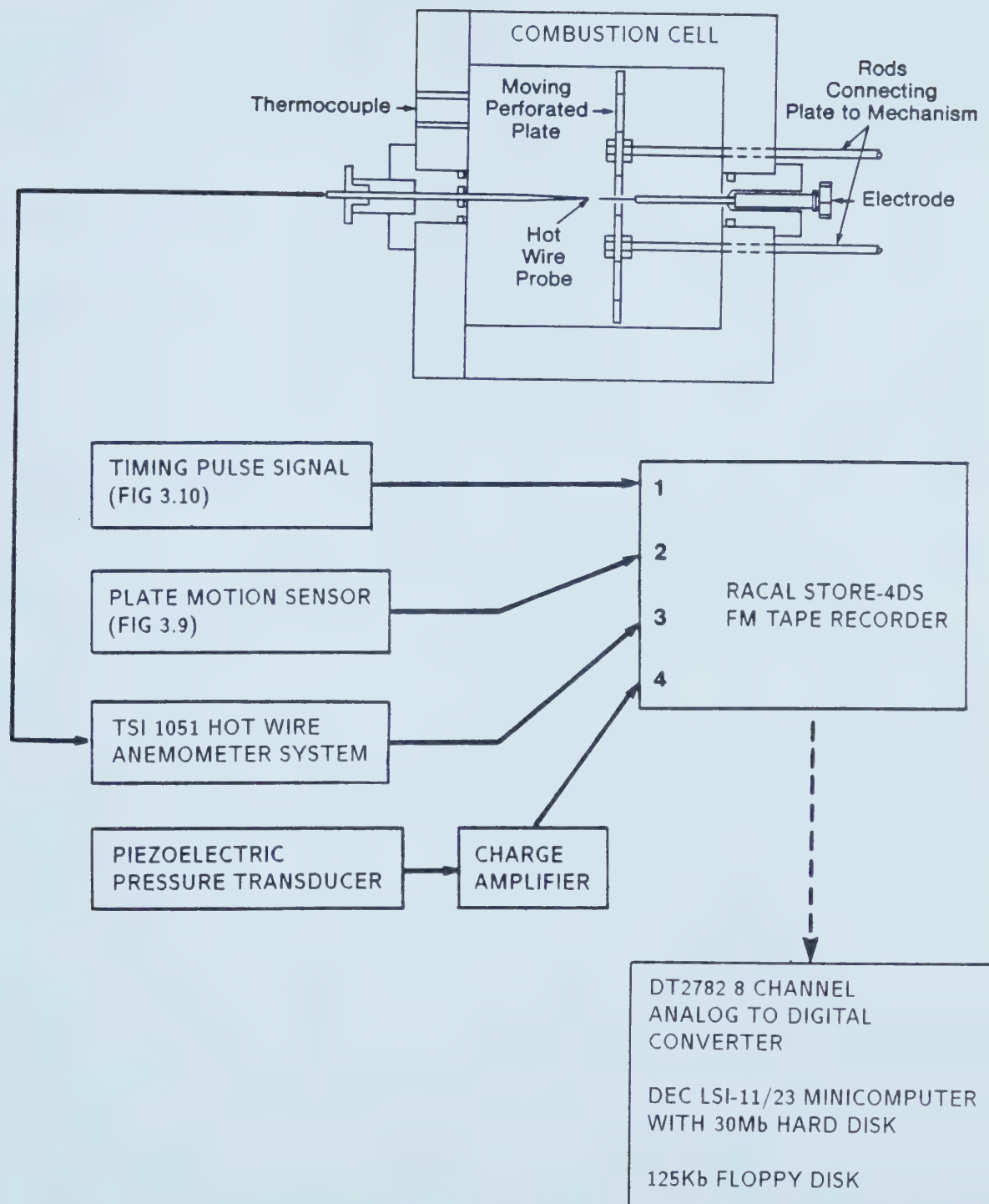


FIGURE 3.16 Apparatus and Signal Recording Summary for Turbulence Measurement in the Combustion Cell

accompanying run information.

A total of 12 identical runs with the 20 mm plate were recorded, and an ensemble mean signal assembled which will be compared with wind tunnel measurements in Chapter 4.

3.3.2 ANEMOMETRY IN THE WIND TUNNEL

Figure 3.17 shows the apparatus used for hotwire anemometry downstream of perforated plates in a 30 cm square wind tunnel. The 5mm thick, 30 cm plates were perforated with 2.5, 5, 10, and 20 mm dia. holes to have geometry and blockage ratios identical to their combustion cell counterparts. When installed, the center hole of each plate was carefully aligned with the wind tunnel centreline.

The hotwire probe was held in a vernier carrier for accurate axial, lateral, and vertical placement. The position of the wire was always measured relative to the centreline at the upstream face of the perforated plate. A Valedyne model DP45 pressure transducer and CD15 conditioning unit (1.0 in. of H_2O range) on the pitot tube 1 m downstream of the plate was used in setting mean wind tunnel velocity, and for checking consistency of hotwire output during measurements. For the bulk of wind tunnel tests, the mean centreline speed was set at about 5 m/s.

Direct analog measurements of hotwire bridge output were made with mean and RMS voltmeters for preliminary axial, lateral, and vertical traverses behind the 20 mm plate. These data were used to determine the degree of homogeneity

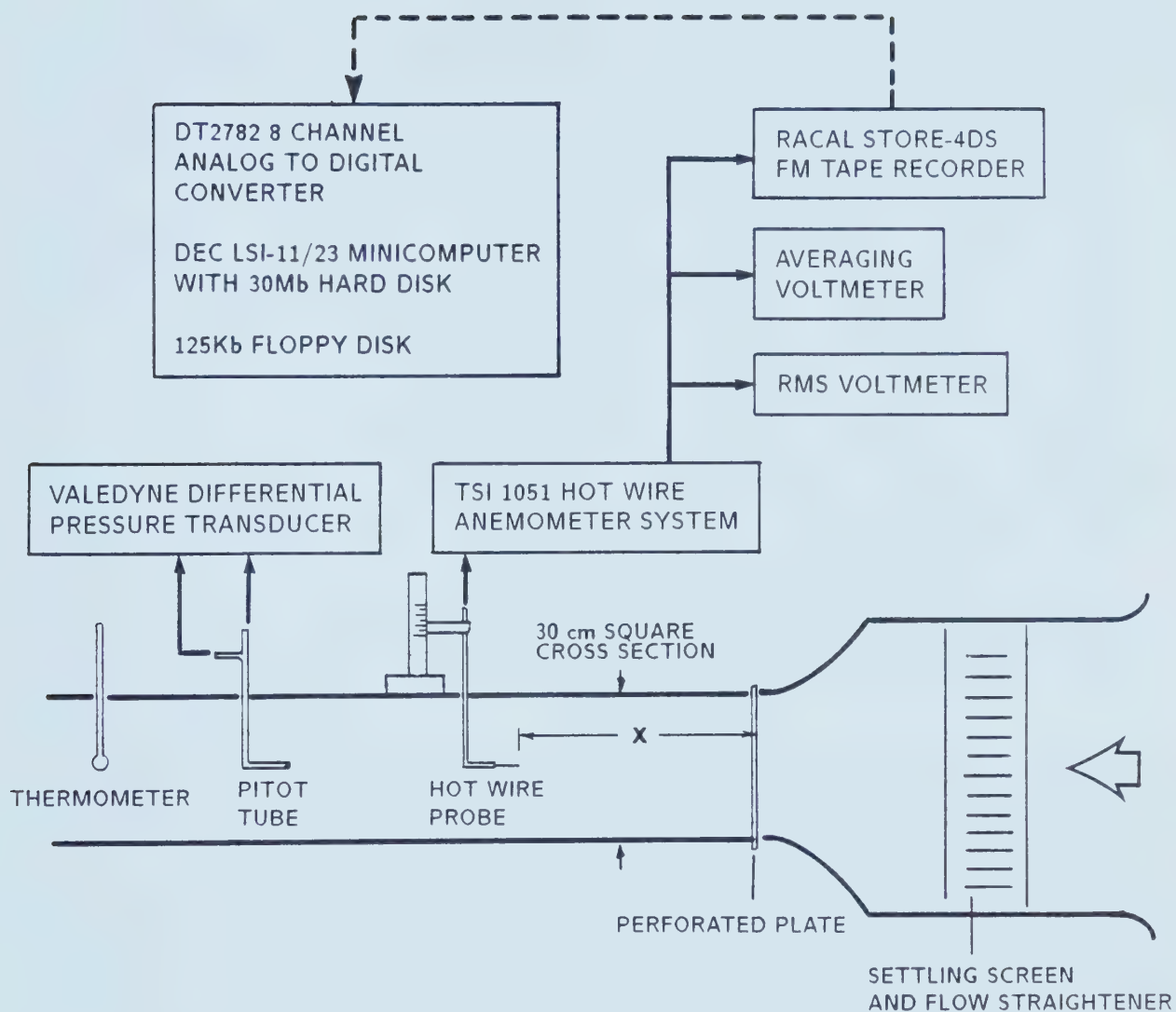


FIGURE 3.17

Apparatus and Signal Recording Summary for
Turbulence Measurement in the Wind Tunnel

of the turbulence depending on downstream position.

For more refined turbulence analysis, signals were taped on the FM recorder during detailed axial traverses along the wind tunnel centreline behind each of the four perforated plates. Hotwire bridge output at each probe station was recorded at 15 i.p.s. tape speed (allowing a 0 to 10 kHz bandwidth) and replayed at the same speed to port 0 of the A/D. A sampling frequency of 20 kHz was sufficiently fast, since Fast Fourier Analysis on bridge output indicated corner frequencies were less than 1 kHz, and the -20 dB cutoff was generally less than about 8 kHz. For each probe station, 12.8 s of data were digitized, calibrated to mm/s, and stored in binary integer form on floppy disk for later digital processing.

Computer software was used to generate frequency spectra and autocorrelation data for the hotwire velocity records. Mean and RMS values were calculated from the digital data and were confirmed by the analog measurements recorded for all probe stations.

1. RESULTS OF TURBULENCE MEASUREMENTS

This chapter presents the results of the hotwire anemometry experiments carried out with the apparatus detailed in Chapter 3. The intent of these measurements was to establish functional predictions of the turbulence intensity and scale to be used as independent variables in turbulent combustion experiments.

The detailed measurements in the present study were performed to enlarge on results of similar observations by Checkel [3] which were reported in further detail by Checkel [26]. These earlier studies were more concerned with the region of intense turbulence soon after the passage of the perforated plate across the combustion chamber. The present study will concentrate on a slightly later period following plate passage, where large scale coherent motions have entirely broken down and the turbulence is homogeneous. These regimes of turbulence will be discussed in detail later on.

4.1 GENERAL DISCUSSION

Conventional hotwire anemometry was chosen over more elaborate laser based diagnostics chiefly because of availability and the relative ease in analyzing the wide range of conditions considered. There are inherent limitations however in the use of a hotwire to directly measure the time varying turbulence in the combustion cell.

A hotwire sensor, oriented with its axis along the z coordinate, responds in general to the modulus of velocity in the x-y plane:

$$\text{signal} = \sqrt{(\bar{U}_x + u'_x)^2 + (\bar{U}_y + u'_y)^2} \quad \text{..... 4.1}$$

where \bar{U}_x ; \bar{U}_y are the mean x and y velocities,
and u'_x ; u'_y are the instantaneous fluctuation velocities

In the turbulent combustion cell, coherent structures (jets which immediately follow the passage of the plate) must vanish rapidly and the remaining turbulent fluctuations are no longer superimposed on a mean flow. In this case the hotwire probe senses only the modulus of the fluctuation velocities in the x-y plane.

$$\text{signal} = \sqrt{u'^2_x + u'^2_y} = u_{xy} \quad \text{..... 4.2}$$

Without a second perpendicular wire, the fluctuations are not resolvable into their directional components.

Uncertainty is increased further for low net velocities because the sensitivity of the hotwire probe decreases with lower net velocities, and there is also the possibility of false indications caused by the wire's heated wake recrossing the sensing point.

Another difficulty with in-cell anemometry arises because the turbulence generated in the combustion cell decays rapidly relative to the time scale of velocity fluctuations. A very large ensemble of identical turbulence decay cycles would be required to statistically generate correlation or spectrum data from which turbulence scales

could be deduced.

All of the above difficulties are circumvented by measuring directly analogous spatially decaying turbulence in the wake of the perforated plate fixed in a constant velocity wind tunnel. The resulting turbulence decay should be similar in both cases since, as is generally acknowledged, the dissipation of turbulent energy takes place in the small scales and is independent of the mean flow on which it is superimposed (assuming homogeneous turbulence). This contention is later supported by comparing a limited ensemble of in-cell turbulence decay cycles to the detailed decay results in the wind tunnel.

In the wind tunnel, where the turbulence is carried along an axial (x-direction) mean flow with no mean flow in the y-z plane, and when the turbulence fluctuation velocities are significantly smaller than the mean velocity (less than 10%), the hotwire response of equation 4.1 may be reduced to:

$$\text{signal} = \bar{U}_x + u'_x \quad \dots\dots\dots 4.3$$

From this signal is simply calculated the streamwise mean velocity \bar{U}_x , and the RMS fluctuation velocity $u_x = \sqrt{u_x'^2}$. For every probe location a power ($u_x'^2$) spectrum and an autocorrelation of the fluctuation may be generated and the streamwise scales deduced.

The wind tunnel results are then used to predict the turbulence intensity and scale in the combustion cell based on the direct analogy between the bulk wind tunnel speed,

$$V = \text{Flowrate} / \text{cross sectional area} \quad \dots\dots 4.4$$

and the mean plate speed V in the cell. The time after the plate passes the centre of the cell (where the probe was located for in-cell measurements) is then simply related to the axial position in the wind tunnel behind the plate by:

$$x = Vt \quad \dots\dots\dots 4.5$$

All length parameters will be normalized with the plate hole diameter D , and velocities will be normalized with the equivalent plate speed V .

4.2 TURBULENCE BEHIND PERFORATED PLATES IN THE WIND TUNNEL

The structure of air flow in the wake of the perforated plates in the wind tunnel is seen from horizontal cross-stream hotwire traverses at various positions downstream of the plate. Figure 4.1 shows the variation in streamwise mean and RMS fluctuation velocity at several positions downstream of the 20 mm D perforated plate with a bulk wind tunnel speed of 5 m/s.

At one diameter downstream, the flow consists of high speed jets with an almost uniform velocity profile and low turbulent fluctuation. These jets are essentially steady, as testified by the vanishing fluctuation velocity along the jet centreline. The fluctuation velocity is highest at the jet's edge, as would be the expected result from vortex shedding at the edge of the hole in the perforated plate, and the high shear between the jet and recirculating flows.

Roughly the same conditions persist at 2.25 diameters

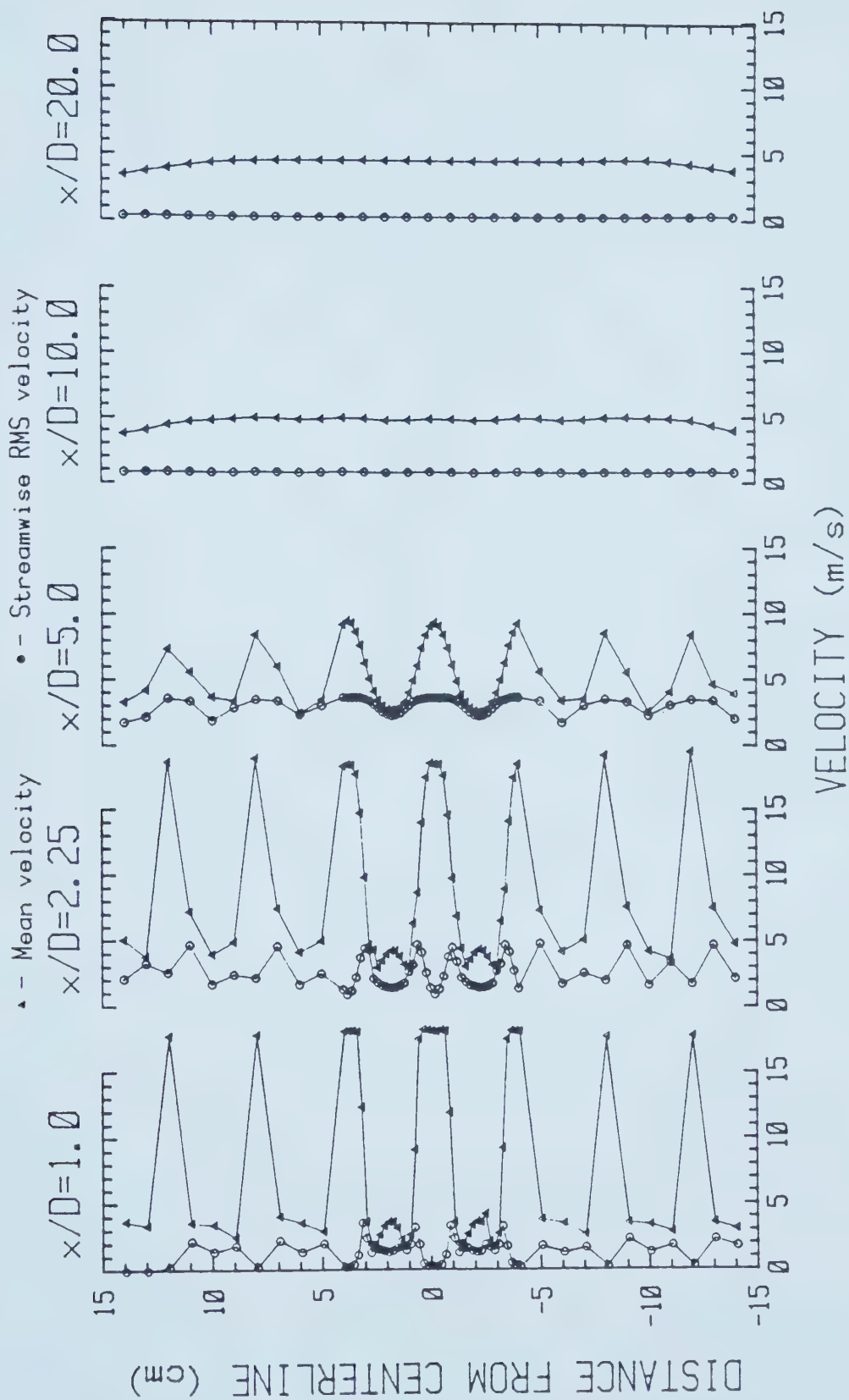


FIGURE 4.1 Horizontal Velocity Profiles Downstream of the 20mm Perforated Plate

with the jet velocity profile becoming parabolic, but with no apparent decrease in peak velocity.

By five diameters downstream, the maximum fluctuation velocity now lies on the jet centreline, and the mean centreline velocity has fallen to about 60% of its original value. These changes result not only from the obvious breakdown of the jet, but also from the onset of intermittancy of the jet flow - that is the wandering of the jet about its original centreline. This tends to reduce the time averaged peak velocity and increase the apparent RMS fluctuation velocity at the fixed sensor location.

The traverses at 10 and 20 diameters show the jets have totally coalesced to a homogeneous flow, since both mean and RMS fluctuation velocities are uniform across the wind tunnel. The growth of a boundary layer in the wind tunnel is apparent from the mean velocity profile.

4.2.1 DECAY OF MEAN VELOCITY

The results of axial (streamwise) traverses along the wind tunnel centreline are shown for all four perforated plates in Figures 4.2 and 4.3. Recall that the central hole of each perforated plate was aligned with its centre on the centreline axis of the wind tunnel.

It is clear from Figure 4.2 that the mean velocity has decayed to the bulk wind tunnel speed by ten diameters, corresponding to the transition to homogeneity that was apparent in Figure 4.1. For each of these traverses, the

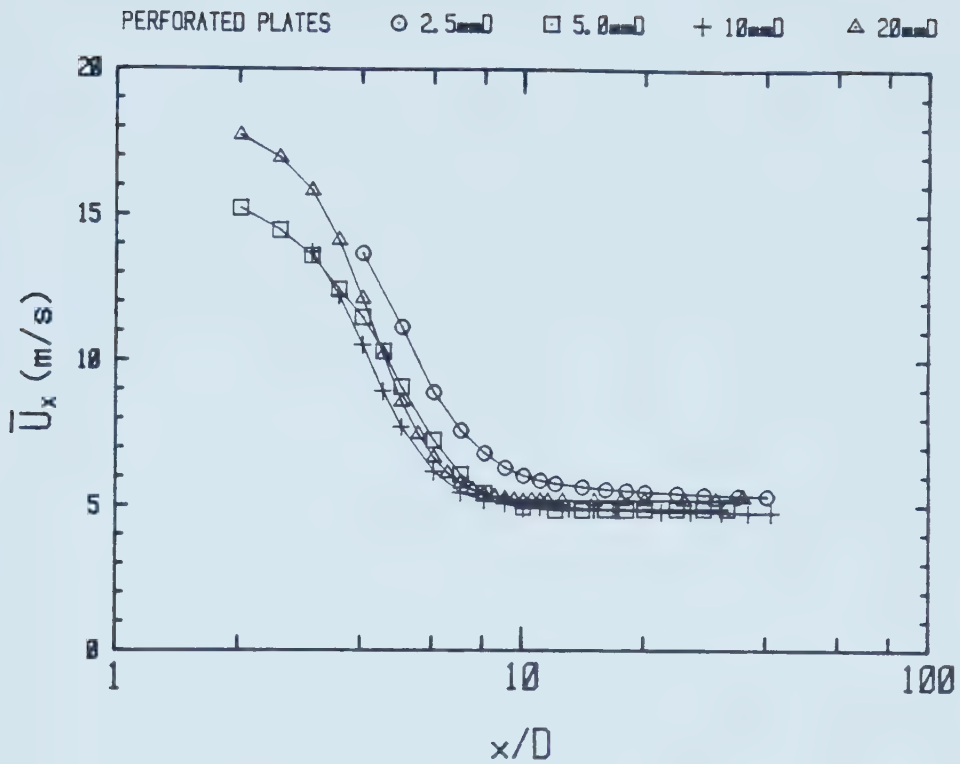


FIGURE 4.2

Decay of Mean Velocity on the Centreline
Downstream of the Perforated Plates

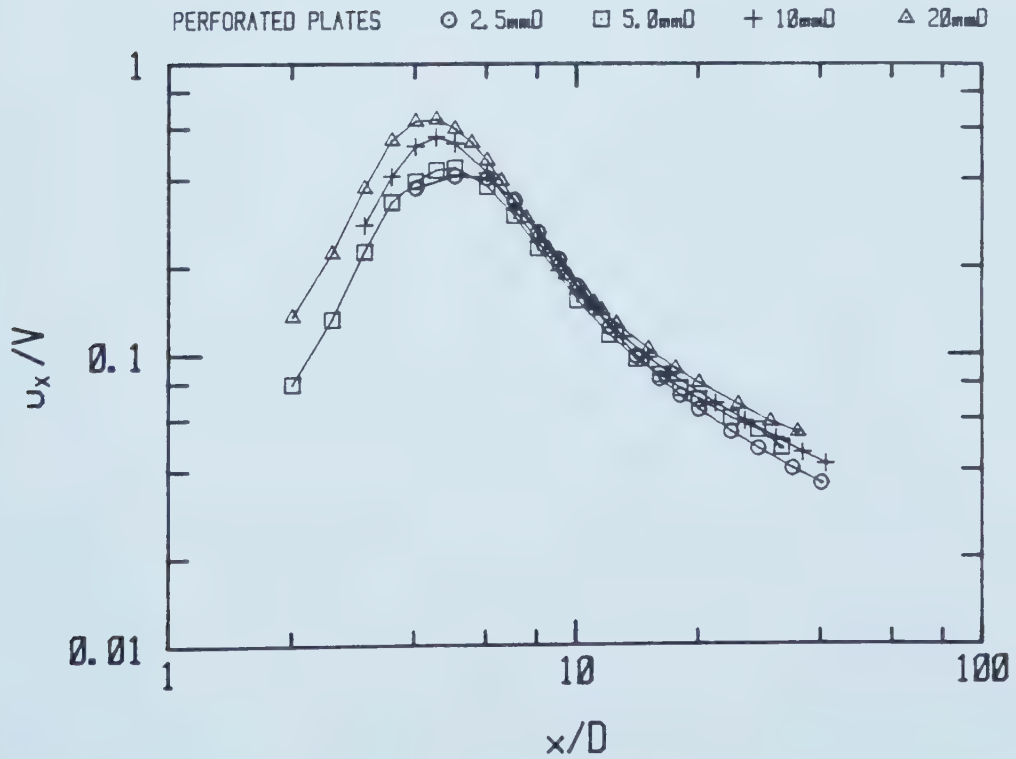


FIGURE 4.3

Decay of RMS Fluctuation Velocity on the
Centreline Downstream of the Perforated
Plates

bulk wind tunnel speed was set at about 5 m/s, but Figure 4.2 shows slightly higher mean velocity for the 2.5 mm D plate, most pronounced between five and ten diameters. Since mean velocity behind this plate converges to the common bulk speed further downstream, neither the wind tunnel setting nor the hotwire calibration were likely in error. This higher indicated mean velocity could result from the range of spatial intermittancy for these smallest jets being close to the length of the hotwire probe, such that the jet centreline is more continuously incident upon the wire. One might then expect a corresponding decrease in the apparent RMS fluctuation, but Figure 4.3 reveals no such decrease. To further examine this behavior, detailed cross stream traverses behind the 2.5 mm D plate are necessary, but none were performed for the present study. Measurements by Checkel [26] behind the 2.5 mm D perforated plate began at ten diameters downstream, so this peculiarity would not have been observed. While this matter is interesting, it should have little impact on the comparison between turbulence levels in the wind tunnel and the combustion cell, and so will remain unresolved for the present.

Beyond ten diameters, the difference between the bulk wind tunnel velocity and the measured mean velocity is attributable to boundary layer growth, but the difference between \bar{U}_x and V was not seen to be more than about 5%. For later comparisons with combustion cell data the mean velocity and bulk velocity are assumed identical beyond ten

diameters.

4.2.2 DECAY OF RMS FLUCTUATION VELOCITY

The decay of the streamwise fluctuation velocity behind all four perforated plates is shown in Figure 4.3. The peak turbulence fluctuation at about five diameters marks the zone where the increasingly intermittent jets lose coherence and coalesce with each other and the surrounding flow. With the fluctuation normalized by bulk velocity, the decay of fluctuation velocity appears similar beyond about six diameters for all the plates.

It was demonstrated by Checkel [26] that the normalized decay for a given perforated plate remained independent of bulk velocity over a bulk velocity range of about 4 to 15 m/s. Since a similar range of flows was considered in the present study, the data of Figure 4.3 will then be sufficient to predict the fluctuation velocity in the wake of each plate as a function of plate hole diameter and bulk velocity. For use in later in-cell turbulence predictions, the decay of RMS fluctuation velocity beyond 10 diameters for each of the plates is fitted using least squares with a simple power law:

$$u/V = A(x/D)^n \quad \dots\dots\dots 4.6$$

The results of these fits are presented in Table 4.1, and are also shown graphically in Figure 4.4

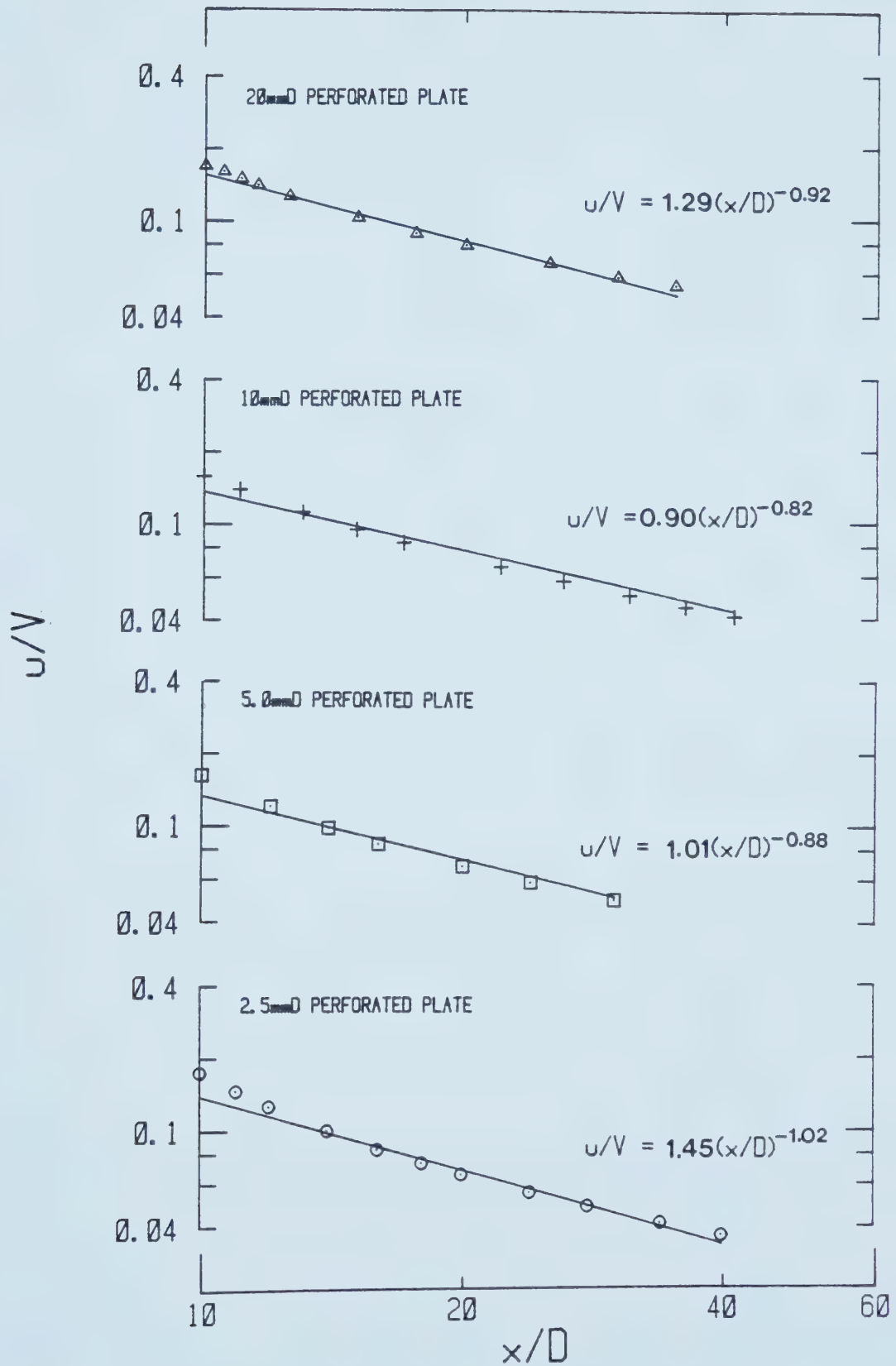


FIGURE 4.4

Power Law Fits to the Decay of RMS
 Fluctuation Velocity Downstream of the
 Perforated Plates

Table 4.1 Decay Constants for Turbulence Beyond 10 Dia.

<u>PLATE</u>	<u>A</u>	<u>n</u>
20mmD	1.29	-0.92
10	0.90	-0.82
5	1.01	-0.88
<u>2.5</u>	<u>1.45</u>	<u>-1.02</u>

In the study by Checkel [26], similar fits were made, but with fewer points and over a larger region which included some of the non-homogeneous flow within ten diameters. Decay exponents reported were $n = -1$ for the 5, 10, and 20 mm D perforated plates, and $n = -.7$ for the 2.5 mm D plate.

Other sources for comparison are found in numerous studies of turbulence behind various grids and screens. Baines and Peterson [31] reported comprehensive measurements behind lattice type screens of varying solidity ratio. Those data are compared with results from the 10 mm perforated plate in Figure 4.5. In order to be consistent with that earlier work, the fluctuation velocity in Figure 4.5 is normalized by local mean velocity \bar{U}_x , and the downstream distance by the bar width b , (lattice geometry is shown in Figure 4.5). The equivalent bar width for a perforated plate was calculated by assuming a lattice of equal wetted perimeter and fraction open area. Thus the equivalent mesh width M , and bar width b , for these perforated plates are:

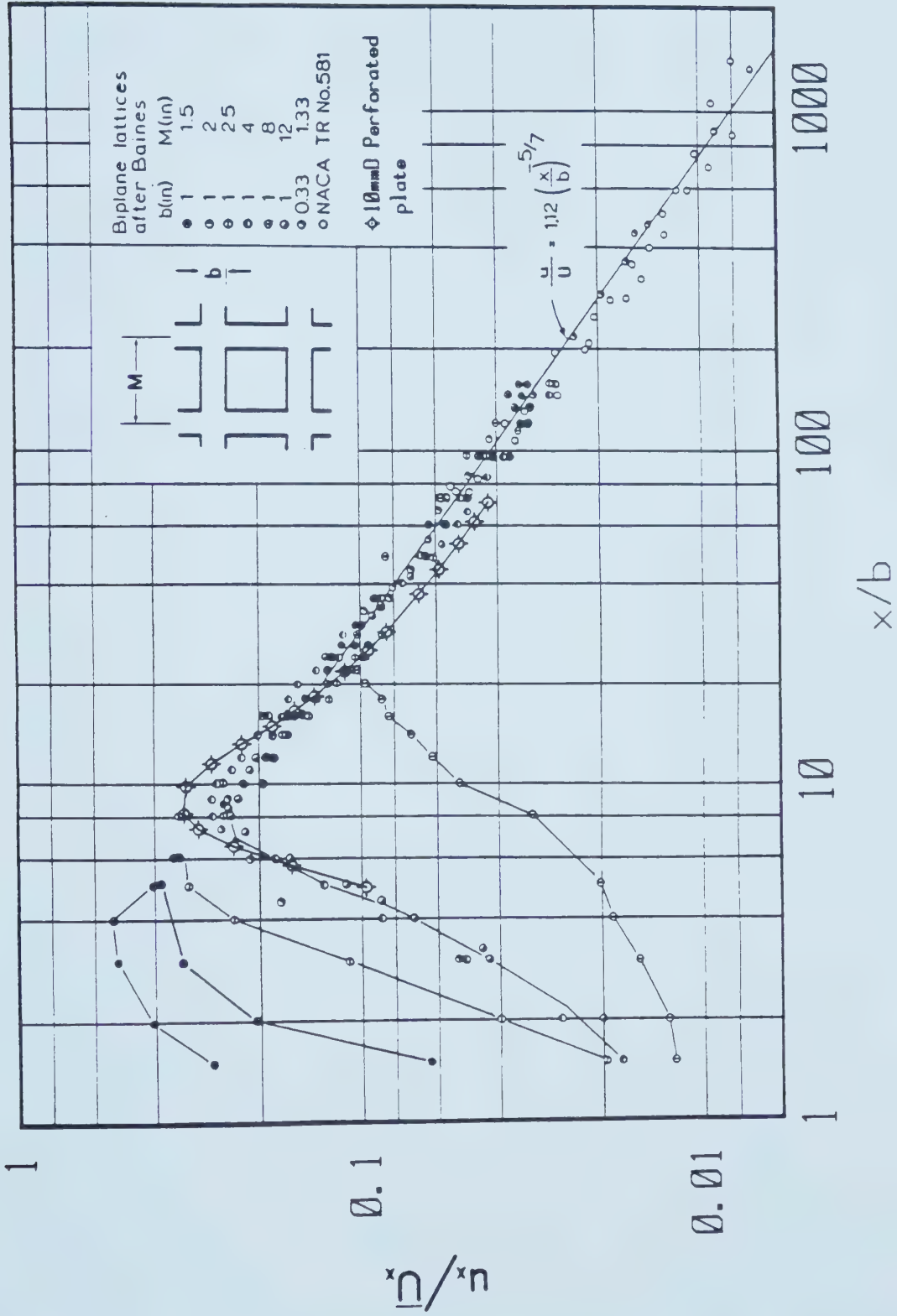


FIGURE 4.5 Comparison Between RMS Decay Behind a Perforated Plate and That Behind Lattice Type Screens

$$M = D\sqrt{8/\pi}$$

$$b = D(\sqrt{8/\pi}-1) \quad \dots\dots\dots 4.7$$

Observe that since local mean velocity was seen to converge to bulk velocity past ten diameters (17 bar-widths) for the perforated plates, the apparent decay exponent will be unaffected by the choice of normalizing velocity beyond this point. The $n = -5/7$ exponent shown in Figure 4.5 was originally predicted by Frenkiel [30] based on the assumption of isotropic turbulence, and was also found by Baines and Peterson [31] to fit some limited measurements of turbulence behind perforated plates of various solidity ratios. Uberoi and Wallace [32] measured turbulence behind a wide variety of grids chiefly to examine the effect of grid geometry on the degree of anisotropy between streamwise and cross stream intensities. Those authors show decay exponents of streamwise RMS fluctuation ranging between $n = -0.6$ and $n = -0.8$.

In general, the decay exponents for the present study are somewhat higher in magnitude than those reported by other grid turbulence investigators. This is more likely the result of the relatively limited, higher intensity region over which the present data was fitted, rather than from characteristic differences between perforated plates and other grids. Examination of the perforated plate turbulence decay in Figure 4.4 shows that the decay rate is not in fact a perfect power law beyond ten diameters, and with increasing distance, the decay exponent decreases in

magnitude. Figure 4.5 shows that the decay rate beyond 40 equivalent bar-widths past the perforated plate appears to approach that of the lattice type screens.

The question of anisotropy between streamwise and cross stream fluctuation components, while not addressed in wind tunnel measurements in the present study, will become important in later interpretation of in-cell anemometry data. [31] and [32] examined this anisotropy in detail and their results will be referred to in the discussion of in-cell anemometry results.

4.2.3 POWER SPECTRA, CORRELATION, AND SCALES

The turbulence spectra and autocorrelation data discussed here were generated from the digitized wind tunnel anemometry data and were used chiefly for the calculation of turbulence scales. These scales were then applied directly in later predictions of in-cell turbulence.

A normalized power spectrum of streamwise fluctuation intensity is shown in Figure 4.6 for the 10 mm D perforated plate at ten diameters. This spectrum does not show a definite inertial subrange with the $-5/3$ exponent suggested by Kolmagorov's universal equilibrium hypothesis. This is likely because the turbulence Reynolds number is not sufficiently high to allow separation between the wavenumber range of energy containing eddies and the range of maximum energy dissipation, as required by Kolmagorov's formulation.

Figure 4.7 shows power spectra at various points

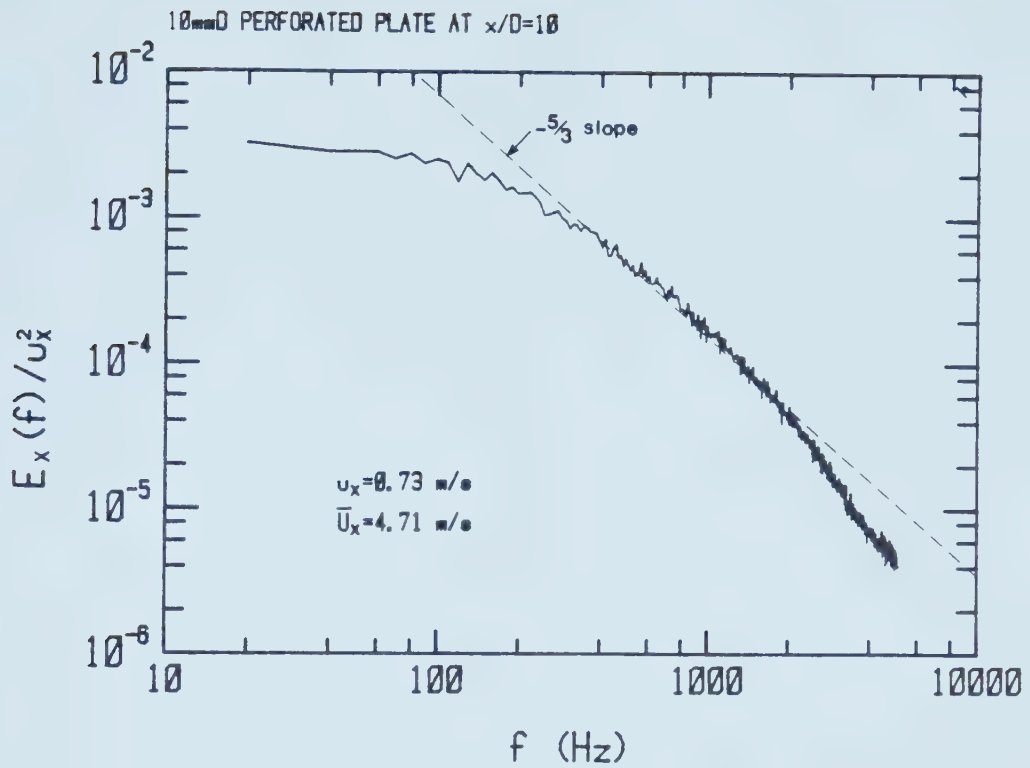


FIGURE 4.6 The Normalized Power Spectrum at 10 Dia. Downstream of the 10mmD Perforated Plate

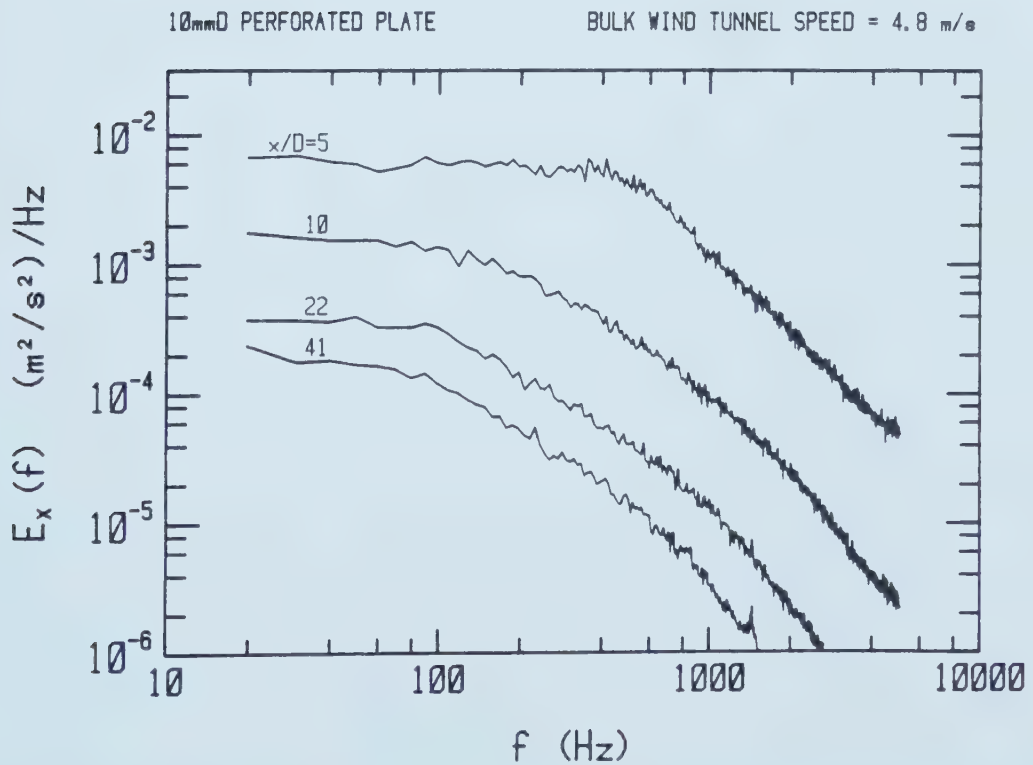


FIGURE 4.7 Power Spectra at Various Positions Downstream of the 10mmD Perforated Plate

downstream of the 10 mm D plate. The data in this plot are not normalized in order to illustrate the absolute decay of turbulence energy throughout the spectrum. What might appear to be an inertial subrange in the spectrum at five diameters resulting from the peak at about 400 Hz in fact has an exponent of -2.05 and should not be interpreted as such. Of much greater interest is the similarity in shape between the spectra beyond ten diameters. While the magnitude of turbulent energy decreases, the spectral distribution remains relatively invariant. It is only at the highest frequencies where the progressive extinction of the smallest eddies is evident. This form of spectral attenuation can be reasonably represented by the change in the mean activity scale - i.e. the integral scale of turbulence. Thus for the decay region of interest in this study, the total turbulence energy is represented by the fluctuation velocity, and the energy spectrum is reflected in the integral scale.

The integral time scale was calculated from the Eulerian time correlation (autocorrelation) for the single probe. A single autocorrelation is shown for the 10 mm plate at ten diameters in Figure 4.8. The shape of this curve typifies observed data beyond 10 diameters for all the plates. The integral time scale is by definition integrated from the autocorrelation function:

$$\tau_E = \int_0^{\infty} R_E(t) dt \quad \dots\dots\dots 4.8$$

Evaluation of this integral from digital data was however found to result in inconsistent and non-converging values,

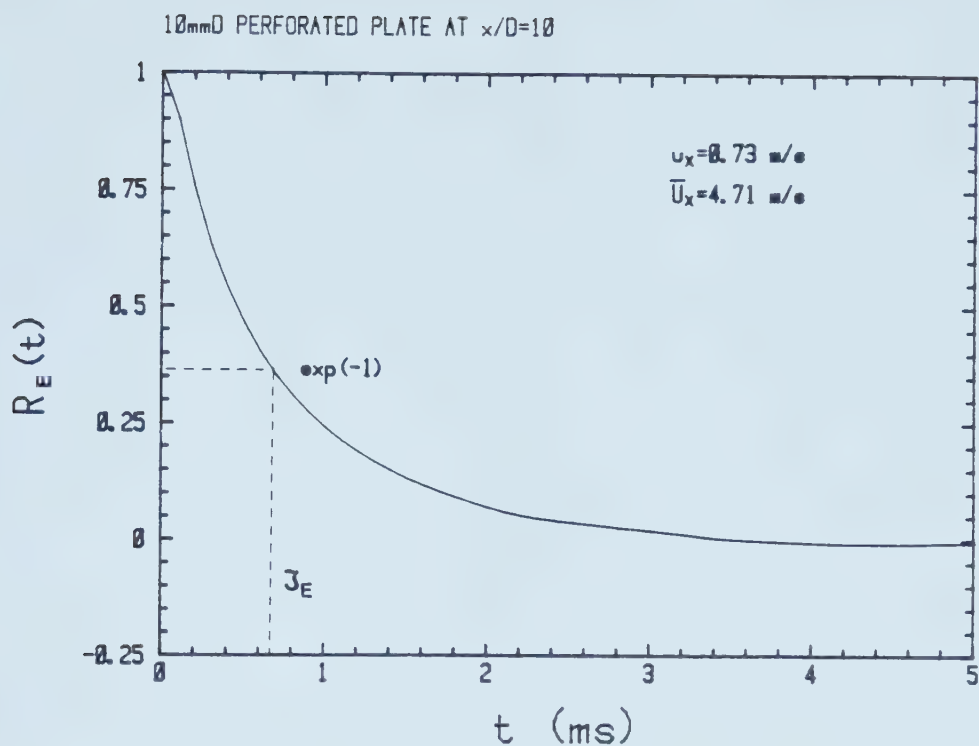


FIGURE 4.8

The Autocorrelation Function at 10 Dia.
 Downstream of the 10mmD Perforated Plate

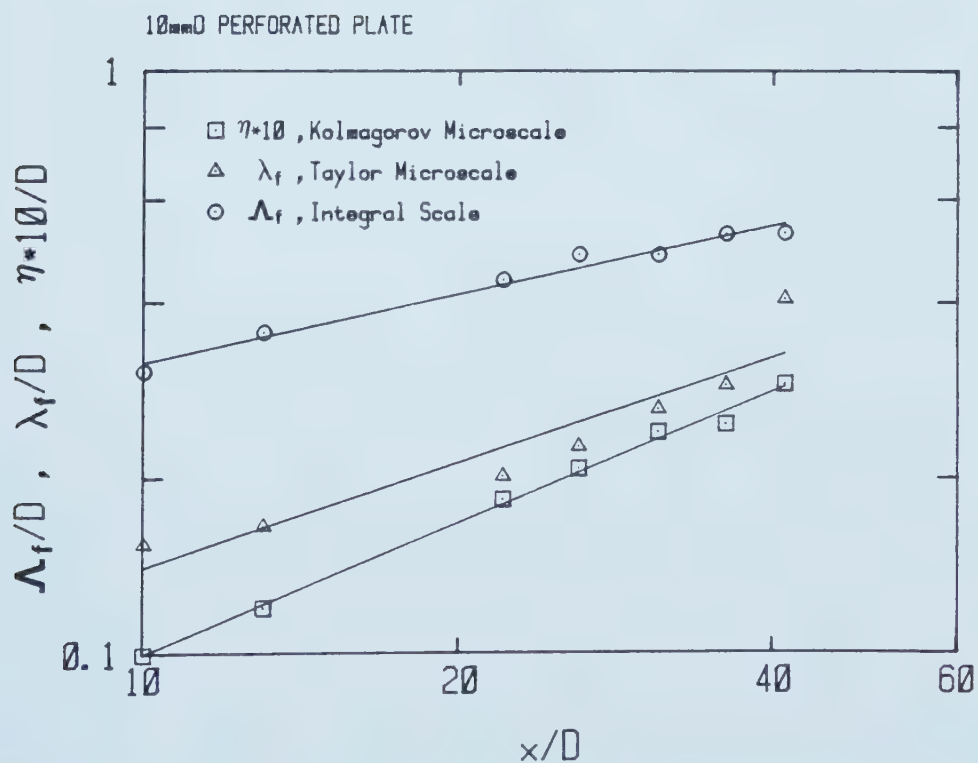


FIGURE 4.9

The Growth of Turbulence Scales Downstream
 of the 10mmD Perforated Plate

since the natural oscillation of the correlation about zero is often of the same order of magnitude as the digital resolution. A more consistent and reliable method of calculating the integral scale is achieved with the simple and commonly used assumption that the turbulence has no inertia and so behaves as a first order Markov process where du'/dt at time $t+\Delta t$ is independent of du'/dt at t . This results in the simple empirical formulation suggested by Hinze [27] (pp 58,59) where the autocorrelation has an exponential form:

$$R_E(t) = \exp(-t/\tau_E) \quad \dots\dots\dots 4.9$$

It is clear that the integral time scale is now easily estimated from the data where $R_E(t=\tau_E) = \exp(-1)$. For the data of Figure 4.8, the time scale was estimated as 0.67ms, as indicated on the plot. The streamwise integral length scale is then simply the product of this time scale and the local mean velocity.

$$\Lambda_f = \bar{U}\tau_E \quad \dots\dots\dots 4.10$$

Although turbulent combustion results discussed later are not related to turbulence microscales, estimation of the Taylor microscale and the Kolmagorov dissipation scale are presented in this discussion for completeness.

The Taylor microscale was calculated using the method suggested by Taylor (see Hinze [27], p 64,65) whereby the micro-time scale is related to the streamwise power spectrum $E(n)$ by:

$$1/\tau_E^1 = 2\pi^1/u_X^1 \int_0^\infty n^1 E(n) dn \dots\dots\dots 4.11$$

Again the corresponding streamwise length scale is simply the product of this time scale and the local mean velocity.

The Kolmagorov microscale is defined in terms of the viscosity and the local dissipation ϵ .

$$\eta = 4\sqrt{v^3/\epsilon} \dots\dots\dots 4.12$$

The local dissipation in this work was estimated based on the large eddy scale l , and the assumption of locally isotropic turbulence which lead to the approximation:

$$\epsilon \approx B_0 u_X/l \dots\dots\dots 4.13$$

Hinze [27] (p 225,255) shows that $B_0 \approx 0.8$. The large eddy scale in equation 4.13 is commonly related to the integral scale by

$$l \approx B_1 \Lambda_f/2 \dots\dots\dots 4.14$$

where Hinze [27] (p 248) gives $B_1 \approx 2.66$. Combining equations 4.13 and 4.14 gives the dissipation estimate:

$$\epsilon \approx 0.6 u_X/\Lambda_f \dots\dots\dots 4.15$$

which, substituted into 4.12 gives the estimate used in this work for calculating the Kolmagorov microscale.

$$\eta \approx 4\sqrt{v^3/(0.6 u_X/\Lambda_f)} \dots\dots\dots 4.16$$

The dissipation may also be calculated from the rate of decay of turbulent kinetic energy, q^2 indicated by the fluctuation velocity measurements:

$$\begin{aligned} \epsilon &= -dq^2/dt \\ &= -d(3u_X^2)/dt \dots\dots\dots 4.17 \end{aligned}$$

assuming isotropic turbulence, where the time derivative of 4.17 is simply taken from the fitted spatial decay functions

of Figure 4.4 via

$$du_x/dt = Vdu_x/dx \dots\dots\dots 4.18$$

Comparison of the two estimates shows that method of Equation 4.15 yields dissipation values of roughly half those indicated by the method of Equation 4.17. If isotropy typical of grid turbulence is applied in 4.17 - for example $q^2 = 2.4u_x^2$ from [32] - then the two agree even more closely. This is reasonable agreement considering that such grid turbulence is generally not isotropic as assumed, and more importantly that the implicit assumption of vanishing turbulence production may not be appropriate. Turbulence producing shear layers may still exist in the regime beyond 10 diameters, including those which result from vortex shedding at the plate.

The growth of all three turbulence scales beyond 10 diameters behind the 10 mm D perforated plate is shown in Figure 4.9. Power functions of the form:

$$\text{scale}/D = B(x/D)^m \dots\dots\dots 4.19$$

were fitted to scale data beyond ten diameters for each of the plates. The results of these least squares fits are presented in Tables 4.2 through 4.4. The results of the all integral scale fits are shown graphically in Figure 4.10.

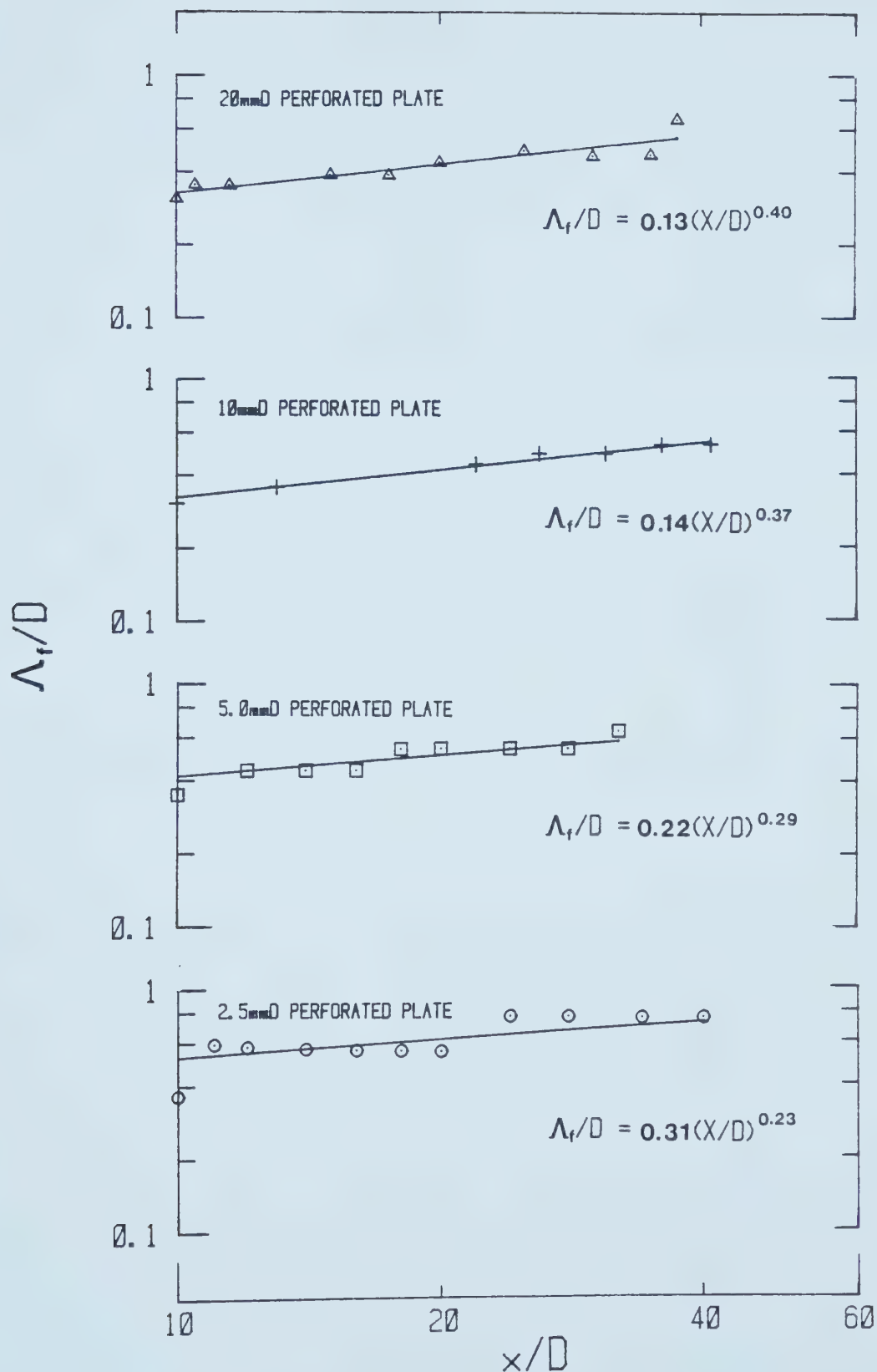


FIGURE 4.10

Power Law Fits to the Growth of Integral Scales Downstream of the Perforated Plates

Table 4.2 Constants for Growth of Integral Scale

<u>PLATE</u>	<u>B</u>	<u>m</u>
20 mm D	0.131	0.397
10	0.140	0.365
5	0.216	0.286
<u>2.5</u>	<u>0.308</u>	<u>0.231</u>

Table 4.3 Constants for Growth of Taylor Microscale

<u>PLATE</u>	<u>B</u>	<u>m</u>
20 mm D	0.034	0.465
10	0.036	0.599
5	0.059	0.616
<u>2.5</u>	<u>0.266</u>	<u>0.245</u>

Table 4.4 Constants for Growth of Kolmagorov Microscale

<u>PLATE</u>	<u>B</u>	<u>m</u>
20 mm D	0.001	0.786
10	0.002	0.790
5	0.002	0.825
<u>2.5</u>	<u>0.003</u>	<u>0.958</u>

4.3 TURBULENCE IN THE COMBUSTION CELL

This section presents the results of the limited hotwire anemometry performed in the Turbulent Combustion Cell to confirm the similarity between perforated plate turbulence in the cell and that observed in the wind tunnel. Measurements were made with only the 20 mm D plate and at one plate speed only, owing to the risk of destruction of the delicate hotwire probes by vibration induced by the plate movement apparatus.

A typical anemometer record beginning at the start of plate motion is shown for a single run in Figure 4.11. It is evident that there are stages of jet formation and decomposition like those noted earlier in the discussion of wind tunnel results. The gas ahead of the plate remains motionless until the plate is within about 15 mm of the probe (located at the centre of the cell). As the plate passes over the probe, the gas in the region of the probe is forced through the central hole of the plate to form the jet. This jet reaches a peak velocity of about twice the nominal plate speed at 3 ms (0.6 diameters of plate travel) following the passage of the plate. Relative to the moving plate, the jet speed of about three times the plate speed agrees reasonably with the wind tunnel results of Figure 4.2. Slightly lower peak jet speed in the cell would be the expected result of the lower pressure differential across the plate due to the 1 mm clearance around the sides of the plate, as well as to the limited total travel of the plate.

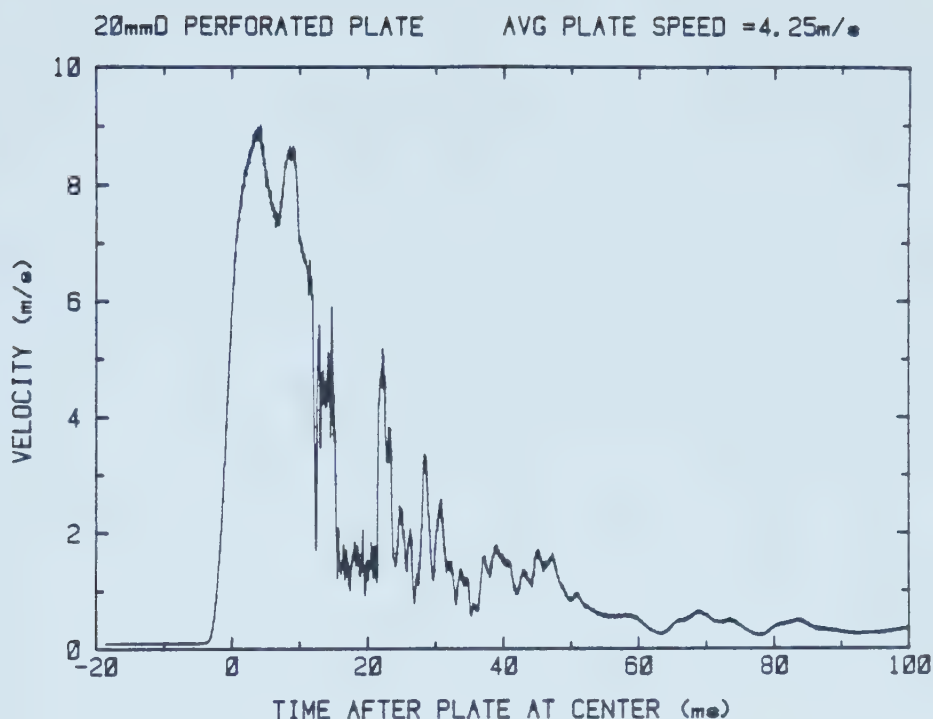


FIGURE 4.11 Anemometer Signal in the Combustion Cell
Following the Passage of the 20mmD
Perforated Plate

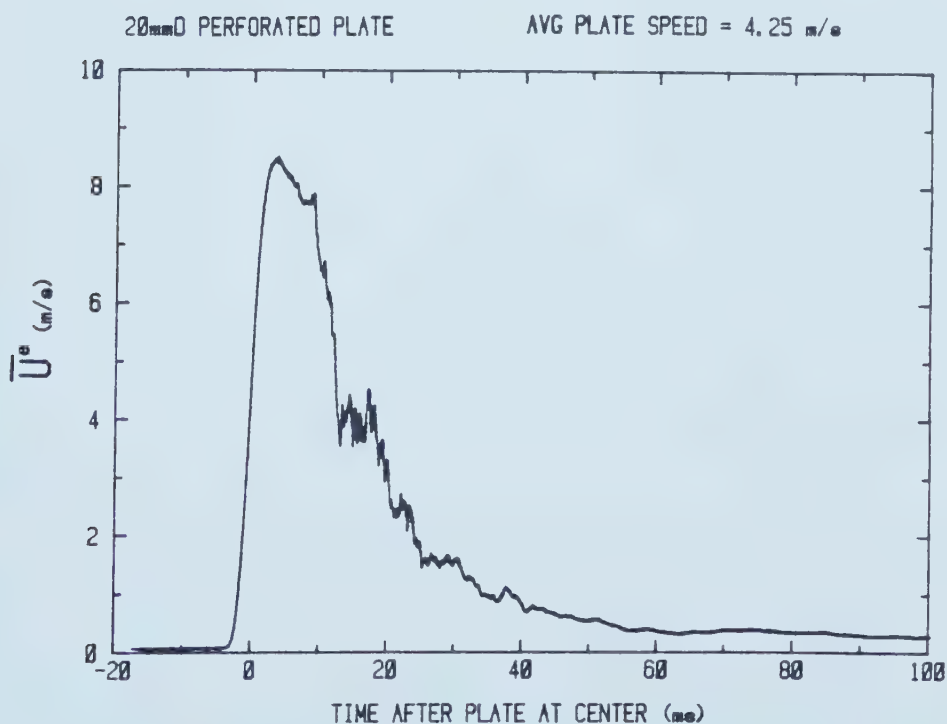


FIGURE 4.12 The Ensemble Mean Velocity at the Centre of
the Combustion Cell for 12 Identical Passes
of the 20mmD Perforated Plate

By 13 ms the plate has reached the end of its travel and jet production ceases. By this time the flow at the probe has begun to rapidly break down and becomes increasingly intermittent. By 25 ms any remaining jet flow at the probe has vanished and the probe will be responding to the modulus of turbulence fluctuation in the x-y plane (probe wire aligned along the z-axis). Negligible mean flow with possible flow reversal is expected. A time of 47 ms corresponds to the downstream position of 10 diameters referred to in wind tunnel correlations.

As outlined in the first section of this chapter, the interpretation of the hotwire response in such a rapidly varying flowfield as exists in the combustion cell poses some difficulties. Acrivlellis [35,36] discusses in some detail the analysis of probe response in situations of low and possibly reversing mean flows. The case of negligible mean flow has been examined by Checkel [26] who showed that the longitudinal RMS fluctuation velocity u_x could be deduced from the mean of the modulus of velocity u_{xy} sensed by the hotwire probe (Equation 4.2). That analysis was based on three assumptions:

1. component velocities in the x-y plane
 behave as uncorrelated random variables
 with normal probability distributions;
2. the component fluctuation velocities
 have zero mean;
3. the relationship between the variances

of the component RMS velocities is known.

(eg. $u_x = u_y$ for isotropic turbulence)

Based on these assumptions it was shown that for the case of isotropic turbulence, the longitudinal RMS fluctuation velocity could be determined from the ensemble mean anemometer signal \bar{U}^e , which for this case of vanishing mean flow is

$$\bar{U}^e = u_{xy} \dots\dots\dots 4.20$$

Checkel [26] calculated for the isotropic case that

$$u_x = 0.798u_{xy} \dots\dots\dots 4.21$$

The case of non-isotropic turbulence was also considered by Checkel since other grid turbulence investigators such as [31] and [32] have reported a range of anisotropy of roughly:

$$0.7 < u_x^2/u_y^2 < 0.9 \dots\dots\dots 4.22$$

for a wide range of grid geometries. For the case of

$u_x^2/u_y^2 = 0.8$, Checkel gives

$$u_x = 0.841u_{xy} \dots\dots\dots 4.23$$

The ensemble mean anemometer signal generated from 12 identical runs in the combustion cell is shown in Figure 4.12. In comparing this plot to Figure 4.11 the effect of the ensemble averaging is seen to smooth out the overall decaying velocity signal. However, in the 15 to 40 ms period following plate passage, it is apparent that this ensemble is not sufficiently large to damp out the large oscillations associated with jet breakdown.

Figure 4.13 compares the decay of streamwise fluctuation

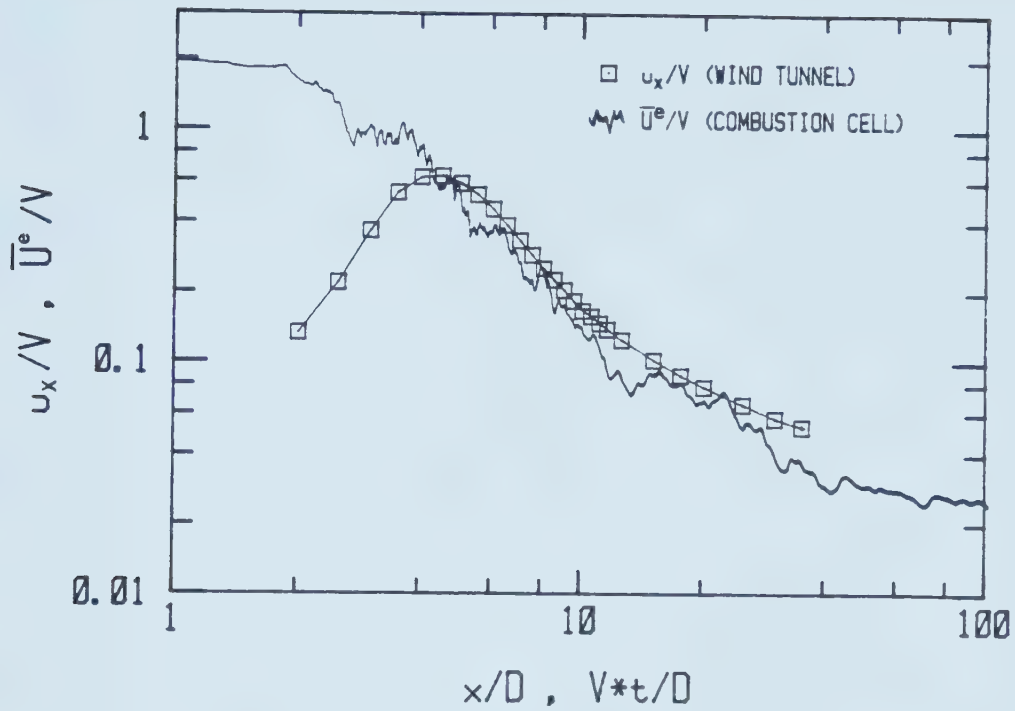


FIGURE 4.13

Comparing the Spatial Decay of Wind Tunnel Turbulence and the Temporal Decay of the Ensemble Mean Velocity in the Combustion Cell for the 20mmD Perforated Plate

velocity in the wind tunnel with the ensemble mean velocity in the combustion cell plotted on normalized axes. Within about four plate hole diameters the ensemble mean velocity in the combustion cell also contains a mean velocity component, and so is higher than the separated fluctuation velocity component of the wind tunnel hotwire reading. Beyond five diameters the ensemble represents the modulus of the x-y fluctuation velocity in the combustion cell, and is about 20% lower than the axial fluctuation in the wind tunnel, rather than larger as predicted in Equation 4.21 or 4.23. This may be the result of the slightly weaker jet production in the combustion cell noted earlier. If equation 4.21 is assumed true, then the streamwise fluctuation velocity u_x in the combustion cell is about 67% of its wind tunnel counterpart, based on the analogy between plate speed and bulk air speed in the wind tunnel.

There is satisfactory similarity in decay rate between the two data sets in the region beyond five diameters, showing that at least the decay exponents n (Eqn. 4.6 and Table 4.1) fitted to wind tunnel data are also applicable in the combustion cell. So although the prediction of turbulence intensity for combustion experiments based on the wind tunnel data fits may be slightly high, the control of intensity with decay time based on these fits will indeed be valid.

It follows from the similar decay rates that the turbulent dissipation is similar in both wind tunnel and

combustion cell (assuming no turbulence production in the decay period of interest). This coupled with the fact that the mechanism of turbulence production is identical in both cases, leads one to expect a corresponding similarity between the energy spectra, and thus the integral scales as well. Unfortunately this assertion is very difficult to test since the rapid decay rate precludes spectral analysis of a single combustion cell run, and generation of a spectrum from an ensemble would require a prohibitive number of runs. It is therefore necessary to simply assume in combustion experiments that integral scales determined from wind tunnel data are also applicable to combustion cell turbulence.

4.4 CONCLUSIONS OF CHAPTER 4

Turbulence behind the perforated plates in the wind tunnel is reasonably characterized by power law fits to turbulent fluctuation velocity and integral scale. These fits are summarized in Figures 4.4 and 4.10 respectively.

The turbulence in the combustion cell decays in the same way as that seen in the wind tunnel, but the RMS turbulent fluctuation velocity is slightly lower in the cell for a given equality of plate speed and bulk air speed in the wind tunnel.

There is sufficient agreement between wind tunnel and combustion cell turbulence measurements to justify the use of the wind tunnel power law fits to model in-cell turbulence. Based on those fits, the turbulence intensity

and scale in combustion experiments may be independently controlled by varying plate speed and decay time prior to ignition in the cell.

5. MEASUREMENTS OF FLAME GROWTH

This chapter discusses the techniques used to measure flame growth rate and flame speed through the premixed propane/air charge in the turbulent combustion cell.

Traditional procedures based on the dynamic pressure history, ionization detection, and direct photography were the chief diagnostics. An experimental method for directly measuring light emission from the flame reaction zone using an optically filtered photomultiplier was also evaluated. The results of this technique are presented in a separate section of this chapter.

Flame growth diagnostics in the combustion cell were first tested with laminar flames under quiescent (non-turbulent) conditions. These techniques were then extended to the measurement of turbulent flame growth.

A detailed description of the equipment used in all of these measurements is included in Chapter 3.

5.1 REPEATABILITY IN THE COMBUSTION CELL

Before discussing the flame growth measurements, it is necessary to indicate sources of uncertainty which affect measurement repeatability. In all experiments care was taken to insure the repeatability of identical runs by maintaining initial charge conditions at 101.3 ± 0.2 kPa and room temperature (22 ± 1 °C). Sufficient time was always allowed between subsequent runs for the cell walls to return to room

temperature and charge motion to settle prior to ignition as in laminar runs, or plate movement as in turbulent explosions.

The largest potential source of uncertainty was found to be in the mixture stoichiometry. Combined repeatabilities of constituent gas flowrates from mixer calibrations indicated an overall uncertainty limit of about $\pm 2\%$ in equivalence ratio. The effect of the mixture uncertainty is seen in Figure 5.1 which shows the variability in overall peak explosion pressure for quiescent runs at three different mixture settings. Also shown is a prediction of peak pressure produced with the STANJAN [37] computer program which assumes no heat loss but accounts for dissociation based on equilibrium concentrations of burned gas constituents. As one would expect, observed peak pressures are much less than the prediction, owing to heat loss. The observed data also appears to have a slightly greater slope, $d(P_e/P_i)/d\phi$ than the adiabatic prediction since combustion is more rapid for near-stoichiometric mixtures and so less heat is lost.

A simple parabolic fit to the observed P_e vs ϕ data gave an approximation of the slope and allowed mixture uncertainty to be inferred from peak pressure variability. The 14 stoichiometric runs shown had a mean pressure rise of $P_e/P_i = 8.99$ ($P_i = 1$ atm), with a standard deviation of 1.2%. Assuming no uncertainty in the pressure measurement, and multiplying this standard deviation by the slope,

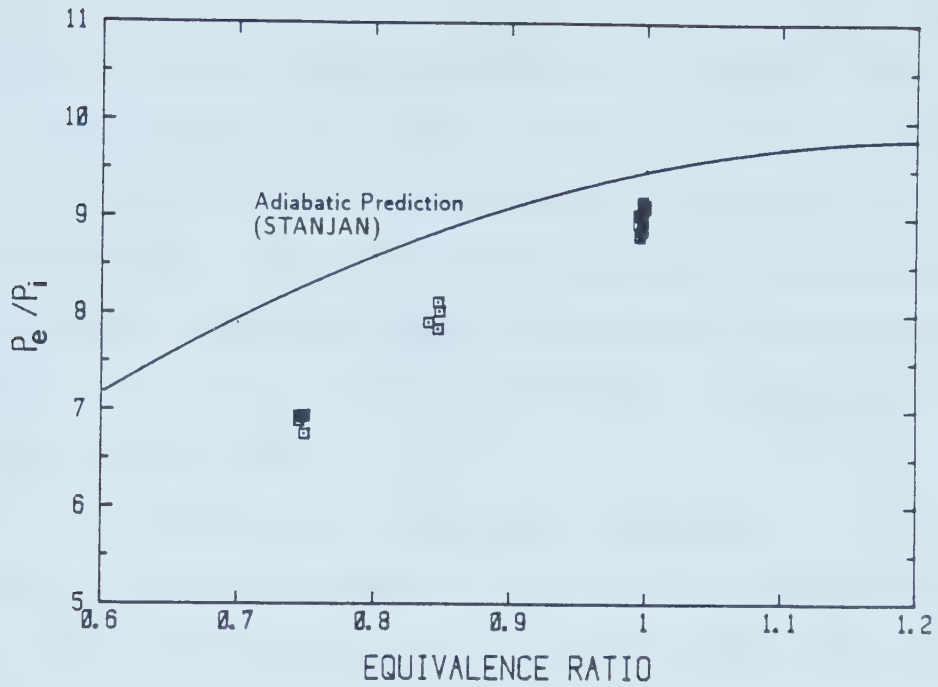


FIGURE 5.1 Variability of Observed Peak Pressure at Different Mixture Settings

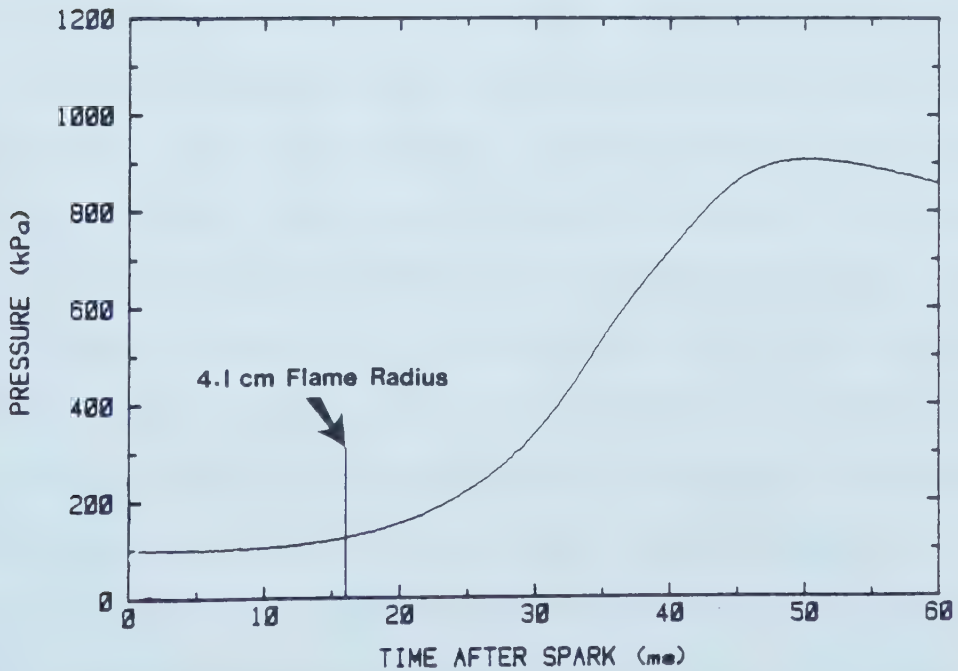


FIGURE 5.2 Pressure Record for a Stoichiometric Quiescent Explosion Showing the Flame Size Datum from the Ionization Sensor

$d(P_e/P_i)/d\Phi$, infers a mixture deviation of about 1.5%. Since this is consistent with the estimated mixture uncertainty limit of $\pm 2\%$, it is reasonable to assume that the equivalence ratio is the dominant source of uncertainty in combustion runs (provided that the pressure measurements are reliable). Static pressure transducer calibrations were repeatable within 0.5%.

The repeatability of quiescent explosions will become important in later discussion of the photomultiplier based burning rate indicator, as well as in turbulent explosion measurements.

5.2 MEASURING LAMINAR FLAME GROWTH

The high speed framing camera provided the most direct means for documenting the progress of the luminous flame front from the ignition point until the flame passed beyond the edges of the cell window. After ignition, the laminar flame was first seen as a small kernel 2 to 10 mm in diameter. It then progressed to a radially growing sphere, which remained essentially spherical until it was 80 to 90 mm in diameter, where it first began to distort toward a more cubical shape. In stoichiometric mixtures, there was no visible effect on early flame shape from the intruding spark electrodes. In the weaker mixtures (85% and 75%), there were slight indentations in the flame shell along the electrodes, but the essentially spherical shape was retained over the same range as that seen in stoichiometric mixtures.

When flame shape is known, a simple formulation based on ideal gas behavior can be made to predict the flame size from the instantaneous pressure during such confined flame growth. This is based on the work of Flamm and Mache [8] for which a detailed presentation is given by Lewis and von Elbe [7] where it is shown that the mass fraction burned is directly proportional to the fractional pressure rise:

$$X = (P - P_i) / (P_e - P_i) \quad \text{..... 5.1}$$

where X = mass fraction burned

P = instantaneous pressure

P_i = initial pressure

P_e = final pressure

This result is based on the following assumptions:

- 1) The combustion wave is a surface of discontinuity containing negligible mass and volume across which the complete change from unburned to burned state takes place.
- 2) The burned and unburned gases behave as ideal gases with constant specific heat ratios, and each region has uniform temperature and composition at any time.
- 3) The pressure is constant throughout the vessel at any instant.
- 4) There is no heat loss to the vessel walls.
- 5) Moles of products per mole of reactants remains constant throughout the process.
- 6) Pressure rise from the fraction burned X is small relative to the absolute pressure.

The volume of the burned gas, V_b , is the difference between the total volume, V_t , and the volume of the unburned gas V_u which has been compressed to pressure, P , and temperature, T_u :

$$V_b = V_t - (1-X)n_iRT_u/P \quad \dots\dots\dots 5.2$$

where n_i = initial number of moles unburned mixture

R = Ideal Gas constant

For isentropic compression of the unburned gas the unburned gas temperature is given by

$$T_u = T_i (P/P_i)^{(k_u-1)/k_u} \quad \dots\dots\dots 5.3$$

where T_i = initial temperature in the cell

k_u = specific heat ratio C_p/C_v of the unburned gas mixture

So substituting equations 5.1 and 5.3 into 5.2 and using the initial condition $n_iRT_i = V_tP_i$ gives the burned volume in terms of the pressure only:

$$V_b = V_t \{ 1 - [(P_e - P)/(P_e - P_i)][P_i/P]^{1/k_u} \} \quad \dots\dots\dots 5.4$$

Knowing that the flame is spherical, the flame radius is then:

$$r_b = \{ 3\pi V_t / 4 \{ 1 - [(P_e - P)/(P_e - P_i)][P_i/P]^{1/k_u} \} \}^{1/3} \quad \dots\dots\dots 5.5$$

In calculations of the flame size from equation 5.5, the specific heat ratio of the unburned mixture was the mole weight average of the specific heat ratios of the constituent gases at initial conditions. Data were taken from van Wylen and Sonntag [38]. The end pressure, P_e , was

not that which was measured, but rather was the adiabatic prediction shown in Figure 5.1. This was to ensure that the heat losses (which occurred predominantly in the final combustion stage with the flame near the walls) would not be reflected in flame size predictions in early flame growth where the adiabatic assumption is more reasonably applied.

Figure 5.2 shows a pressure history for a quiescent stoichiometric explosion. The ionization probe was inserted to sense flame arrival at a radius of 4.10 cm and this datum is included on this figure. The flame reached the 8 cm diameter within 16 ms after the spark. At this point the flame had travelled about $2/3$ of the distance from the ignition point to the wall, the flame area had grown to more than 100 times the spark kernel area, and the burned volume was 15% of the total cell volume. However, because of burned gas expansion, only about 3% of the ultimate pressure rise had taken place. Most of the mass was burned in the next 30 ms as the flame finished burning out to the wall and into the corners. Thus the output of the pressure sensor, which can measure the total pressure rise, was still very flat during the period where most of the flame growth occurred. This limitation is illustrated in subsequent figures where factors derived from early pressure rise are displayed on more sensitive scales and considerable noise is evident.

Figure 5.3 compares the flame size measured from the high speed photographs (750 frames/sec) and the pressure-predicted flame size from Equation 5.5. Also included is the

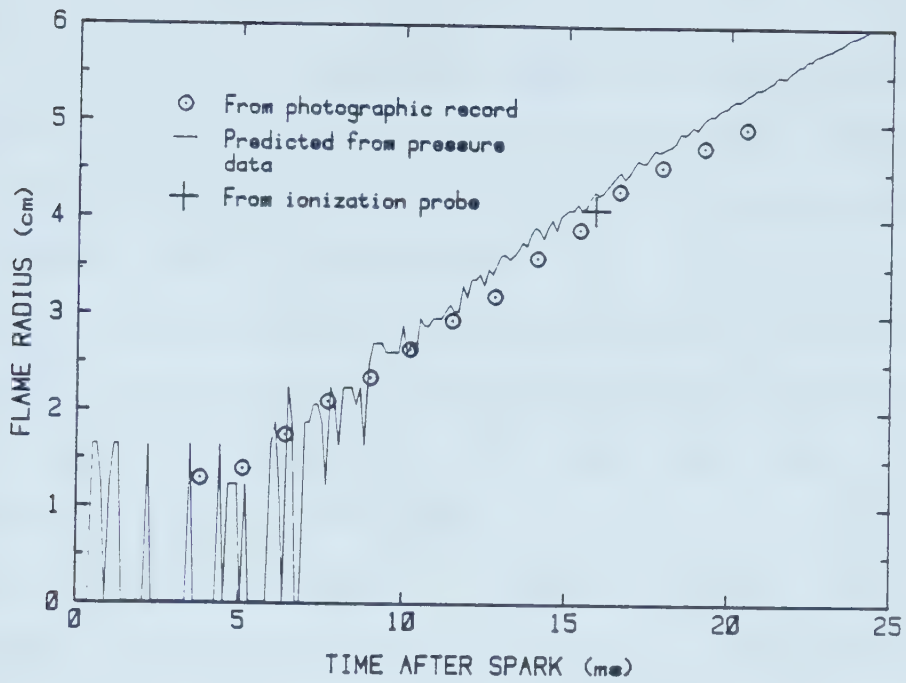


FIGURE 5.3 Comparing the Available Flame Size Measures

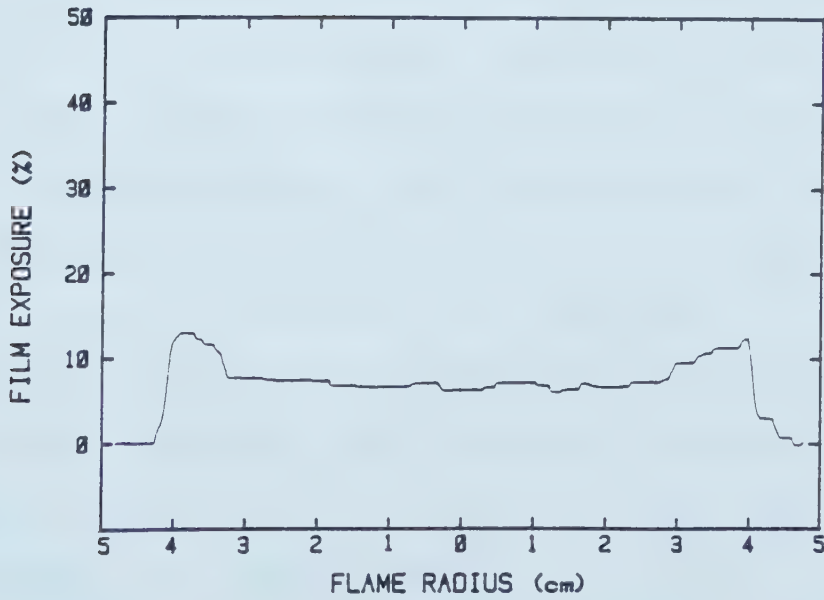


FIGURE 5.4 Microdensitometer Trace of a Photographed Laminar Flame Sphere (15.4 ms After Ignition)

datum from the ionization probe. Generally, the flame photographs indicated a smaller radius than that required to produce the observed pressure rise, with the photographed flame radius being consistently 2 to 3 mm lower. This difference is explained by considering limitations of photography. Photographing a spherical flame results in the greatest optical density on the film at a point corresponding to the inside edge of the flame front, since the path through the flame is longest there. Thus direct photographs of spherical flames, which are of necessity at the limits of the film speed, tend to show a ring of flame which is too small by the thickness of the luminous flame zone. This uncertainty in photographed flame size may be quantified somewhat with a microdensitometer. Figure 5.4 shows the relative optical density of the flame image on the frame at 15.4 ms after the spark. The bright inner ring is clearly visible. Extending beyond this is a gradient zone of about 3 mm, attributable to both the shallower flame depth at the outside of the sphere and the actual progression of the flame during the interval that the shutter was open. In this case the flame had progressed about 1.3 mm during the 0.5 ms shutter interval. The flame size measured from the microdensitometer traces was based on the bright edge and did not include the gradient zone.

The response of the ionization probe, although not studied in detail in this work, might be expected to lag slightly behind the actual flame front if the probe tip were

to cause any quenching effects. This technique was studied in steady flames by Karlovitz et al [39] who showed that in fact the highest concentration of positive ions was on the order of about 1 mm ahead of the zone of hot combustion products (the luminous zone) in hydrocarbon flames. This uncertainty is of little concern here however, since the run to run repeatability discussed earlier manifested a variability of about ± 1.5 mm in flame radius at 15 ms after the spark. The ionization sensor was not used extensively in turbulence experiments due to its low tolerance to plate motion shock and also because satisfactory results could be had with the pressure based diagnostics and photography.

The level of agreement between the pressure predicted flame size and that indicated by the other methods proves that the pressure based method is reasonable and consistent for measuring laminar flame growth. Moreover, the pressure record is continuous so growth factors such as mass burning rate and burning speed are easily derived. Finally, pressure recording is free of the complications of ion detection and high speed photography, so it was chosen as the chief diagnostic in the bulk of combustion cell experiments.

5.2.1 LAMINAR FLAME SPEED

Using the approach of Lewis and von Elbe [7] the laminar burning velocity can be estimated from the radial growth rate of flame which is the coupled effect of laminar burning and the expansion of the burned gas. This formulation is

based on the same assumptions outlined earlier.

First, for simplicity, an effective radius of the combustion cell is defined:

$$a = (3V_t/4\pi)^{1/3} \dots\dots\dots 5.6$$

where a = effective cell radius

Accounting for the turbulence plate, rods, electrodes and other intrusions, $a = 7.66$ cm.

The nominal radius, r_i is the radius of the spherical volume occupied by the mass fraction X of unburned gas which upon burning gives rise to the pressure P , therefore:

$$r_i = ax^{1/3} \dots\dots\dots 5.7$$

If, during the growth of the flame, the burned gas had not expanded, then an element dr_i would represent the thickness of a shell of unburned mixture at the initial state P_i and T_i about to be traversed by the flame in time dt . The volume of this shell is

$$dV_i = 4\pi(r_i)^2 dr_i \dots\dots\dots 5.8$$

However, through burned gas expansion, the radius of the shell has increased from r_i to r_b and the temperature and pressure to T_u and P . Thus its volume has become

$$dV_b = 4\pi(r_i)^2 dr_i (T_u P_i / T_i P)$$

where Equation 5.3 is used to eliminate temperature terms.

The burning velocity S_u can also be used to express the the thickness of the expanded shell as $S_u dt$, so its volume is

$$dV_b = 4\pi(r_b)^2 S_u dt \dots\dots\dots 5.9$$

By equating 5.8 and 5.9, an expression for burning velocity

is written uniquely in terms of pressure derived factors:

$$S_u = dr_i/dt(r_i/r_b)^2(P_i/P)^{1/ku} \quad \text{..... 5.10}$$

Since all of the variables in Equation 5.10 are in terms of the pressure, P and the derivative, dP/dt , the high noise to pressure rise ratio in the early pressure history necessitated the use of smoothing to obtain reliable results. A sixth order polynomial was used to fit the raw pressure data and the effects of spark noise on the fit were removed by mirroring the inverted signal onto the negative time axis, and including it in the fit. This technique ensured a smooth fit through the time origin. Figure 5.5 shows a typical fit on the early pressure history of a stoichiometric quiescent run where some mirrored data is also shown. Figure 5.6 compares the derivative of the smoothing polynomial with that of the raw data, demonstrating that this technique gave a reasonable smoothing function for the otherwise erratic derivative.

With the smoothed pressure data, Equation 5.10 gives the flame speed history shown in Figure 5.7 plotted against flame radius for a quiescent run. This is compared to the laminar flame speed predicted according to the correlation of Metghalchi and Keck [9]. This prediction starts at about 32 cm/s and increases with flame travel due to assumed adiabatic compression of the gases ahead of the flame front. The measured burning velocity was somewhat higher, starting at 35 cm/s, but had a lower rate of increase with increased

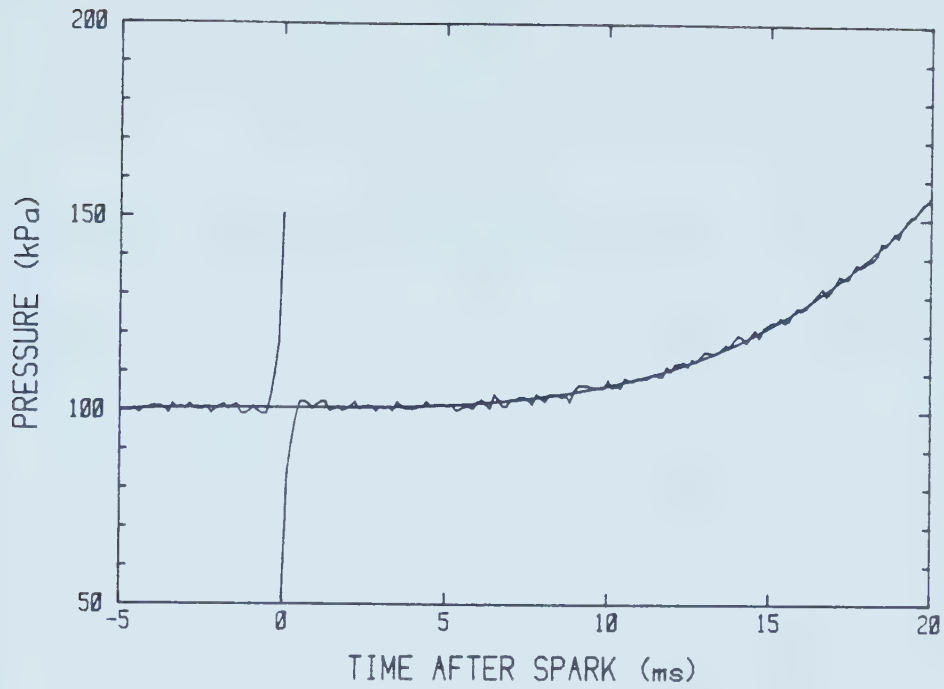


FIGURE 5.5 Smoothing the Early Pressure Signal

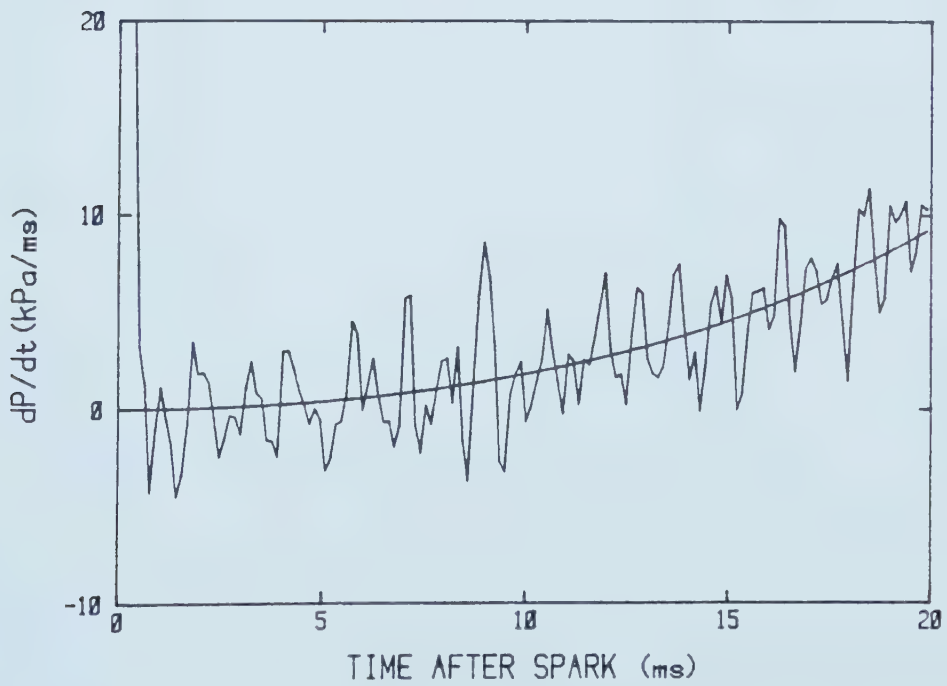


FIGURE 5.6 Comparing the Derivative of the Raw Pressure Signal With That of the Smoothing Function

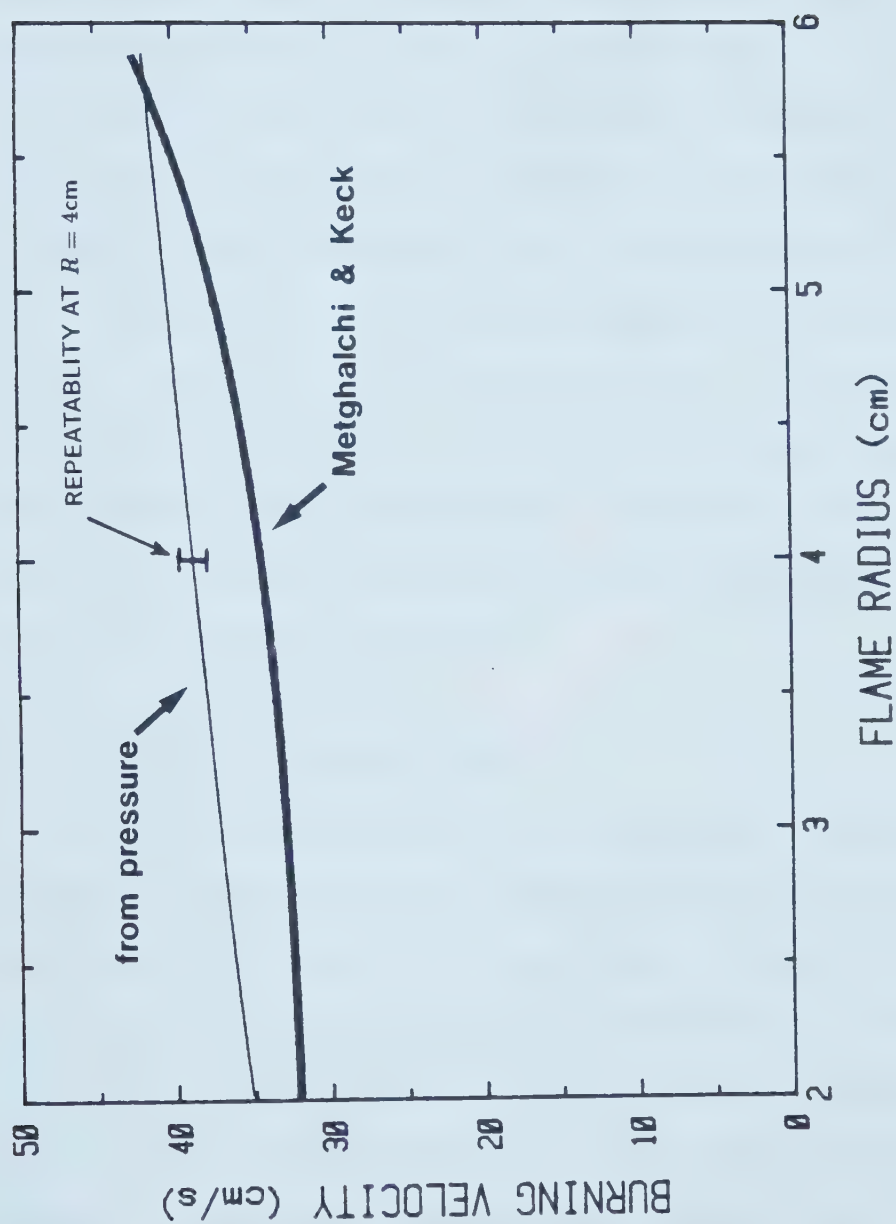


FIGURE 5.7 Comparing Flame Speed Derived from Smoothed Pressure Record With That Predicted With the Correlation of Reference [9]

pressure. The latter difference most likely arises from the limitations of Equation 5.1. The repeatability of this measurement over 14 similar quiescent runs is illustrated with an error bar at the 4 cm flame radius.

It has been shown that with polynomial smoothing, the the flame speed could be abstracted from the early pressure history of the growing flame. By evaluating the flame speed at a fixed flame size rather than at a fixed time after the spark then only the repeatability in flame speed is of concern, since the variability in combustion duration is eliminated. Also, the effect of calculation method on the relative results is reduced since comparisons are carried out at a constant pressure.

5.3 TURBULENT FLAME SPEED

For this discussion, the turbulent flame speed, S_t , is defined as the rate of propagation of an imaginary smooth envelope enclosing the burned gas volume, even though the turbulent flame front may be distorted or discontinuous. By this definition, the turbulent flame speed is directly analagous to the laminar flame speed and constitutes a bulk measure of burning rate, which is of most use in engine combustion studies. This is also consistent with the generally accepted definition for S_t arising from burner studies as the average velocity of the turbulent mixture flowing through a stationary, planer flame (Ref 7).

Once the continuous envelope model is assumed, certain

assumptions used in the laminar flame speed measurements of the previous section must be examined.

1) That the actual flame front is stretched and wrinkled by turbulence would not contradict the important assumption that the reaction zone has negligible volume if the local reaction zones are still on the same order of thickness as that of the laminar flame. This is essentially the assumption on which the wrinkled flame model is based [11].

2) The assumption of a spherical flame volume is not violated since flame shape was seen from high speed photography to remain essentially spherical over roughly the same range as that of the laminar flame front for the moderate turbulence levels used in this study.

3) One assumption of the previous section which could be compromised is that of negligible heat loss. Certainly convective heat transport from the compressing unburned gas to the cell wall will be enhanced by the turbulence. However, since the pressure rise is still small after the flame has travelled $2/3$ of the distance to the wall, those losses are small compared to the thermal energy released into the expanding burned gas by combustion. Also, burning is much faster, so there is less time for heat loss to occur.

4) With the presence of turbulence there must also be instantaneous spatial variation in pressure, but since the turbulence is homogeneous, those variations will vanish on average. So the assumption of uniform pressure would still

apply over volumes much greater than the size of turbulent motions, and such is the case using the formulation of the previous section.

Figure 5.8 compares the radius of a spherical, weakly turbulent flame from the high speed photographs (750 frames per second) with that calculated from the unsmoothed pressure history according to Equation 5.5. As seen before with the laminar flame, the pressure predicted radius was slightly larger than that measured from photographs. The uncertainty in flame size from the photographs was greater in this case, as can be seen from the microdensitometer trace in Figure 5.9. The gradient zone at the flame edge was about 20% of the total flame radius. It is also obvious that this turbulent flame was much brighter than the laminar flame of Figure 5.4.

The reasonable agreement between the pressure predicted flame growth and the visible flame size from photographs combined with the availability of continuous traces allowed this pressure technique to be applied in measuring relative turbulent flame speeds in the combustion cell. Results of flame speed variation with turbulence parameters are presented in Chapter 6.

5.4 PHOTOMULTIPLIER BASED DIAGNOSTICS FOR FLAME GROWTH

The low pressure rise in the early flame growth stages limits the resolution of pressure based measurements, so a more sensitive monitoring scheme based on the light emitted

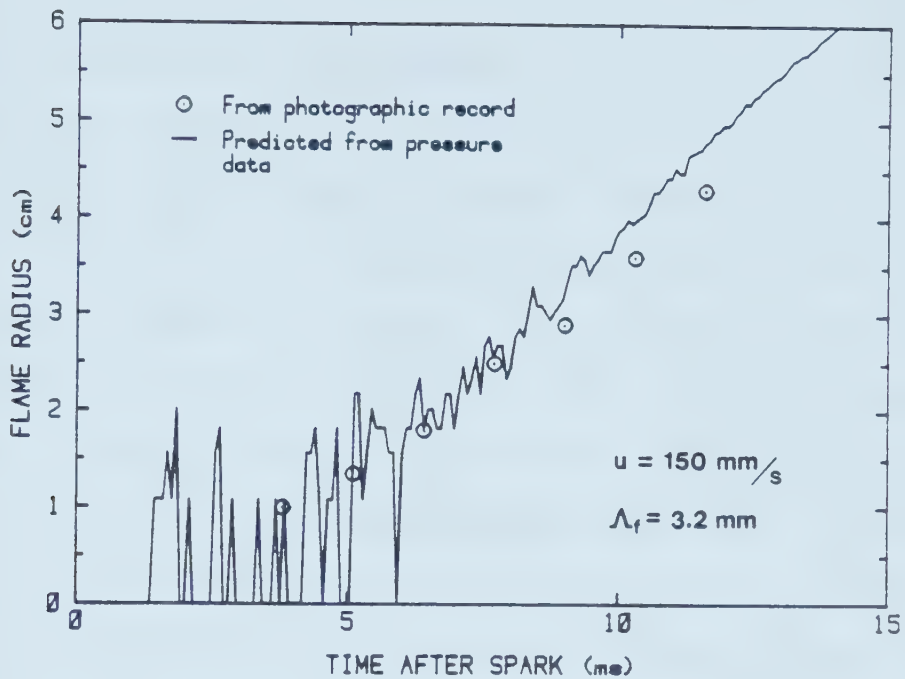


FIGURE 5.8 Comparing Photographed Flame Size With Pressure Prediction For a Moderately Turbulent Flame.

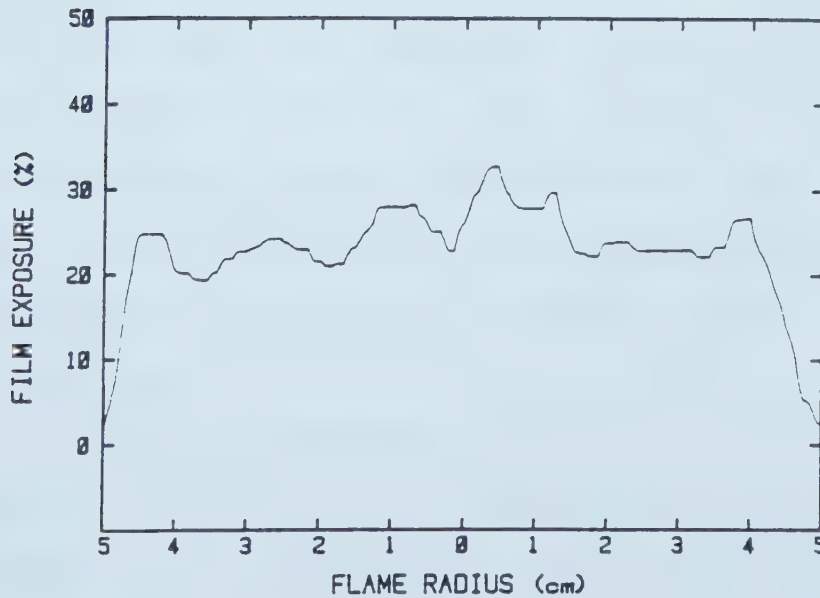


FIGURE 5.9 Microdensitometer Trace of a Photographed Turbulent Flame (11.6 ms After Ignition)

from the growing flame was examined.

Using an optically filtered photomultiplier, it is possible to monitor early growth rates of quiescent and turbulent flames in the combustion cell based on the visible radiation of species present only in the flame reaction zone. In lean hydrocarbon flames one of the most conspicuous of these is the CH radical, which emits a prominent band at 431.5 nm, the characteristic bright blue seen in the inner cone of a bunsen burner flame. The excited CH radicals are produced in significant concentrations only in the hottest part of the reaction zone and are diffuse enough that reabsorption of the light from one flame front passing through another flame zone is minimal. Thus CH emission measurement gives an indication of the total reacting volume or flame front area in the cell.

This approach was described by Hurle et al [40] for measuring burning rates in open burner flames and was extended to closed vessel experiments by Checkel [3]. This technique was investigated in the present work to evaluate its advantages and limitations compared to the other flame growth measures.

Of fundamental importance in such measurements is the assumption that the photometric emissions of the flame front are a function of mass burning rates only, and that there are no secondary effects arising from turbulence. The work of John and Summerfield [41] shows that in reality, the radiation intensity per unit mass burned of the species CO_2 ,

C_2 , and CH in propane/air burner flames can be decreased by as much as 20% from that of the laminar flame for a highly turbulent flame. This effect is most pronounced for stoichiometric and richer flames and particularly severe for the CO_2 emission. Since CO_2 has a high concentration in the burned gas as well as the reaction zone, this effect may be related to reabsorption when multiple, overlapping flame fronts are present. For the 431.5 nm CH band, these researchers showed the effect of turbulence to be less significant particularly for leaner mixtures, so the CH emission is suitable as a burning rate diagnostic for moderately turbulent explosions.

The apparatus used in the presents study is described in detail in Chapter 3, Section 3.5.2. Basically it consisted of a photomultiplier optically filtered to respond to the 431.5 nm band. A lens and frosted glass diffuser were used to cast a randomized image of light from one window of the cell on to the photocathode of the photomultiplier tube. The randomization was to ensure that the system was equally sensitive to light from all parts of the cell. The photomultiplier was configured to provide a voltage output proportional to photocathode current and the output was recorded simultaneously with other explosion sensors.

It would be desirable to measure either flame area or mass burning rate directly from the photomultiplier trace. With adequate information on the flame composition and state of substances in the flame zone, it might be possible to

predict the CH light emission as a function of burning rate and thus provide a fundamentally based calibration for the photomultiplier system. However even if this could be done, the complications of losses in the light collection optics and of quantifying photomultiplier response would prevent the calibration from being absolute. A practical calibration of the photomultiplier signal can be made against the other measures of laminar flame size shown in Figure 5.3.

Figure 5.10 shows the calibration of flame area against the photomultiplier output for the same stoichiometric quiescent explosion of Figures 5.2 and 5.3. The flame area values from both the pressure predicted flame size and the photographs are shown. It is seen that the photomultiplier response is quite linear.

It is also possible to calibrate the photomultiplier directly against mass burning rate. The mass fraction burned can be measured directly from the fractional pressure rise (Equation 5.1), or it may be inferred from photographed flame size and the corresponding instantaneous pressure using the ideal gas equation (if the burned zone is assumed to be uniform and at the flame temperature appropriate to that mixture at the temperature and pressure of the unburned gas). For the latter calculation a realistic value for adiabatic flame temperature was taken from the correlation of Chang and Rhee [42]. The result of this calibration in Figure 5.11 is an almost linear relationship between instantaneous mass burning rate and photomultiplier output.

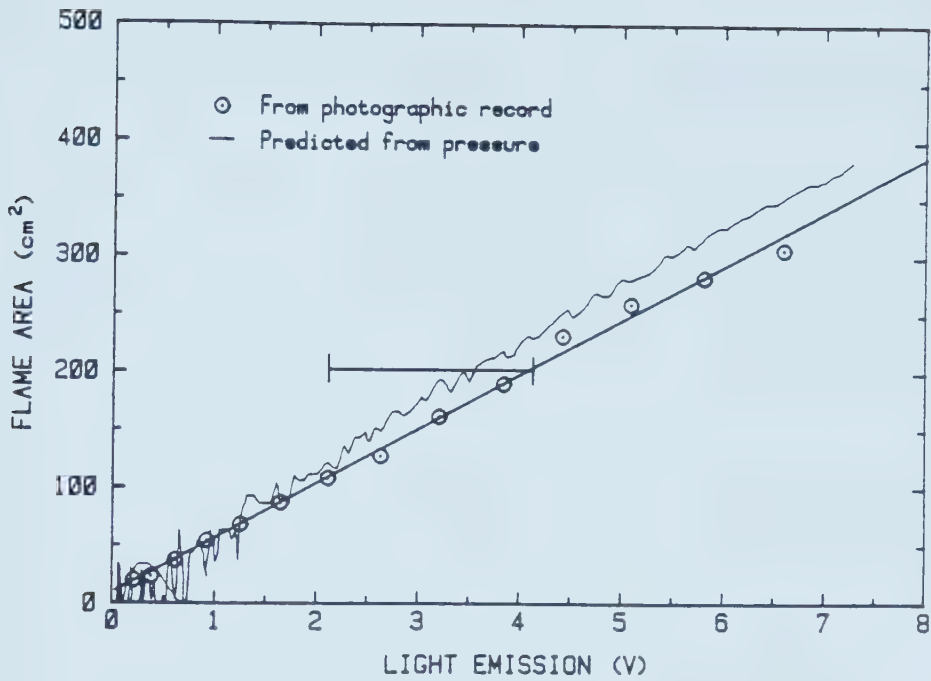


FIGURE 5.10 Calibration of Photomultiplier Output to Laminar Flame Area

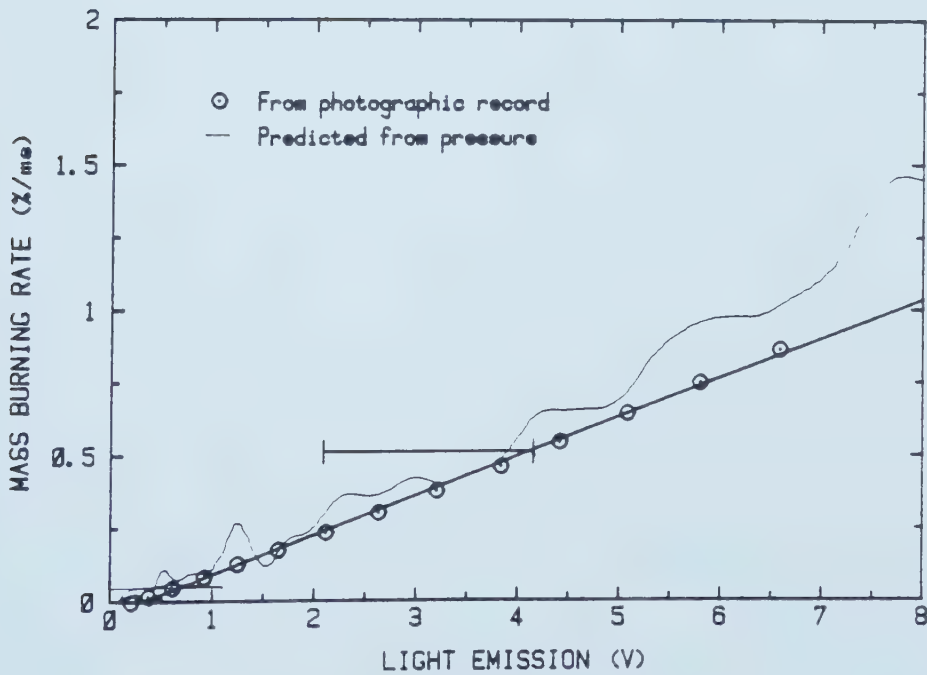


FIGURE 5.11 Calibration of Photomultiplier Output to Mass Burning Rate.

Again, the photographs slightly underestimate the fraction burned relative to the pressure record. (Note: for this figure, the pressure derived data was smoothed using a simple digital filter which was later discarded in favour of the polynomial regression discussed earlier in this chapter).

Unfortunately, the repeatability of these calibrations was extremely disappointing. The variability of the response over several identically prepared quiescent runs is illustrated on Figures 5.10 and 5.11 by error bars at a 4 cm flame radius. The photomultiplier showed very little drift and the warm-up time prior to each run was similar, so it is a reasonable conjecture that the large variability was a manifestation of mixture uncertainty. John and Summerfield [38] supplied data for the variation of CH concentration with mixture strength for a laminar propane-air flame at atmospheric conditions. This data indicates that a $\pm 2\%$ variation in equivalence ratio could be expected to produce about $\pm 12\%$ change in CH concentration in a stoichiometric flame. This would not account for the $\pm 30\%$ variability seen on the two calibrations, so non-linearity of optical system sensitivity may be compounding the error.

It was unfortunate that this promising technique was undermined by unacceptable repeatability which rendered it less reliable than the elementary pressure based techniques. For this reason, further results based on this method will not be presented in this work. Refinements in the

photomultiplier apparatus and better mixture control would undoubtedly yield more satisfactory results.

6. RESULTS OF TURBULENT COMBUSTION EXPERIMENTS

This section presents the results of combustion measurements for various conditions of controlled pre-ignition turbulence. The turbulence parameters of chief interest in these experiments were the root mean square intensity, u , and the integral scale, Λ , which were calculated from measured perforated plate speed using the turbulence decay functions presented in Chapter 4 (Figures 4.4 and 4.10). Through independent control of the plate speed and the delay between the plate passage and ignition, the turbulence intensity and scale at the time of the spark could be independently controlled. In order for the decay functions to properly apply, the non-dimensional delay between plate passage and ignition was always

$$Vt/D \geq 10 \quad \text{.....} \quad 6.1$$

where V = plate speed

t = delay between plate passing cell
centre and ignition

D = plate hole diameter

The integral scales at ignition generated in these experiments ranged from 1 to 11 mm, and rms intensities at ignition from 10 to 90 cm/s.

The majority of the experiments were performed with fixed integral scales at ignition (one for each perforated plate size), and varying intensities. A series of stoichiometric runs were also performed where the intensity

at ignition was held fixed, and the integral scale varied. Three different mixtures were examined: 75, 85, and 100% stoichiometric. The initial conditions of 101.3 kPa and 22°C were fixed for all experiments.

6.1 EFFECTS OF TURBULENCE ON OVERALL COMBUSTION

The net energy available from the constant volume explosion is indicated by the maximum pressure reached. Figure 6.1 shows the effect on peak pressure of increasing intensity for fixed integral scales at ignition. Note that stoichiometric experiments employed four distinct scales, and leaner mixtures only two. The quiescent (no turbulence) datum is also shown on each plot.

The lowest turbulence intensity clearly increased the peak pressure over the quiescent case for all three mixtures, but further increasing intensity only slightly enhanced peak pressure. The theoretical peak pressure curve presented in Chapter 5 (Figure 5.1) predicts pressure rises P_e/P_i of 8.3, 8.9, and 9.5 for the 75%, 85%, and 100% mixtures respectively, and these data are included on Figure 6.1. That these predictions were exceeded is attributed to mixture uncertainty, especially as the propane was only 98% pure so more energetic hydrocarbons are likely present.

The larger integral scales appear to result in slightly higher peak pressures, and this is most apparent in the stoichiometric data of Figure 6.1. At an intensity of 50 cm/s, increasing the integral scale from 1.4 mm to 10 mm

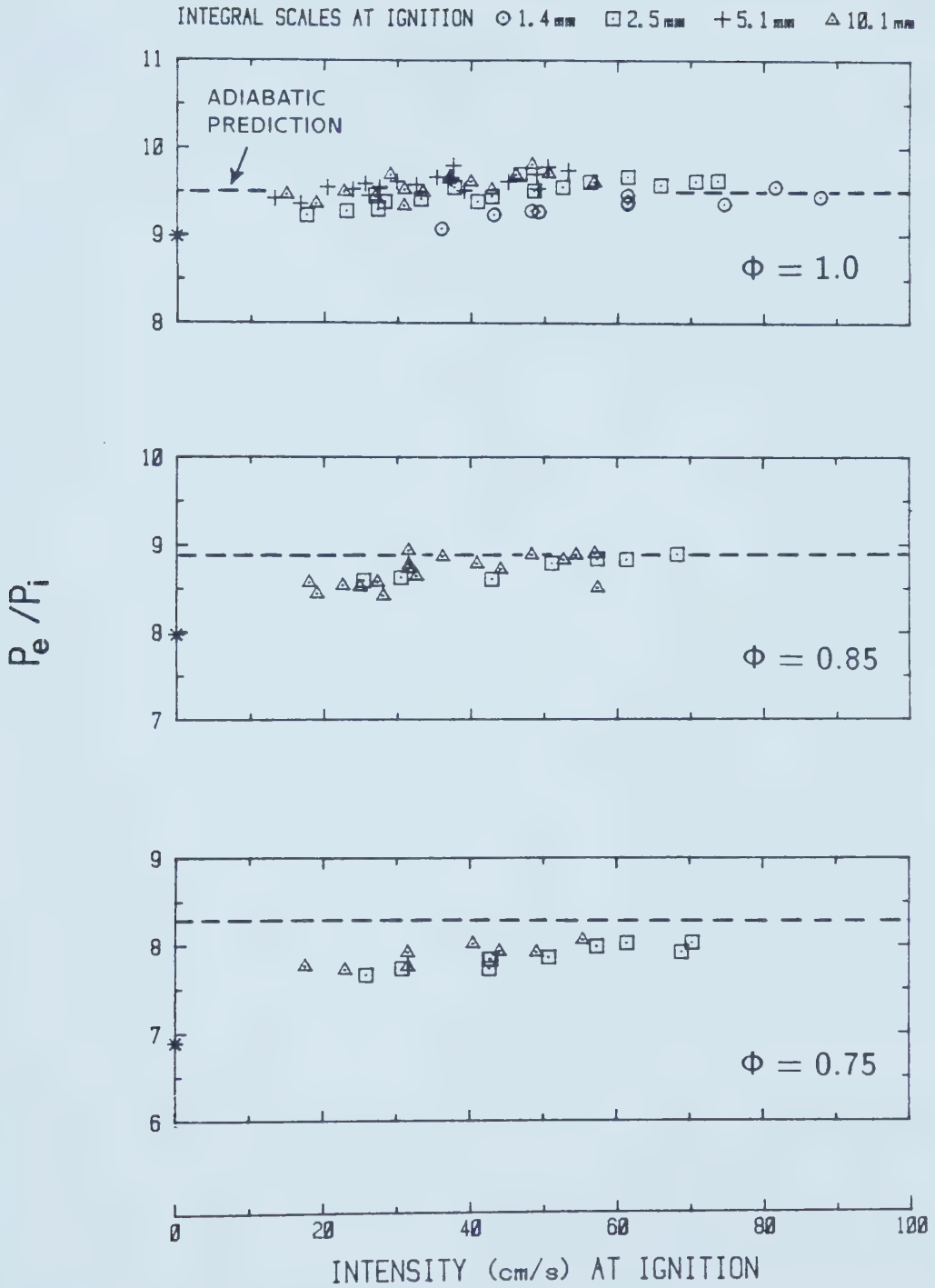


FIGURE 6.1 Dependence of Maximum Pressure Rise on Ignition Time Intensity (Integral Scales Fixed at Ignition)

increased the pressure rise P_e/P_i from 9.3 to 9.7.

It is most likely that the turbulence increases the ultimate pressure by reducing overall heat loss with reduced combustion duration, particularly since the increase in P_e over the quiescent value is greatest for lean mixtures.

Combustion duration is also important with respect to spark ignition engine application, since it determines the departure from the ideal Otto cycle and thus the efficiency of the engine. The combustion duration has been defined here as the time from ignition to reach the peak pressure. Figure 6.2 plots combustion duration for the varying intensity experiments. The effect of intensity is more apparent in this figure, with burning times decreased by nearly 50% of the quiescent value, over the range of intensities used.

The effect of scale is not clear in Figure 6.2 however. For the stoichiometric runs, the shortest and longest burning times consistently resulted from the 5 and 10 mm scales respectively, while the smaller 1.4 and 2.5 mm scales data were somewhere between. Conversely, for the 75% mixture, the larger scale brought shorter burning times, and there was no clear scale effect in the 85% data.

Since the time to peak pressure must be affected by the shape of the combustion chamber, particularly from heat lost in the later stages of combustion, a more objective measure of combustion duration was afforded by considering the interval where the flame was still growing spherically. Figure 6.3 shows the time from ignition for the flame to

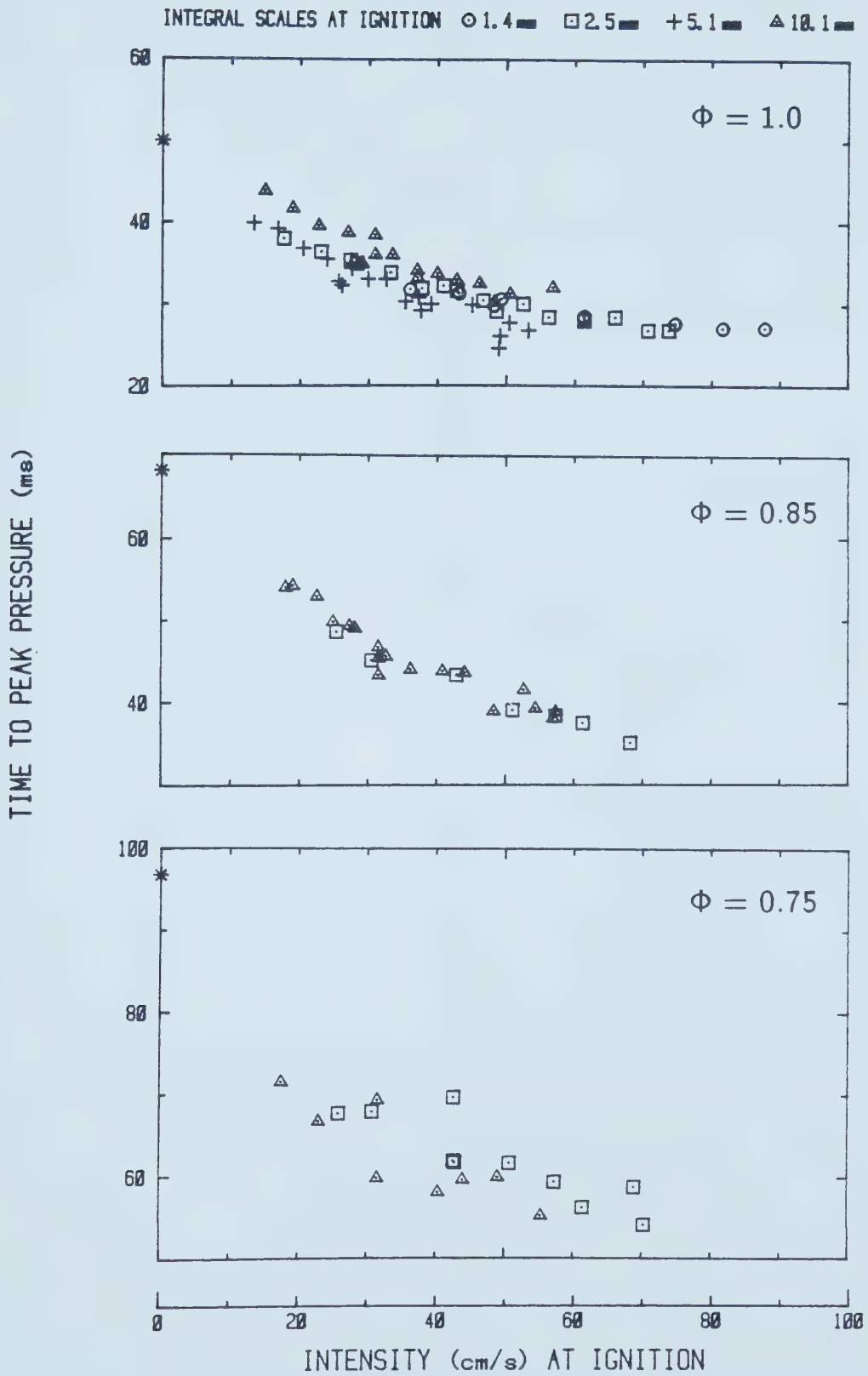


FIGURE 6.2

Dependence of Time to Reach Maximum Pressure on Ignition Time Intensity (Integral Scales Fixed at Ignition)

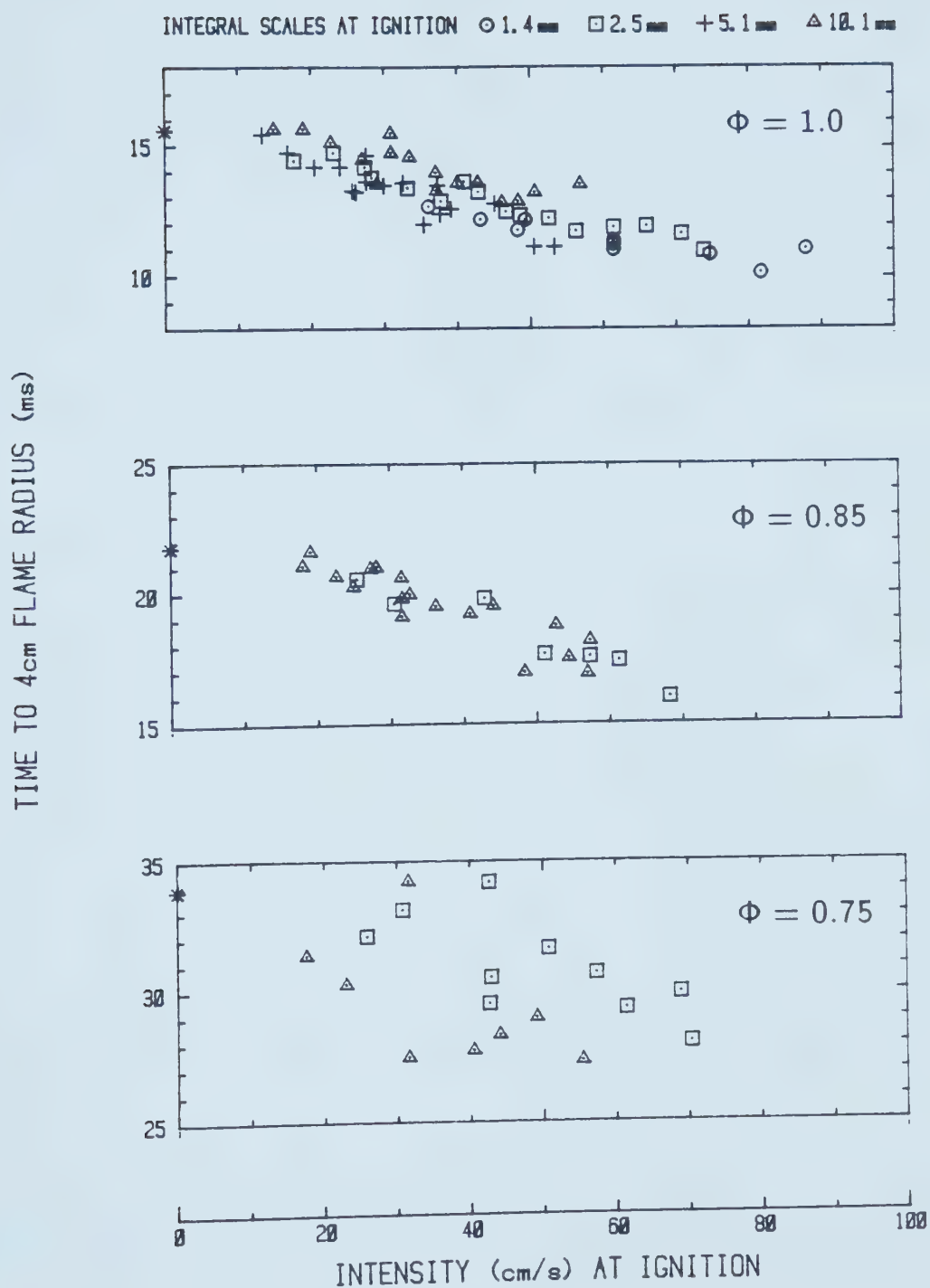


FIGURE 6.3

Time For Flame to Reach a 4 cm Radius for
Varied Ignition Time Intensity and Fixed
Integral Scales

reach a 4 cm radius. The distribution of data in these plots is similar to that seen on the previous figure, with the exception that the decrease in burning time from the quiescent runs was at best about 30%. Comparing the relative and absolute decreases in burning time between Figures 6.2 and 6.3 indicates the importance of the turbulence in enhancing combustion in its latter stages.

The results discussed so far have been based on the experiments where ignition time integral scales were held fixed, and the intensity varied. Figure 6.4 presents burning time results of stoichiometric runs where the intensity at ignition was fixed at 50 cm/s, and the scales varied. As in the previous figures, a different plotting symbol is used to distinguish which perforated plate was used. These plots agree with the earlier observation that an intermediate (5 mm) integral scale induced the shortest combustion durations. However, there appears a slight trend toward shorter burning times for the smaller scales at this intensity.

Since dissipation (ie decay rate) is inversely proportional to integral scale (recall Eqn. 4.15), Figure 6.4 also illustrates the relatively slight importance of dissipation compared to ignition time intensity in the range of turbulence tested.

6.2 BURNING SPEEDS AND TURBULENCE

Burning speeds were estimated from pressure records

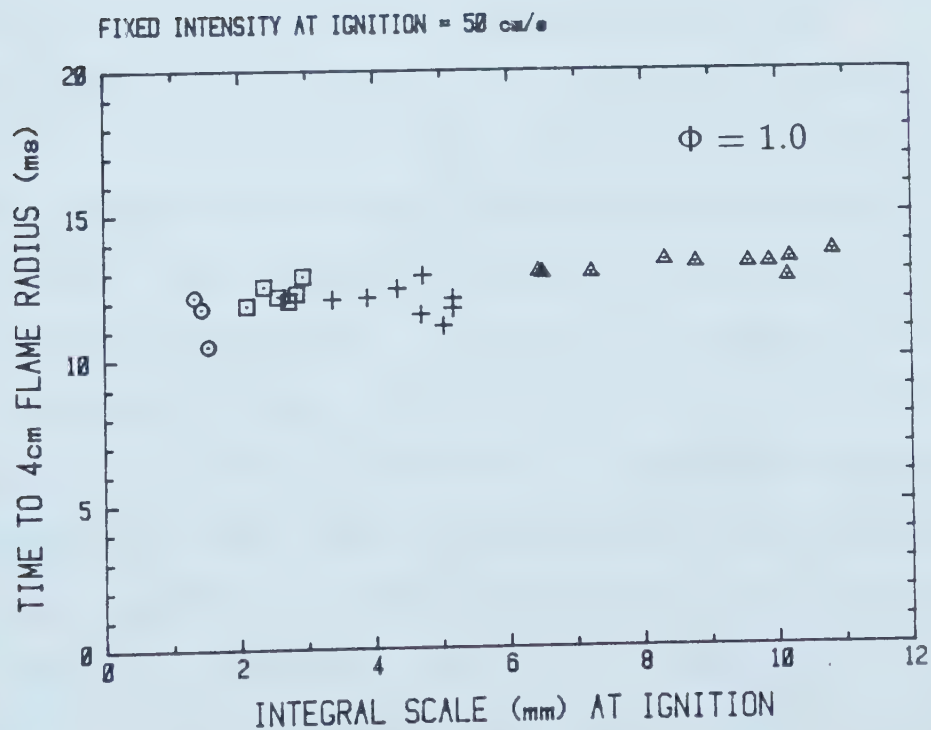
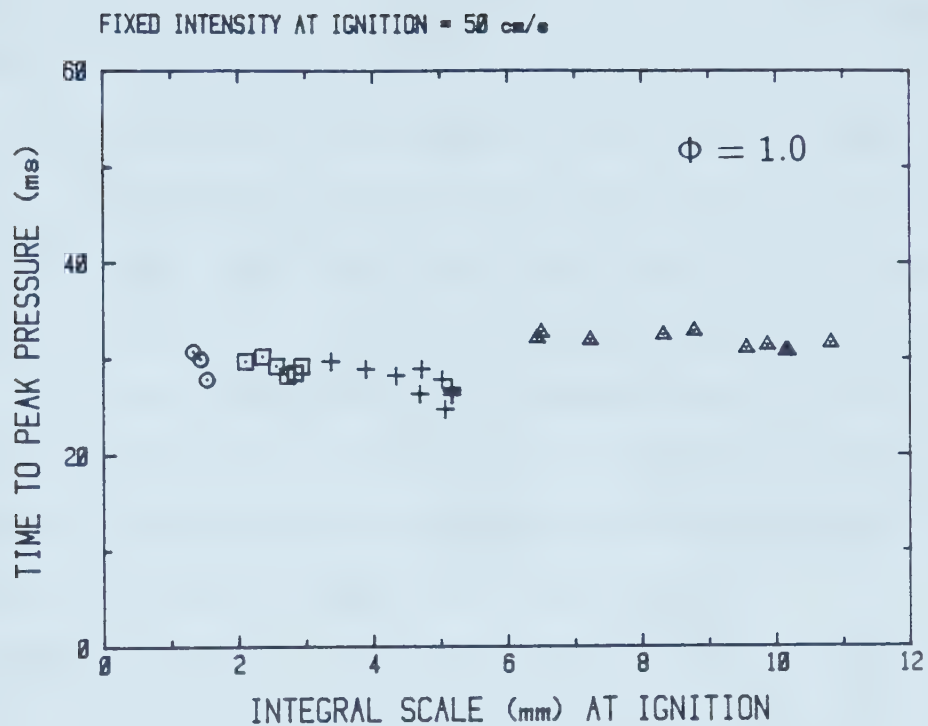


FIGURE 6.4

Times to Peak Pressure and 4 cm Flame Radius
For Varied Ignition Time Integral Scale, Fixed
Intensity (Stoichiometric Only)

using the technique detailed earlier in Section 5.3. For comparison, speeds were calculated at a fixed flame radius of 4 cm. At this point the pressure rise is high enough that signal to noise ratio is good, yet was still within the range of accurate flame size prediction based on pressure. Traces of flame speed against radius showed that at 4 cm radius the flame speed was also fairly constant. This period of constant flame speed was described by Lancaster [21] as the "fully developed" regime of flame growth.

Turbulence levels at the 4 cm time were calculated assuming that the flame had no effect on the turbulence: that is the pre-ignition decay functions still apply. This disregards the following counteracting mechanisms:

- 1) with compression heating of the unburned gas the viscosity rises, and with it the turbulent decay rate;
- 2) The expanding flame front distorts the turbulence in its path, and increased intensity is expected according to Townsend's [25] rapid distortion theory.

A theoretical study of the evolution of turbulence during constant volume combustion in a cylindrical vessel was presented by Hoult and Wong [24], where rapid distortion theory was applied to the 2-dimensional, axi-symmetric, central ignition case. One result of this study was that turbulence in the unburned zone depends only on initial values and the degree of compression. Integral scales varied inversely with the square root of the fractional increase in density, and intensity depended on both density rise and

flame radius. For engine-like conditions, it was seen that intensity should be relatively constant over the combustion process, at about twice the initial level.

The use of the rapid distortion theory for the present study is questioned however, since Townsend's theory required that the duration of the distortion be much shorter than the turbulent decay. This is certainly not generally the case in the turbulent combustion cell where decay time constants ranged from 4 ms to 340 ms, and the times to 4 cm flame radius ranged from 10 ms to 35 ms for the various mixture and turbulence conditions.

Predicting turbulence levels during combustion using the normal decay functions in this study is expected to slightly underestimate the intensity, and since the density increase is small at the 4 cm flame, the overestimate of integral scale will be almost negligible.

6.2.1 BURNING SPEED RESULTS

Figure 6.5 presents burning speed data from stoichiometric runs where ignition time intensities were varied for fixed integral scales. However, the turbulence parameters were calculated for the time of the 4 cm flame radius. These data indicate a linear dependence of burning speed on intensity, and a negative correlation to integral scale, where the smaller scales further enhance flame speed over the larger scales, at a given intensity.

Least squares lines were fitted through data for each

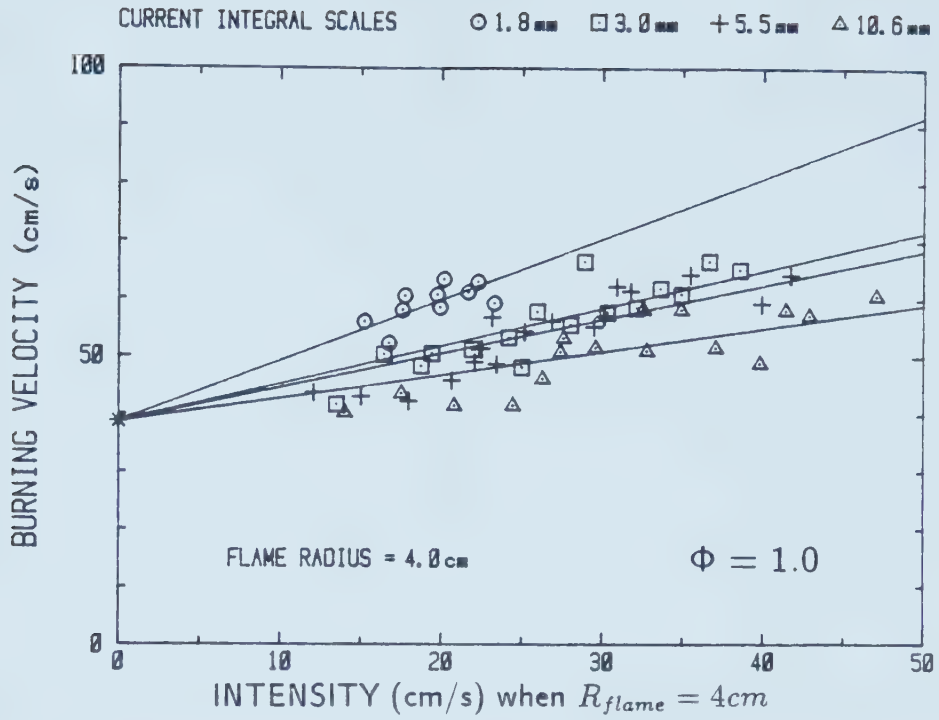


FIGURE 6.5 Turbulent Burning Velocity Dependence on Instantaneous Intensity and Integral Scale

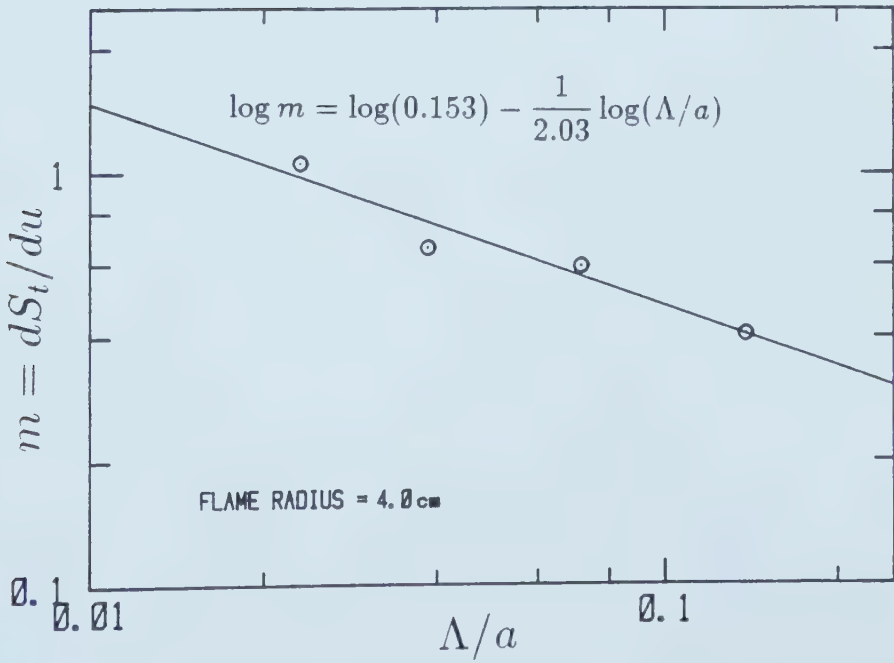


FIGURE 6.6 Fitting the Intensity Dependence of Burning Speed to Integral Scale

scale subject to the constraint that they pass through S_u at zero intensity. The value of $S_u = 38$ cm/s is taken from Figure 5.7 for a flame radius of 4 cm. The slopes, $m = dS_t/du$, of these fitted lines are given in Table 6.1 and are plotted on logarithmic axes in Figure 6.6 against integral scale normalized for convenience with the effective combustion chamber radius ($a = 7.66$ cm). It is apparent from Figure 6.6 that the dependence of S_t on u varies with $\Lambda^{-1/2}$. Figures 6.5 and 6.6 suggest a correlation of the form:

$$S_t = S_u + B u (\Lambda/a)^{-1/2} \quad \dots\dots\dots 6.2$$

where $B = 0.15$ is also provided by the fit in Figure 6.6.

TABLE 6.1 Dependence of Burning Speed on Intensity
As It Varies With Scale

$$S_t = S_u + m u$$

Λ (mm)	Slope, m
1.8	1.06
3.0	0.66
5.5	0.59
10.6	0.41

In order to isolate the effects of mixture composition and temperature, the common approach is to normalize turbulent burning speed with the laminar flame speed at the same conditions. In assembling results from a number of sources, Abdel-Gayed and Bradley [17] showed strong

correlations of S_t/S_u with S_u/u , so a similar procedure was implemented here, while incorporating the observed correlation with $\Lambda^{-1/2}$. The laminar burning speeds used in this normalizing scheme were those actually measured in the combustion cell for quiescent runs. Figure 6.7 plots S_t/S_u against the parameter:

$$\eta = (u/S_u) (\Lambda/a)^{-1/2} \dots\dots\dots 6.3$$

and the data are overlaid with the line:

$$S_t/S_u = 1 + 0.15\eta \dots\dots\dots 6.4$$

To test the supposition that mixture strength has been isolated from this correlation, the 85% and 75% mixture results are compared to Equation 6.4 in Figure 6.8. The 85% data are seen to agree reasonably with the correlation, but the equation seems to slightly underestimate relative turbulent flame speeds for the 75% mixture.

In order to improve the correlation for leaner mixtures it is possible that the integral scale should be normalized with laminar flame thickness, but the validity of this approach should be tested by using more than one fuel type or introducing diluents to vary the flame thickness.

6.2.2 COMPARISON TO PREVIOUS WORK

A linear correlation between the flame speed ratio, S_t/S_u , and intensity has been observed in engine experiments as well as closed bomb and burner measurements. Lancaster [22] performed detailed hotwire turbulence measurements in a motored CFR engine for various operating conditions and

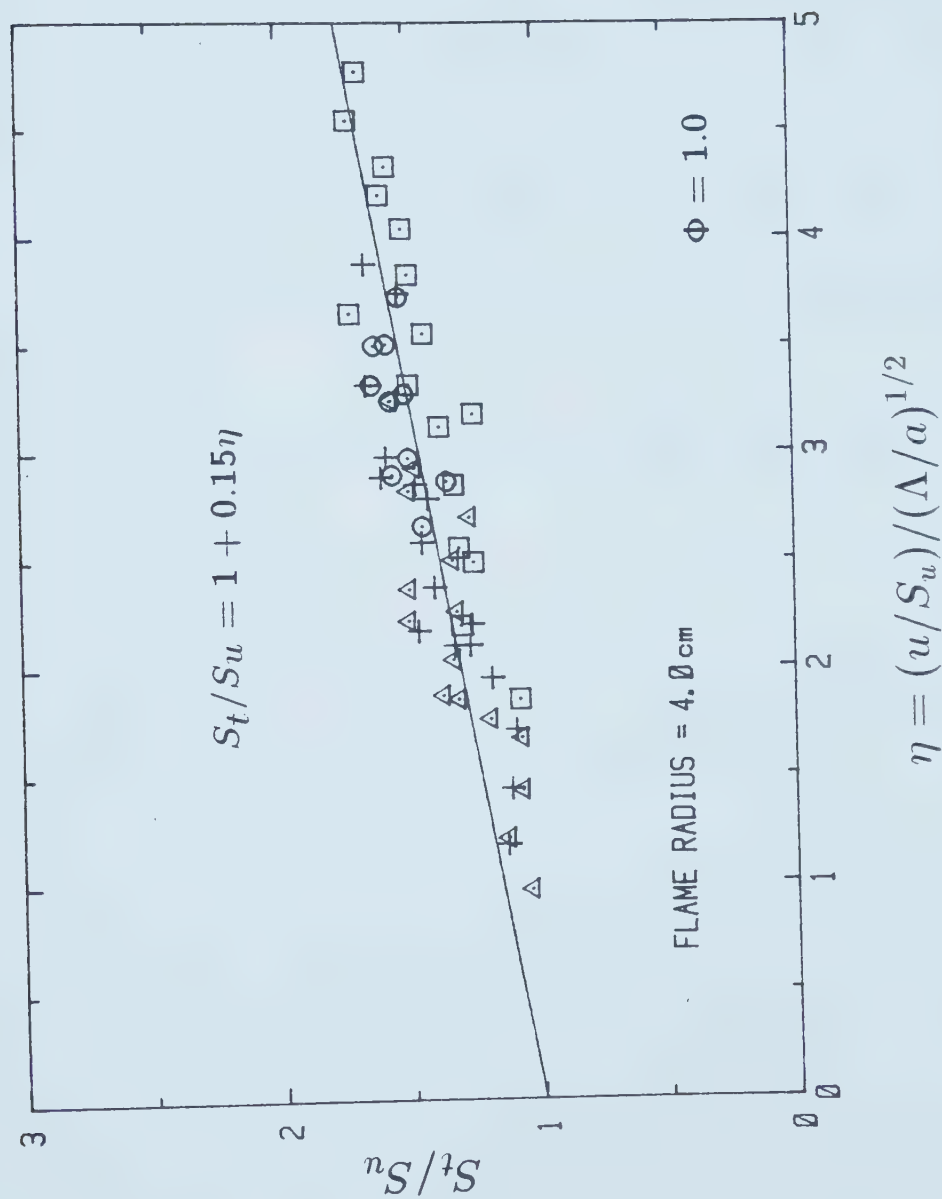


FIGURE 6.7 Correlation of Burning Speed Ratio to Instantaneous Intensity and Scale

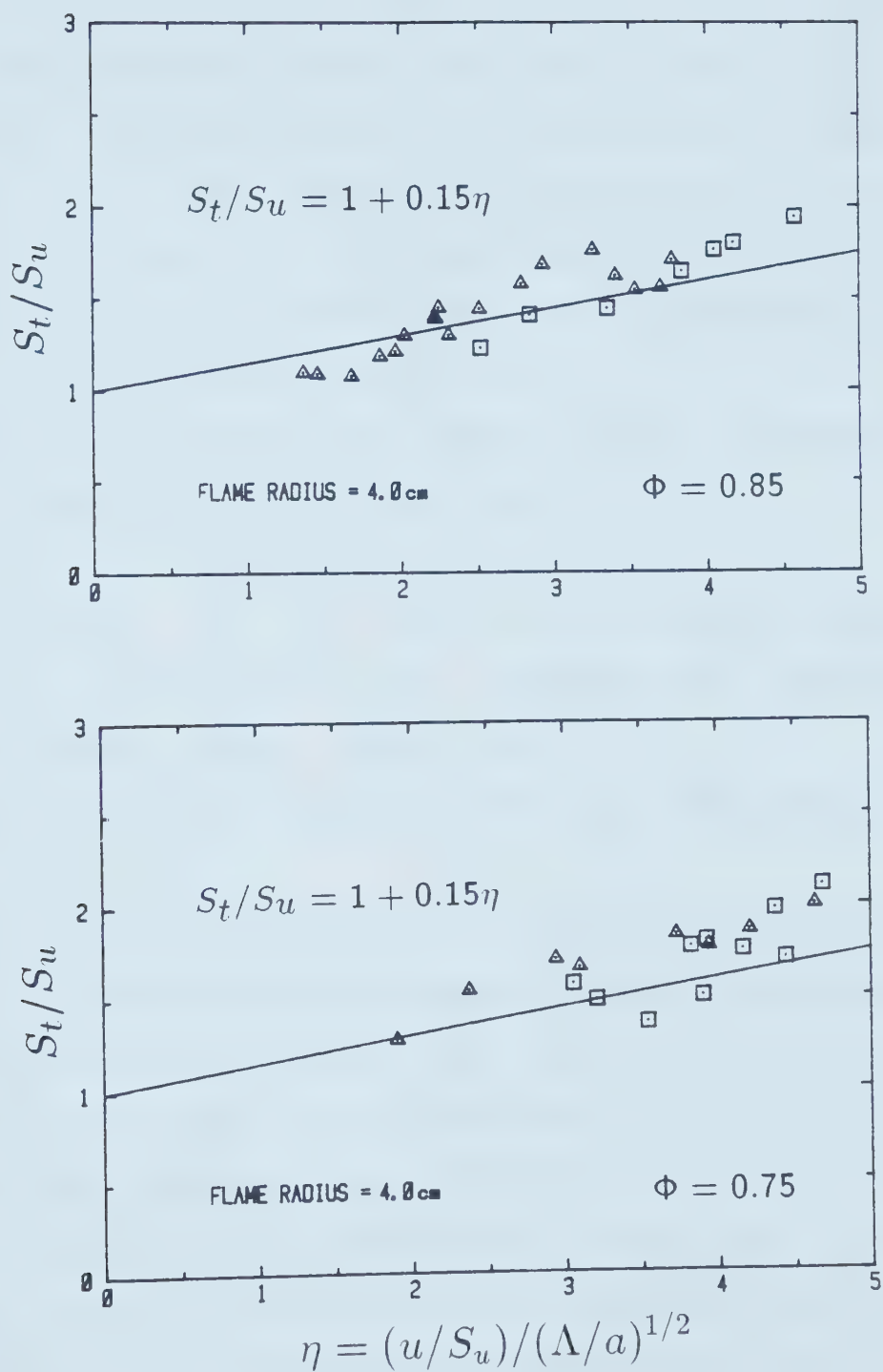


FIGURE 6.8

Comparing the Correlation to Lean Mixture Data

valve configurations. Intensities ranged from 1 to 5 m/s. Under identical running conditions with propane/air mixtures Lancaster et al [21] measured the flame speeds (calculated from the pressure history) associated with the motored turbulence levels. The results were seen to collapse to :

$$S_t/S_u = 1.3 + 0.91 u \quad \dots\dots\dots 6.5$$

Expressed in a like form, the results of the stoichiometric data of Figure 6.5 ($S_u \approx 39$ cm/s) reduce to:

$$S_t/S_u = 1.0 + b u \quad \dots\dots\dots 6.6$$

where b is 2.7, 1.7, 1.5, and 1.1 for integral scales of 1.8, 3.0, 5.5, and 10.6 mm respectively. Lancaster's integral scales ranged from about 3 to 12 mm, but no dependence of burning speed on scale were observed in that study.

The larger scale results of this study agree fairly well with that of Lancaster's measurements, despite the disparity in experimental techniques and the comparatively low intensity range used in the present study.

Groff and Matekunas [23] extended Lancaster's work to more conventional engine geometries, paying closer attention to the effect of combustion on turbulence evolution. A semi-empirical correlation was generated which corrected the motored turbulence levels for compression enhancement. Their result was:

$$S_t/S_u = 2.0 + 1.21(u/S_u)C_1C_2 \quad \dots\dots\dots 6.7$$

where C_1 was a theoretical correction of motored intensity for compression enhancement by combustion, and C_2 was an

empirical correlation to account for an observed spark timing effect. Generally

$$1.0 \leq C_1 \leq 1.5 \quad \text{and} \quad 1.0 \leq C_2 \leq 1.2$$

Intensities ranged from 1 to 9 m/s, but scales were not reported by these authors. It may be that a different range of integral scales than used in the present study could explain the slightly higher flame speeds predicted by Equation 6.7 compared to present results.

Ohigashi et al [20] performed photographic measurements with propane/air mixtures in a disk-shaped, centrally ignited bomb, where a perforated plate was used to generate turbulence in a manner similar to the present study. The results were presented in the form of flame propagation rates as a function of turbulence intensity. Their data reduce to the line:

$$S_f/S_{f0} = 1 + 1.9 u/S_{f0} \quad \dots\dots\dots 6.8$$

where S_{f0} is the quiescent flame propagation rate, and S_f is the turbulent flame propagation rate. In the present turbulent combustion cell, the quiescent flame propagation rate was 256 cm/s for a stoichiometric mixture at the 4 cm flame radius, and for $u = 15$ cm/s, a propagation rate of 336 cm/s was observed (see Figures 5.3 and 5.8). Thus the flame propagation rate ratio, $S_f/S_{f0} = 1.31$ seen here was higher than the 1.1 predicted by Equation 6.8, possibly due to the difference in flame shapes between the two studies (the flat disk chamber of Ohigashi had a height/diameter ratio of 10%). Lancaster [21] also noted somewhat higher

flame propagation rate ratios than seen in the Ohigashi study.

The results of a number of non-engine flame speed measurements in various burners, ducts, and fan stirred bombs have been assembled by Abdel-Gayed and Bradley [17], and combined with the results of their own investigation with hydrogen/air mixtures in a fan stirred bomb. Results were compiled into a family of curves of S_t/S_u against S_t/u for ranges of turbulent Reynold's numbers, $Re_\Lambda = \Lambda u/\nu$, from 25 to 3000.

Figure 6.9 compares the 'best fit' curves from [17] for two different ranges of Re_Λ with the engine correlation of [23] and the results of stoichiometric runs in the present study. Turbulent Reynolds numbers in the present study ranged from about 50 to 250.

Both the present results and the engine data of [23] show a much weaker dependence of flame speed on intensity than the curves of [17]. That the present results appear to agree more closely with the engine data of [21] and [23] is attributable to two principle differences between these sources and [17]:

- 1) Abdel-Gayed and Bradley's [17] measurement technique monitors the outermost edge of the flame and does not account for flame thickness. Increased intensity likely has greater effect on transport at the leading edge of the flame than on the actual progress of the average flame envelope, as is detected by the pressure based methods used here and

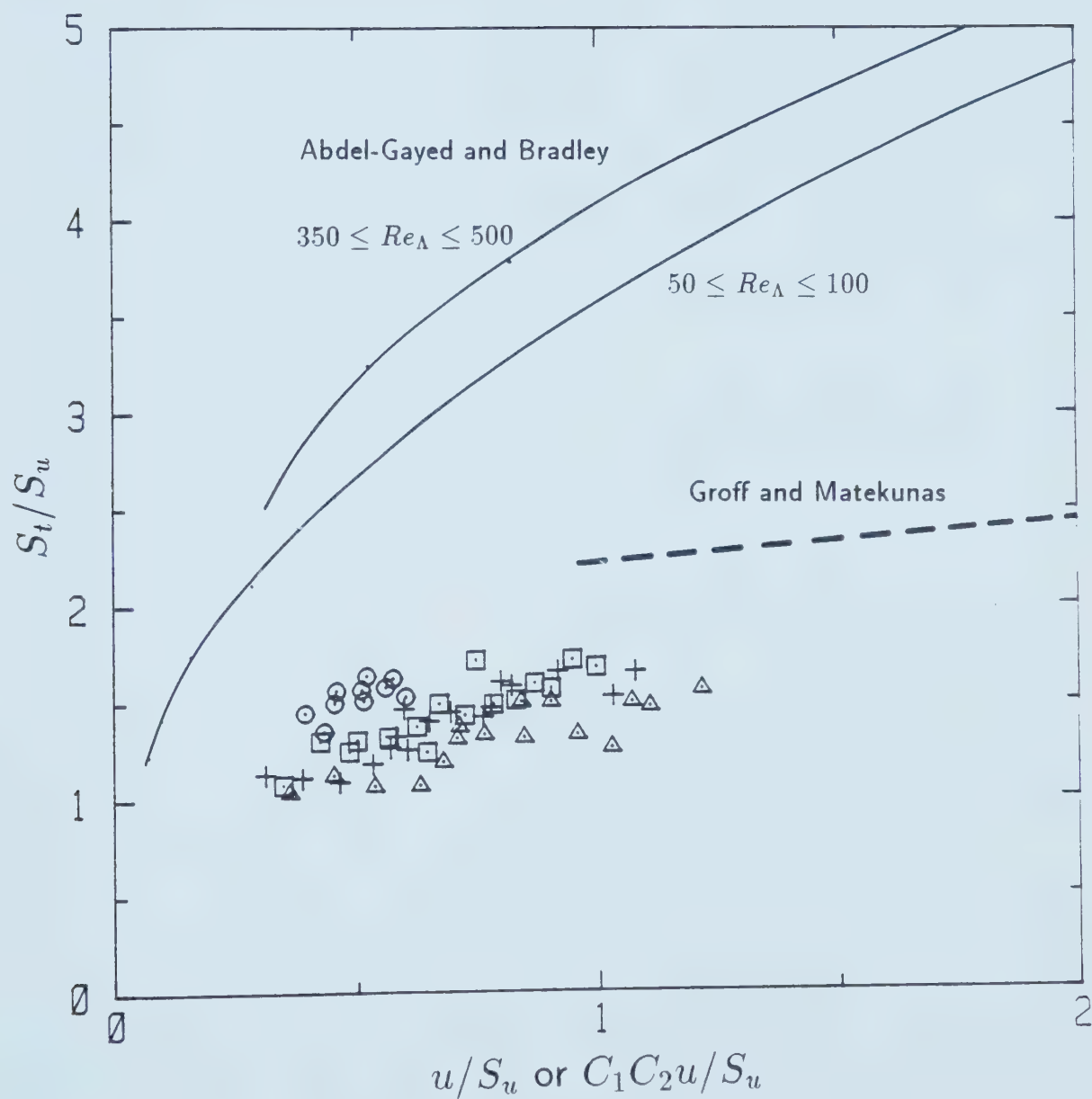


FIGURE 6.9

Comparing Data From The Present Study To
Other Sources

in [21] and [23].

2) All of the measurements reported in [17] were for stationary turbulence conditions (constant production); in the present study, and in [21,23], the turbulence was decaying (no production). Coherent structures of turbulence producing shear layers in stationary turbulence could be expected to effect flame speed through distortion, yet spatially fixed shear zones would not be manifested in local intensity readings.

The positive correlation of flame speed with Re_Λ reported by Abdel-Gayed and Bradley [17] contradicts the observation in the present study that flame speed varies with $\Lambda^{-1/2}$. In a more sensitive study of the effects of integral scale, Ballal and Lefebvre [15] measured flame speeds in a propane/air burner and reported that S_t/S_u increased with integral scale under conditions of 'low' turbulence, and decreased with scale in 'high' turbulence. The two regimes were separated approximately by $u/S_u = 2$. For an intensity of $u/S_u = 5$ and a scale range of $0.5 \leq \Lambda \leq 2.5$ mm, they found S_t/S_u proportional to $\Lambda^{-0.34}$. This could be a reasonable agreement with the present result, except that the present data would actually fall into the 'low' turbulence regime.

The inconsistency in observed effects of integral scale on burning speed for the different experimental techniques is an indication again that an effect of turbulence production may not be accounted for, that the integral scale

alone is not appropriate to represent turbulence scale effects, or that the evolution of turbulence during combustion has not be properly accounted for in some of the experiments. The integral scale is representative of the entire turbulence spectrum on average, and can not differentiate between the possibly separate effects of dissipation scales and large eddy scales.

Other observers already discussed [20,21] saw no effect of scale in their experiments. Several other sources where no scale effects were seen are also quoted in [21].

In general, the dependence of relative burning speed on intensity compares reasonably with other empirical sources, but the much smaller effect of scale remains inconsistent and somewhat contradictory among the same sources.

7. CONCLUSIONS

7.1 TURBULENCE

The temporal decay of turbulence intensity in the wake of the 60% solid perforated plates drawn across the interior of the combustion cell was shown to be similar to analogous spatial decay behind like plates fixed in a wind tunnel. The magnitude of intensity in the cell was about 30% lower than predicted by the direct analogy between plate speed and wind tunnel mean velocity, but decay rates were virtually identical. The measured intensity decay in the wind tunnel was also similar to results in the literature for perforated plates and grids of various geometries.

The decay of intensity fits a power function in the region beyond 10 plate hole diameters down stream of the plate. Intensity normalized with wind tunnel velocity (or plate speed), and distance (or plate speed times time) with plate hole diameter gave decay functions which were similar for the four different plates used.

Integral scales measured in the wind tunnel were assumed to apply in the combustion cell since turbulence generation and energy decay were identical.

Integral scale and intensity in the cell at the time of the spark could be independently controlled with control of the plate speed, plate hole diameter, and the time following the passage of the plate prior to ignition. However, this did introduce the decay rate at ignition as a third

variable. For a given intensity, a smaller integral scale is associated with faster decay rate.

7.2 FLAME MEASUREMENTS

All experiments were carried out with propane/air mixtures initially at room temperature and one standard atmosphere.

High speed photography and the ionization detection probe confirmed the accuracy of flame size predicted from the pressure history. This formulation was based on mass fraction burned as the fractional pressure rise, and a simple ideal gas model of burned and unburned gases separated by a thin spherical flame. The same simple formulation could be applied to mildly turbulent flames where the overall flame shape was still essentially spherical.

Flame speed could be derived from the predicted flame size history by abstracting from it the expansion component calculated assuming adiabatic ideal gas behavior. This technique required smoothing of the pressure trace to be effective. For the fully developed laminar flame, derived laminar flame speeds were about 10% greater than a prediction from an established flame speed correlation calculated at the measured pressure and a temperature appropriate to adiabatic compression of the unburned mixture.

The technique for monitoring flame growth with an

optically filtered photomultiplier proved less effective than pressure based measures due to a high repeatability uncertainty ($\pm 30\%$ in output signal for a fixed flame size between identically prepared laminar runs) which was attributed to the $\pm 2\%$ mixture uncertainty. However, a simple calibration of the photomultiplier to flame area or mass burning rate of a laminar explosion was demonstrated, so that the same parameters might be measured directly in turbulent runs.

7.3 TURBULENCE AND FLAME GROWTH

The peak pressures reached by turbulent explosions were increased significantly over that of the laminar explosion by the mildest levels of turbulence used. Increasing the turbulence further only slightly increased the peak pressure, as the theoretical adiabatic maximum had been practically reached. It is most likely that the benefit of turbulence here is in the rapid burning in the final stages of combustion, reducing wall quenching effects.

Comparison of the relative reductions in time to reach the peak pressure and the time to reach an arbitrary fixed flame size showed that the turbulence played a significant role in enhancing burning rate in the latter stages of combustion near the wall. This would infer that the longer lived, large scale turbulence might be of greatest benefit in reducing combustion time. However, it was observed that smaller integral scales better enhanced burning speed for a

given intensity so a trade off between early and late combustion rate improvements is expected. In fact, it was seen that an intermediate integral scale gave the shortest burning times in stoichiometric mixtures over the range of intensities examined.

Turbulent flame speeds measured at a fixed flame size in the fully developed regime were fitted with the correlation of Equation 6.2, where turbulence parameters were estimated at one flame size assuming undistorted turbulence decay. This correlation appeared reasonably independent of mixture strength. The linear dependence of turbulent to laminar flame speed ratio with intensity is in agreement with other empirical sources. The inverse dependence of the flame speed ratio with the square root of the integral scale can not be confirmed, since integral scale dependence is a matter of much inconsistency and contradiction in the literature. This may be due in part to the difficulty inherent in measuring turbulence scales.

It is speculated that the integral scale may not be an appropriate parameter to correlate, since similar integral scales may be generated from very different turbulent spectra and would not be able to account for possibly independent influences of large scales and dissipation scales.

7.4 RECOMMENDATIONS FOR FUTURE RESEARCH

The turbulent combustion cell has proven a reliable

medium for generation of turbulent combustion data. Some improvements over the present work are suggested to improve data quality, especially if the same or similar apparatus will be used.

Improved mixture control must be sought to reduce the repeatability uncertainty between runs. It is suggested that careful gas analysis should be performed to insure a high certainty in mixture strength, since it may become of interest to isolate the possible effects of turbulence on explosion variability.

Future work to generate turbulent burning speed correlations suitable for engine applications should attempt to encompass a wider range of intensities.

Improved pressure sensing equipment with better signal to noise ratio would reduce uncertainty and variability in pressure based diagnostics. In retrospect, it would seem that the piezo-electric charge type pressure transducer is not the appropriate choice for such one-shot measurements with relatively slow burning charges. In fact, during the writing of this work, experiments with a classic strain gage transducer have shown better results.

Once mixture uncertainty has been reduced, the photomultiplier based technique should be re-examined, since it did show good promise as an early flame growth monitor.

In more general terms, further work must be done to shed light on some aspects of the turbulence-flame interaction which could not be resolved in the present work.

More empirical and theoretical data are required to predict the evolution and distortion of turbulence during flame growth in a closed vessel. The turbulent combustion cell apparatus could easily be adapted for such a study, since the optical windows afford the opportunity for laser anemometry during combustion.

Correlations of flame speed to other turbulent scales should be studied to possibly determine any separate effects of large eddy scales and small dissipation scales. Also the possibility of using the laminar flame thickness in the flame speed correlation should be experimentally and theoretically tested.

The comparability of flame speed in stationary turbulence with that in decaying zero production turbulence should be examined.

Improved understanding of the turbulent flame and the factors which influence flame propagation rate must ultimately result in improved engine and combustor design. This will in turn provide more efficient use of chemical energy resources, and help reduce the harmful by-products of combustion which are becoming a threat to the health of Earth's atmosphere.

REFERENCES

1. G.M. Rassweiler and L. Withrow, "High Speed Motion Pictures of Engine Flames Correlated with Pressure Cards" SAE J., May 1938
2. C.L. Bouchard, C.F. Taylor, and E.S. Taylor, "Variables Affecting Flame Speed", SAE J., Vol 41., no. 5, Nov 1937
3. M.D. Checkel, Turbulent Enhanced Combustion of Lean Mixtures, PhD Thesis, Cambridge University, 1981
4. M.D. Checkel and A. Thomas, "Turbulent Explosions in Closed Vessels", Paper C57/1983, Combustion in Engineering, I.Mech.E., Oxford 1983
5. C.J. Gibbs and H.C. Calcote, "The Effect of Molecular Structure on Burning Velocity", Journal of Chemical Engineering Data Vol 4, pp 226, 1959
6. G.E. Andrews and D. Bradley, "Determination of Burning Velocities: A Critical Review", Combustion and Flame, Vol 18, pp 133, 1972
7. B. Lewis and G. von Elbe, Combustion, Flames and Explosions of Gases, Academic Press, 3rd Ed.1987
8. L. Flamm and H. Mache, Wien Ber. 126, 1917
9. M. Metghalchi and J.C. Keck, "Laminar Burning Velocity of Propane-Air Mixtures at High Temperatures and Pressures" Combustion and Flame, Vol 38, pp 143, 1980
10. M. Metghalchi and J.C. Keck, "Burning Velocities of Mixtures of Air with Methanol, Isooctane, and Indolene At High Temperatures and Pressures", Combustion and Flame, Vol 48, pp 191, 1982
11. G.E. Andrews, D. Bradley, and S.B. Lwakabamba, "Turbulence and Turbulent Flame Propagation: A Critical Appraisal", Combustion and Flame, Vol 24, pp 285, 1975
12. R.G. Abdel-Gayed and D. Bradley, "A Two Eddy Theory of Premixed Turbulent Flame Propagation", Phil. Trans. R. Soc. London, A301, pp 1, 1981
13. J. Abraham, F.A. Williams, F.V. Bracco, "A Discussion of Flame Structure in Premixed Charges", SAE paper 850345, 1985
14. M.D. Fox and F.J. Weinberg, "An Experimental Study of Burner Stabilized Turbulent Flames in Premixed Reactants", Proc. R. Soc. London, A268, pp222, 1961

15. D.R. Ballal and A.H. Lefebvre, "The Structure and Propagation of Turbulent Flames", Proc. R. Soc. London, A344, pp 217, 1975
16. S.B. Lwakabamba, "Turbulent Flame Propagation in Closed Vessels", Ph.D Thesis, University of Leeds, 1975
17. R.G. Abdel-Gayed, D. Bradley, "Dependence of Turbulent Burning Velocity on Turbulent Reynolds Number and Ratio of Laminar Burning Velocity to RMS Turbulent Velocity" 16th Symposium (International) on Combustion, The Combustion Institute, pp 1725, 1976
18. R.G. Abdel-Gayed, D. Bradley, and M. McMahon, "Turbulent Flame Propagation in Premixed Gases: Theory and Experiment", 17th Symposium (International) on Combustion, The Combustion Institute, pp 245, 1978
19. D.E. Fuller, "Mixture Motion in an Engine Cylinder", Ph.D Thesis, University of Cambridge, 1975
20. S. Ohigashi, Y. Hamamoto, and A. Kizima, "Effects of Turbulence on Flame Propagation in Closed Vessels", Bull. of the JSME, Vol 14, No 74, pp 849, 1971
21. D.R. Lancaster, R.B. Krieger, S.C. Sorenson, W.L. Hull, "Effect of Turbulence on Spark Ignition Engine Combustion", SAE paper 760160, SAE Trans. Vol 85, pp 689, 1976
22. D.R. Lancaster, "Effects of Engine Variables on Turbulence in A Spark ignition Engine", SAE paper 760159, SAE Trans., Vol 85, pp 671, 1976
23. E.G. Groff and F.A. Matekunas, "The Nature of Turbulent Flame Propagation in a Homogeneous Charge Spark Ignited Engine", SAE paper 800133, pp 740, 1980
24. V.W. Wong and D.P. Hoult, "Rapid Distortion Theory Applied to Turbulent Combustion", SAE paper 790357, 1979
25. A.A. Townsend, Structure of Turbulent Shear Flow, Cambridge University Press, 1956
26. M.D. Checkel, "Measurements of Turbulence Behind 60% Solid Perforated Plates", ASME Trans., J. of Fluids Engineering, March 1986
27. J. Hinze, Turbulence, 2nd Ed., McGraw-Hill, 1975
28. G.I. Taylor, "Statistical Theory of Turbulence", Proc. R. Soc. London, Vol A151, pp 421, 1935

29. T. von Karman and L. Howarth, "On The Statistical Theory of Isotropic Turbulence", Proc. R. Soc. London, Vol A164, pp 192, 1938
30. F.N. Frenkial, "The Decay of Isotropic Turbulence" Trans. of the ASME, Vol 70, pp 311, 1948
31. W.D. Baines and E.G. Peterson, "An Investigation of Flow Through Screens", Trans. of the ASME, Vol 73, pp 467, 1951
32. M.S. Uberoi and S. Wallace, "Effects of Grid Geometry on Turbulence Decay", The Physics of Fluids, Vol 10, No 6, pp 1216, 1967
33. M. Tsuge, H. Kido, and H. Yanagihara, "Decay of Turbulence in a Closed Vessel", Bul. of the JSME, Vol 16, No 92, pp 244, 1973
34. P. Fremuth, "Frequency Response and Electronic Testing For Constant Temperature Hot Wire Anemometers", J. Phys Eng. Sci. Instruments, Vol 10, pp 705, 1977
35. Acrivllelis, "Hotwire Measurements in Flows of Low and High Turbulence Intensities", DISA Information No 22, Sept. 1977.
36. Acrivlellis, "An Improved Method for Determining The Flowfield of Multidimensional Flows at any Turbulence Intensity", DISA Information No 23, Sept. 1978
37. W.C. Reynolds, "STANJAN Chemical Equilibrium Solver V 3.81", Mechanical Engineering, Stanford University, 1987
38. G.J. van Wylen and R.E. Sonntag, Fundamentals of Classical Thermodynamics, John Wiley and Sons, 1978
39. B. Karlovitz, D.W. Denniston Jr, D.H. Knapschaefer, and F.E. Wells, "Studies on Turbulent Flames", Fourth Symposium (International) on Combustion, pp 613, 1953
40. I.R. Hurle, R.B. Price, T.M Sugen, and A. Thomas, "Sound Emission From Open Turbulent Premixed Flames" Proc. R. Soc. London, Vol A303, pp 409, 1968
41. R. John and M. Summerfield, "Effect of Turbulence on Radiation Intensity From Propane Air Flames", Jet Propulsion, Vol 27, pp 169, 1957
42. S. Chang and K. Rhee, "Adiabatic Flame Temperature Estimate of Lean Fuel-Air Mixtures", Combustion Science and Technology, Vol 35, pp 203, 1983

B45963